A measurement of the permanent electric dipole moment of ^{129}Xe

by

Natasha Sachdeva

A dissertation submitted in partial fulfillment
of the requirements for the degree of
Doctor of Philosophy
(Physics)
in The University of Michigan
2019

Doctoral Committee:

Professor Timothy Chupp, Chair
Professor Wolfgang Lorenzon
Professor Sara Pozzi
Assistant Professor Joshua Spitz
Professor James Wells

TABLE OF CONTENTS

LIST OF FIGURES

Figure

LIST OF TABLES

Table

ABSTRACT

A measurement of the permanent electric dipole moment of ^{129}Xe

by

Natasha Sachdeva

Chair: Timothy Chupp

Searches for permanent electric dipole moments (EDMs) are a powerful way to investigate Beyond-the-Standard-Model CP-violation. This work describes the development of a new technique to measure the EDM of ^{129}Xe with a ^{3}He comagnetometer and reports the results of our first measurement. In the HeXeEDM experiment, ^{3}He and ^{129}Xe are polarized using spin-exchange optical pumping, transferred to a measurement cell, and transported into a magnetically shielded room. The free precession of both species is detected with SQUID magnetometers in the presence of an applied 2.7–3.3 kV/cm electric field and a 2.6 μT magnetic field. Linear comagnetometer drifts are compensated by combinations of four segments with alternating high-voltage. The results of a one week run and extensive study of systematic effects is $d_A(^{129}\mathrm{Xe}) = 0.25 \pm 2.32(\mathrm{stat.}) \pm 0.73(\mathrm{syst.}) \times 10^{-27}\ e\,\mathrm{cm}$. This result corresponds to an upper limit of $|d_A(^{129}\mathrm{Xe})| < 4.8 \times 10^{-27}\ e\,\mathrm{cm}$ (95% c.l.), which is $\approx 40\%$ more sensitive than the previous limit.

CHAPTER I

Motivation

1.1 Introduction

The fundamental symmetries of charge conjugation (C), parity (P), and time-reversal (T) have puzzled physicists for decades. From the seminal measurements of parity-violation in the late 1950s followed by the discovery of CP-violation in the mid-1960s, our understanding of symmetries and their role in the fundamental interactions of particles has evolved. The culmination of that knowledge and all known forces and elementary particles into a self-consistent theory is known as the Standard Model of particle physics.

Despite the great success of the Standard Model, many physical observations are yet unexplained. One of these is the predominance of matter over antimatter in the universe. To understand the baryon asymmetry, we investigate the symmetries between particles and antiparticles, C and CP symmetry. The Standard Model accommodates small amounts of CP-violation, but it is not enough. In many extensions of the Standard Model, sources of CP-violation arise naturally.

Electric dipole moments (EDMs) of particles, atoms, and molecules are manifestations of CP-violation and therefore may provide insight into new physics. EDMs in different systems are sensitive to different sources of beyond-the-Standard-Model CP-violation; therefore, measurements in many systems are necessary to provide a complete picture. Neutron EDM measurements have been ongoing for decades. Atomic and molecular EDM measure-

ments have been used to set stringent limits on the electron EDM. Diamagnetic atoms are uniquely sensitive to possible new CP-violating interactions between nucleons. Currently, the EDM limit of ^{199}Hg, a diamagnetic atom, is the most sensitive to date of any system. However, theoretical uncertainty in atomic and nuclear structure calculations have made it difficult to take advantage of the experiment's precision to set limits on new physics.

^{129}Xe, another diamagnetic atom, had been investigated in the past with the most recent published limit in 2001. In 2013, the opportunity arose for a new ^{129}Xe investigation, taking advantage of a magnetically-shielded environment developed for a neutron EDM experiment in Garching, Germany. The experiment, HeXeEDM, uses a ^{3}He–^{129}Xe comagnetometer and a new measurement technique, detection with SQUID magnetometers. This work provides an overview of the experiment's progress toward our first EDM measurement, which was a low-statistics campaign with one week of data collection. In later chapters, the analysis including an extensive study of systematic effects and final results are presented.

1.2 Background

1.2.1 Matter-Antimatter Asymmetry

The baryonic matter in the universe is dominated by matter rather than antimatter. The asymmetry between baryons and antibaryons is characterized by the baryon-to-photon ratio determined through big-bang nucleosynthesis (BBN) observations of light element (^{3}He, ^{4}He, D, ^{6}Li, and ^{7}Li) abundances and independently from the Cosmic Microwave Background (CMB). The baryon-to-photon ratio is [1]

$$\eta = \frac{n_B - n_{\bar{B}}}{n_\gamma} = 6.1^{+0.3}_{-0.2} \times 10^{-10}, \tag{1.1}$$

where n_B is the number density of baryons, $n_{\bar{B}}$ is the number density of antibaryons, and n_γ is the number density of photons. It is notably not zero, which one might expect in a

homogenous baryon-symmetric universe. In fact, in the case that the universe expansion is faster than annihilation reactions in local thermal equilibrium, there would be leftover baryons and antibaryons, known as "freeze out". The freeze-out abundance is [2, 3]

$$\frac{n_B}{n_\gamma} = \frac{n_{\bar{B}}}{n_\gamma} \approx 10^{-20} \tag{1.2}$$

which is too small to explain current observations.

Because of inflation, we do not expect baryon asymmetry to be an initial condition of the universe because baryon-symmetric interactions would dilute any asymmetry during inflation. Therefore, it is necessary for the baryon asymmetry to be generated dynamically, known as baryogenesis.

1.2.2 Sakharov Conditions

Sakharov's conditions for baryogenesis [4] are the ingredients needed to create baryon asymmetry dynamically:

1. B violation
2. Loss of thermal equilibrium
3. C and CP violation

B violation It is clear that to generate baryon asymmetry, baryon number (B) must not be conserved.

Loss of thermal equilibrium In thermal equilibrium, any baryon-asymmetric process has an inverse process with equal rate resulting in no net asymmetry. Therefore, interactions must take place outside of thermal equilibrium.

C and CP violation Charge conjugation (C) is the symmetry between particles and antiparticles. When C is conserved, the rate for any process that generates excess baryons has a C-conjugate process that generates antibaryons, and no net asymmetry is observed.

Similarly, if a process violates C but is CP (charge-parity) symmetric, no net asymmetry is observed. For example, if a process generates excess left-handed baryons, even if the C-conjugate process does not occur, under CP-symmetry the conjugate process producing right-handed antibaryons restores B. Therefore, both C and CP violation are necessary.

1.2.3 CP-violation in the Standard Model

CP-violation in the Standard Model (SM) has been observed in kaon, B meson, and strange B meson decays. It is parametrized as the complex phase in the Cabbibo-Kobayashi-Maskawa (CKM) quark-mixing matrix. There is also an unobserved source of CP violation in the standard model, the θ-term in the QCD Lagrangian [5]

$$\mathcal{L}_{\bar{\theta}} = -\frac{\alpha_S}{16\pi^2}\bar{\theta}\mathrm{Tr}\left(G^{\mu\nu}\tilde{G}_{\mu\nu}\right), \tag{1.3}$$

where $G_{\mu\nu}$ is the gluon field strength tensor and $\tilde{G}_{\mu\nu} = \epsilon_{\mu\nu\alpha\beta}G^{\alpha\beta}/2$ is its dual. $\bar{\theta}$ is experimentally constrained by measurements of electric dipole moments to be $< 10^{-10}$, which is known as the "strong CP" problem. The strong CP problem has motivated solutions such as the spontaneously broken Peccei-Quinn symmetry, which generates axions.

However, it is generally agreed upon [3] that SM CP violation is too small for baryogenesis, motivating the search for beyond-the-standard model (BSM) sources of CP violation.

1.3 Electric Dipole Moments (EDMs)

An electric dipole moment is the electric analogue to the magnetic dipole moment. For a spin-$1/2$ particle with magnetic dipole moment μ, the P-even, T-even interaction with the

electromagnetic field strength tensor $F_{\mu\nu} = \partial\mu A_\nu - \partial_\nu A_\mu$ is [6]

$$\mathcal{L}_{\text{MDM}} = -\mu\frac{1}{2}\bar{\Psi}\sigma^{\mu\nu}F_{\mu\nu}\Psi. \tag{1.4}$$

For the transformation $\mathbf{B} \to \mathbf{E}$, we make the transformation $F_{\mu\nu} \to -\tilde{F}_{\mu\nu}$ where $\tilde{F}_{\mu\nu} = \epsilon_{\mu\nu\alpha\beta}F^{\alpha\beta}/2$ is its dual. Using the identity $\epsilon_{\mu\nu\alpha\beta}\sigma^{\alpha\beta}/2 = -i\gamma^5\sigma_{\mu\nu}$,

$$\mathcal{L}_{\text{EDM}} = -d\frac{i}{2}\bar{\Psi}\sigma^{\mu\nu}\gamma^5 F_{\mu\nu}\Psi, \tag{1.5}$$

which is P-odd due to the appearance of the chirality matrix γ^5 and, because the time-reversal operator T is antiunitary, the additional i in $\mathcal{L}_{\text{EDM}}$ implies it is T-odd. This is clear in the nonrelativistic limit where $\mathbf{S}$ is the particle spin [6]

$$\mathcal{H}^{\text{nr}}_{\text{EDM}} = -d\frac{\mathbf{S}}{S}\cdot\mathbf{E}. \tag{1.6}$$

Under parity $\mathbf{S} \to \mathbf{S}$ and $\mathbf{E} \to -\mathbf{E}$. Under time-reversal, $\mathbf{S} \to -\mathbf{S}$ and $\mathbf{E} \to \mathbf{E}$. Assuming CPT conservation, the T-violation of EDMs means non-zero EDMs are also CP-violating.

The history of EDM searches can be traced back nearly 70 years ago to 1950 when Purcell and Ramsey [7] suggested the possibility of a parity-violating electric dipole moment. Shortly thereafter, the first measurement of the neutron EDM was completed [8]. The negative result was not published [9] until after the discovery of parity violation in the weak sector [10, 11, 12, 13]. Later, after CP-violation in K^0 decay [14], there was renewed interest in EDMs as probes of CP-violation.

1.3.1 Atomic and Molecular EDMs

EDMs may also be investigated in atoms and molecules with nondegenerate ground states. For a system with total angular momentum $\mathbf{F}$, the EDM $\mathbf{d}$ relative to the center of

mass ($\mathbf{r} = 0$) is [5]

$$\mathbf{d} = \int \mathbf{r}\rho_Q d^3r = d\frac{\mathbf{F}}{F}, \tag{1.7}$$

where ρ_Q is the electric-charge distribution. In atoms, there is a shielding effect described by Schiff's theorem [15] such that in a neutral system composed of nonrelativistic point-like particles in equilibrium under the effect of electrostatic forces, the net electric field at each charged particle is zero. The effect is a result of the internal rearrangement of charged particles to generate an internal electric field $\mathbf{E}_{\text{int}}$ that cancels the externally applied field $\mathbf{E}_{\text{ext}}$; therefore, an EDM cannot be observed.

However, the shielding is incomplete in the case of a finite nucleus and from relativistic effects in (paramagnetic) systems with unpaired electrons. Paramagnetic atoms additionally have an enhancement of the electron EDM d_e approximately proportional to Z^3 [16, 17]. BSM CP-violating interactions between the electrons and the nucleus may also generate an atomic EDM.

Diamagnetic atoms are sensitive to BSM CP-violating nucleon-nucleon interactions that couple through the Schiff moment $\mathbf{S}$, which is the r^2-weighted electric-dipole charge distribution [5]

$$\mathbf{S} = \frac{1}{10}\int r^2\mathbf{r}\rho_Q d^3r - \frac{1}{6Z}\int r^2 d^3r \int \mathbf{r}\rho_Q d^3r, \tag{1.8}$$

where the second term is subtracted because it is the contribution from the nuclear EDM, which cannot be observed in a neutral atom.

1.3.2 Global EDM Analysis

BSM sources of CP-violation manifest differently in different EDM systems. To interpret the results of EDM measurements across the experimental landscape to constrain BSM CP-violation in a model-independent way, a formalism based on an electroweak-scale effective field theory (EFT) has been developed and is applied in Refs. [18, 19, 20, 5]. In the EFT approach, experimental observables constrain the EFT operator coefficients while

BSM theory provides predictions for the same coefficients. We briefly summarize the approach below.

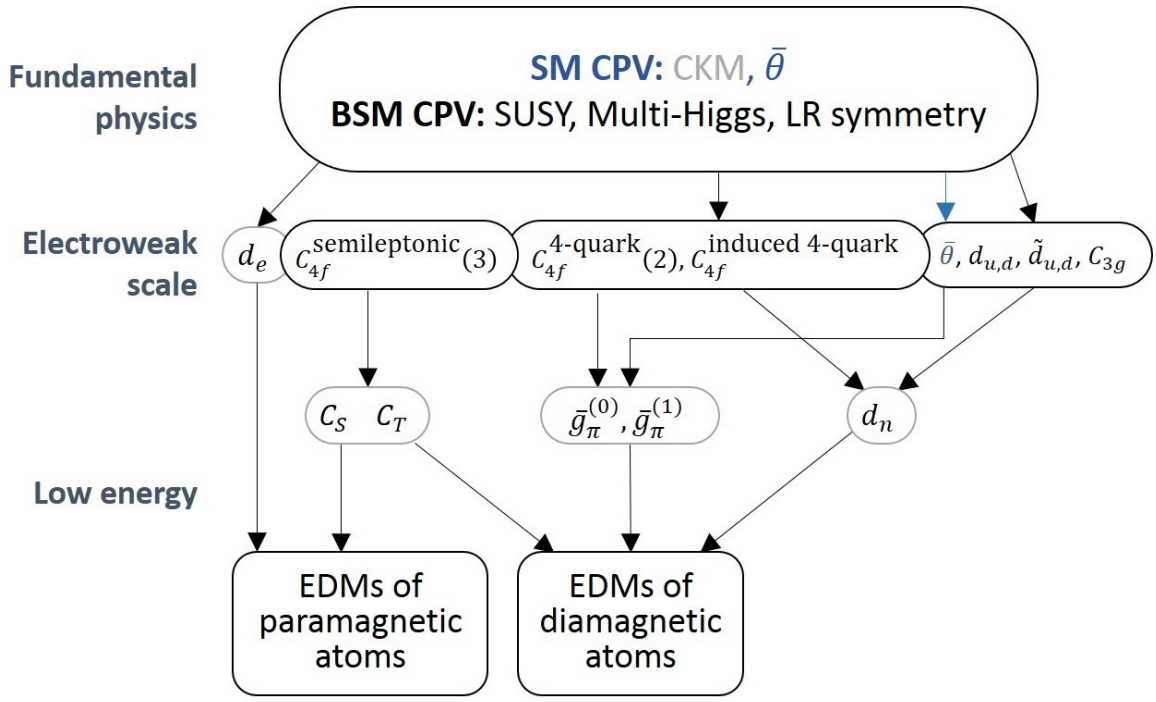

Figure 1.1: Illustration of how CP-violation, including Standard Model and beyond-the-Standard-Model physics, may manifest in experimentally observable EDMs. The electroweak scale parameters are derived from the EFT theory described in the text.

The EFT consists of a set of non-renormalizable dimension-6 operators based on SM fields that are $\propto v^2/\Lambda^2$ where $v = 246$ GeV is Higgs vacuum expectation value and Λ is the mass scale of new physics. The CP-violating Lagrangian incorporating SM and BSM contributions is

$$\mathcal{L}_{\text{CPV}} = \mathcal{L}_{\text{CKM}} + \mathcal{L}_{\bar{\theta}} + \mathcal{L}_{\text{BSM}} \tag{1.9}$$

where $\mathcal{L}_{\text{BSM}}$ contains new physics at dimension six or higher. Here, we only consider the EFT contribution at dimension six

$$\mathcal{L}_{\text{BSM}}^{\text{eff}} = \frac{1}{\Lambda^2} \sum_k \alpha_k^{(6)} \mathcal{O}_k^{(6)}, \tag{1.10}$$

where $\alpha_k^{(6)}$ are the Wilson coefficients for each operator $\mathcal{O}_k^{(6)}$. The operators include sources of CP-violation such as fermion EDMs and chromo-EDMs, four-fermion semi-leptonic and non-leptonic interactions, a three-gluon interaction, and a quark-Higgs interaction [18]. From these coefficients, a set of independent low-energy parameters are derived to describe CP-violation at the hadronic scale. These include CP-violating nucleon-nucleon interactions $\bar{g}_\pi^{(I)}$ for isospin $I = 0, 1, 2$; scalar and tensor electron-nucleon interactions $C_S^{(I)}$ and $C_T^{(I)}$, respectively; and the electron EDM d_e and short-range contribution to the neutron EDM $\bar{d}_n$. The EDM of a particular system can be written as [19]

$$d_i = \sum_j \alpha_{ij} C_j \tag{1.11}$$

where C_j are the low-energy parameters and the coefficients α_{ij} (sometimes written as $\frac{\partial d_i}{\partial C_j}$) are provided by atomic and nuclear theory calculations. Fig. 1.3.2 shows to which low-energy sources of CP-violation the observable EDMs in paramagnetic and diamagnetic systems are primarily sensitive. The inverse of Eq. 1.11 in terms of measured EDMs [21, 22, 23, 24] from Ref. [5] (see Table IV within for α_{ij} and references) is

$$\begin{bmatrix} \bar{d}_n^{\text{sr}} \\ \bar{g}_\pi^{(0)} \\ \bar{g}_\pi^{(1)} \\ C_T^{(0)} \end{bmatrix} = \begin{bmatrix} 5.2 & 4.7 \times 10^4 & 9.5 \times 10^3 & 21 \\ -2.8 \times 10^{14} & -3.1 \times 10^{18} & -6.3 \times 10^{17} & -1.4 \times 10^{15} \\ -7.0 \times 10^{13} & -7.7 \times 10^{17} & -1.6 \times 10^{17} & -4.8 \times 10^{14} \\ 1.9 \times 10^{16} & 1.4 \times 10^{19} & 3.6 \times 10^{19} & 8.4 \times 10^{16} \end{bmatrix} = \begin{bmatrix} d_n \\ d_{\text{Xe}} \\ d_{\text{Hg}} \\ d_{\text{Ra}} \end{bmatrix}. \tag{1.12}$$

Note that while d_{Xe} and d_{Hg} are similarly sensitive to low-energy CP-violating parameters, there is considerable uncertainty in $\frac{\partial d_{\text{Hg}}}{\partial d g_\pi^{(I)}}$, in particular an unknown sign of $\frac{\partial d_{\text{Hg}}}{\partial d g_\pi^{(1)}}$.

1.4 ^{129}Xe EDM searches

The first ^{129}Xe EDM measurement by Vold *et al.* monitored ^{129}Xe Larmor precession frequencies as a function of applied electric fields [25]. Development of a ^{129}Xe–^{3}He comagnetometer for an ^{129}Xe EDM search by Oteiza and Chupp [26, 27] led to a measurement of $d_A(^{129}\mathrm{Xe})$ by Rosenberry and Chupp [22] using a two-species Zeeman maser for continuous running over months and reported $d_A(^{129}\mathrm{Xe}) = 0.7 \pm 3.3 \times 10^{-27}\ e\,\mathrm{cm}$, the most sensitive ^{129}Xe measurement to date. Current ^{129}Xe efforts include an active maser technique that is currently being explored [28], and the use of liquid xenon has also been investigated [29]. An approach similar to the one described in this work using free precession and SQUID magnetometry is being pursued [30]. Additionally, ^{129}Xe is being considered as a comagnetometer in a neutron EDM experiment [31] and, in order to measure the neutron EDM with sensitivity $1 \times 10^{-27}\ e\,\mathrm{cm}$, the ^{129}Xe EDM sensitivity must be reduced to $\lesssim 3 \times 10^{-28}\ e\,\mathrm{cm}$.

CHAPTER II

The HeXeEDM Experiment: Methods

The layout of the HeXeEDM experiment is shown in Fig. 3.6. The basic principle of the experiment was as follows: ^{129}Xe and ^{3}He were polarized using spin-exchange optical pumping and then transferred to a measurement cell with electrodes. The measurement cell was placed in a magnetically shielded room near SQUID detectors in a holding magnetic field created by a set of Helmholtz coils. Spin precession of the ^{129}Xe and ^{3}He was achieved using either a nonadiabatic magnetic field rotation or using an oscillating magnetic field pulse resonant with both species. The SQUIDs detected the magnetization from the precessing ^{129}Xe and ^{3}He. Finally, we applied a high voltage to one electrode of the cell and held the other at ground potential. The ^{3}He signal was used as a comagnetometer to correct the ^{129}Xe signal for magnetic field fluctuations. $d_A(^{129}\mathrm{Xe})$ was determined from the comagnetometer corrected ^{129}Xe frequency.

In this chapter, we will review separately the main components of the experiment: comagnetometry (2.1), spin precession (2.2), spin-exchange optical pumping (2.3), use of magnetically shielded rooms (2.4), SQUID magnetometry (2.5), and measurement cells (2.6).

2.1 Precision requirements and comagnetometry

As mentioned previously, an electric dipole moment is analogous to the magnetic dipole moment

$$\boldsymbol{\mu} = \mu \frac{\mathbf{F}}{F} = \gamma \mathbf{F} \tag{2.1}$$

for an atom where γ is the gyromagnetic ratio and $\mathbf{F} = \mathbf{I} + \mathbf{J}$ is the total angular momentum. For both ^{129}Xe and ^{3}He the electronic total angular momentum $\mathbf{J} = 0$ and the nuclear spin $\mathbf{I} = 1/2$. We will continue to use $\mathbf{F}$ for generality. Similarly for the electric dipole moment

$$\mathbf{d} = d \frac{\mathbf{F}}{F}. \tag{2.2}$$

Under the influence of applied magnetic and electric fields, the Hamiltonian is

$$\mathcal{H} = -\boldsymbol{\mu} \cdot \mathbf{B} - \mathbf{d} \cdot \mathbf{E} \tag{2.3}$$

For $\mathbf{B} = +B_0 \hat{\mathbf{z}}$ and $\mathbf{E} = +E_0 \hat{\mathbf{z}}$,

$$U(+B_0, +E_0) = -\gamma \hbar m_F B_0 - d(m_F/F) E_0. \tag{2.4}$$

If the gyromagnetic ratio is positive, a positive m_F will be energetically preferred. Similarly, for a negative gyromagnetic ratio (like those of ^{129}Xe and ^{3}He), a negative m_F is preferred. For $\mathbf{B} = -B_0 \hat{\mathbf{z}}$, the opposite is true. The energy splitting between two m_F states is typically measured through the Larmor precession frequency, which gains a term proportional to d. For $\Delta m_F = 1$

$$\omega = \frac{|U(\Delta m_F = 1)|}{\hbar} = \left| -\gamma \Delta m_F B_0 - \frac{d \Delta m_F E_0}{\hbar F} \right| = \left| -\gamma B_0 - \frac{d E_0}{\hbar F} \right|. \tag{2.5}$$

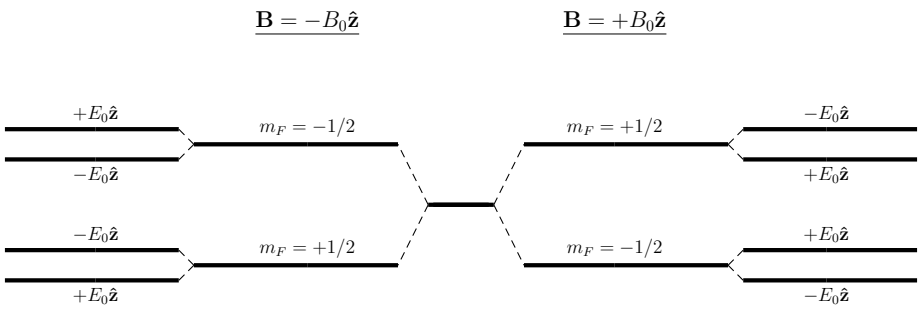

Figure 2.1: Energy levels if $d = +|d|$ for a 2-level system with a negative gyromagnetic ratio, like ^{3}He and ^{129}Xe. (Not to scale.)

Then, we can combine a pair of frequency measurements with opposite E_0 directions

$$|\omega(+E_0) - \omega(-E_0)| = \left|\frac{2dE_0}{\hbar F}\right| \tag{2.6}$$

In practice, there is some magnetic field drift between the two measurements, so, instead, for a pair of measurements we have for a spin-1/2 system

$$|\omega(+E_0) - \omega(-E_0)| = \left|\frac{4dE_0}{\hbar}\right| + \gamma\,\delta B. \tag{2.7}$$

where δB is the shift in the magnetic field between the two measurements. Even with very stable laboratory magnetic fields, the second term can easily dominate. To address this in the HeXeEDM experiment, we use a ^{3}He comagnetometer. Use of a ^{129}Xe-^{3}He comagnetometer was developed previously to take advantage of the ability to polarize multiple noble gas species at once using spin-exchange optical pumping [32] and was utilized in the Rosenberry experiment [22]. Other precision searches have also used a ^{129}Xe–^{3}He comagnetometer [33, 34]. Due to its small Z, the atomic EDM for ^{3}He is suppressed relative to the ^{129}Xe EDM. Therefore, the ^{3}He precession frequency was used to track changes in the magnetic field. Details for how the comagnetometer correction was applied in the analysis are discussed in Ch. V. For a single frequency measurement with $\mathbf{B} = +B_0\hat{\mathbf{z}}$ and

$\mathbf{E} = +E_0\hat{\mathbf{z}}$, we have for ^{129}Xe,

$$\omega_{\mathrm{Xe}} = \gamma_{\mathrm{Xe}} B_0 - \frac{2d_A(^{129}\mathrm{Xe})E_0}{\hbar} \tag{2.8}$$

and for ^{3}He

$$\omega_{\mathrm{He}} = \gamma_{\mathrm{He}} B_0 - \frac{2d_A(^{3}\mathrm{He})E_0}{\hbar}. \tag{2.9}$$

Since these are *simultaneous* measurements, the magnetic field dependence can be canceled to get

$$\omega_{\mathrm{Xe}} - \frac{\gamma_{\mathrm{Xe}}}{\gamma_{\mathrm{He}}}\omega_{\mathrm{He}} = -\frac{2E_0}{\hbar}\left[d_A(^{129}\mathrm{Xe}) - \frac{\gamma_{\mathrm{Xe}}}{\gamma_{\mathrm{He}}} d_A(^{3}\mathrm{He})\right] \approx -\frac{2d_A(^{129}\mathrm{Xe})E_0}{\hbar}. \tag{2.10}$$

For a phase-noise limited frequency measurement, the precision obtainable for d is given by [35, 36, 5]

$$\sigma_d \gtrsim \frac{\hbar}{2E_0}\sqrt{\frac{3}{\pi}}\frac{v_n}{V_0}\tau^{-3/2} \tag{2.11}$$

where v_n/V_0 is the signal-to-noise ratio (SNR), and τ is the observation time. Increasing the electric field and SNR, along with long observation times, is how we can reach the desired precision. How each of these parameters is optimized in the HeXeEDM experiment will be discussed in the following sections. Briefly, the electric field is limited to ∼3–5 kV/cm by high-voltage breakdown through the 0.5–1.5 bar ^{129}Xe-^{3}He-N_2 gas mixture [37] and the observation time is limited by a drift seen in the comagnetometer-corrected ^{129}Xe frequency. The source of these frequency shifts are detailed in Chapter IV. The SNR increases in the development of the experiment are detailed in Chapter III.

2.2 Spin precession

We will switch to a semiclassical picture of nuclear magnetic resonance [38, 39] to describe how spin precession is induced in the experiment. The holding magnetic field

$\mathbf{B} = B_0\hat{\mathbf{z}}$ exerts a torque on $\boldsymbol{\mu}$

$$\boldsymbol{\tau} = \frac{\mathrm{d}\mathbf{F}}{\mathrm{d}t} = \boldsymbol{\mu} \times \mathbf{B} \tag{2.12}$$

Using $\boldsymbol{\mu} = \gamma\mathbf{F}$, the equation of motion is

$$\frac{\mathrm{d}\boldsymbol{\mu}}{\mathrm{d}t} = \boldsymbol{\mu} \times \gamma\mathbf{B}. \tag{2.13}$$

It is helpful to define a rotating frame. For a general vector

$$\mathbf{f} = f_x\hat{\mathbf{x}}' + f_y\hat{\mathbf{y}}' + f_z\hat{\mathbf{z}}', \tag{2.14}$$

in a rotating (primed) system with angular velocity Ω_{rot},

$$\frac{\mathrm{d}\hat{\mathbf{x}}}{\mathrm{d}t} = \boldsymbol{\Omega}_{\text{rot}} \times \hat{\mathbf{x}}. \tag{2.15}$$

The time derivative of $\mathbf{f}$ in the lab frame is

$$\begin{aligned} \frac{\mathrm{d}\mathbf{f}}{\mathrm{d}t} &= \frac{\mathrm{d}f_x}{\mathrm{d}t}\hat{\mathbf{x}}' + \frac{\mathrm{d}\hat{\mathbf{x}}'}{\mathrm{d}t} + \frac{\mathrm{d}f_y}{\mathrm{d}t}\hat{\mathbf{y}}' + \frac{\mathrm{d}\hat{\mathbf{y}}'}{\mathrm{d}t} + \frac{\mathrm{d}f_z}{\mathrm{d}t}\hat{\mathbf{z}}' + \frac{\mathrm{d}\hat{\mathbf{z}}'}{\mathrm{d}t} \\ &= \left(\frac{\mathrm{d}\mathbf{f}}{\mathrm{d}t}\right)' + \boldsymbol{\Omega}_{\text{rot}} \times \mathbf{f} \end{aligned} \tag{2.16}$$

The equation of motion in the frame where $\boldsymbol{\mu}$ is rotating is then

$$\left(\frac{\mathrm{d}\boldsymbol{\mu}}{\mathrm{d}t}\right)' = \boldsymbol{\mu} \times \gamma\mathbf{B}_{\text{eff}} \tag{2.17}$$

where

$$\mathbf{B}_{\text{eff}} = \mathbf{B} + \frac{\boldsymbol{\Omega}_{\text{rot}}}{\gamma} \tag{2.18}$$

Notice that for $\mathbf{B} = B_0\hat{\mathbf{z}}$ we can solve for the equation of motion: if $\boldsymbol{\Omega}_{\text{rot}} = -\gamma B_0\hat{\mathbf{z}}$, $\mathbf{B}_{\text{eff}}$ is zero. As expected, this is the Larmor precession frequency. Since $\left(\frac{\mathrm{d}\boldsymbol{\mu}}{\mathrm{d}t}\right)' = 0$, $\boldsymbol{\mu}$ is fixed in the rotating frame. Next, we use the rotating frame to describe the two different ways spin

precession was induced in the experiment.

2.2.1 Pulsed NMR

For pulsed NMR, we applied an oscillating magnetic field resonant with the ^{129}Xe and ^{3}He precession frequencies. For simplicity, we discuss the single frequency case. Consider the effect of an oscillating magnetic field $\mathbf{B_1} = 2B_1 \cos\omega t$ on a spin in an applied magnetic field $\mathbf{B_0} = B_0\hat{\mathbf{z}}$. We can decompose this into two counter-rotating magnetic fields

$$\begin{aligned} \mathbf{B}_R &= B_1(\hat{\mathbf{x}}\cos\omega t + \hat{\mathbf{y}}\sin\omega t) \\ \mathbf{B}_L &= B_1(\hat{\mathbf{x}}\cos\omega t - \hat{\mathbf{y}}\sin\omega t) \end{aligned} \tag{2.19}$$

where ω can be positive or negative. Only one of these rotates in the same sense as the precession, and we neglect the other for the moment. In the frame rotating with frequency ω, B_1 is static:

$$\left(\frac{d\boldsymbol{\mu}}{dt}\right)' = \boldsymbol{\mu} \times [\hat{\mathbf{z}}'(\omega - \omega_0) + \hat{\mathbf{x}}'\gamma B_1] = \boldsymbol{\mu} \times \gamma \mathbf{B}_{\text{eff}}. \tag{2.20}$$

Here, we've substituted $\omega_0 = -\gamma B_0$. Note that in the rotating frame

$$\begin{aligned} \hat{\mathbf{x}}' &= \hat{\mathbf{x}}\cos\omega t + \hat{\mathbf{y}}\sin\omega t, \\ \hat{\mathbf{y}}' &= -\hat{\mathbf{x}}\sin\omega t + \hat{\mathbf{y}}\cos\omega t, \\ \hat{\mathbf{z}}' &= \hat{\mathbf{z}}. \end{aligned} \tag{2.21}$$

At resonance $\mathbf{B}_{\text{eff}} = B_1\hat{\mathbf{x}}'$ is a static field in the rotating frame and $\boldsymbol{\mu}$ will precess in the y'-z' plane, which allows one to use a B_1 pulse to rotate $\boldsymbol{\mu}$ to an angle in the y'-z' plane using

$$\theta = \gamma B_1 t_w, \tag{2.22}$$

where t_w is the pulse length. If off resonance, B_{eff} will be shifted toward $\hat{\mathbf{z}}$ or away from $\hat{\mathbf{z}}$ depending on whether the frequency is above or below the resonance frequency. We can write the magnitude of B_{eff} in terms of frequency as

$$-\gamma B_{\text{eff}} = -\frac{\gamma}{|\gamma|}\sqrt{(\omega-\omega_0)^2+\omega_1^2}, \tag{2.23}$$

where $\omega_1 = -\gamma B_1$. The angle between $\mathbf{B}_{\text{eff}}$ and $\hat{\mathbf{x}}'$ is $\alpha = \arctan\left(\frac{\omega_0+\omega}{\omega_1}\right)$ and $\sin\alpha = \frac{\omega_0+\omega}{-\gamma B_{\text{eff}}}$. In this case the spin precesses in a tilted y'-z' plane. The angle between $\boldsymbol{\mu}$ and $\mathbf{B_0}$ if at $t = 0$ they are aligned is

$$\cos\theta = \sin^2\alpha + \cos^2\alpha\cos(\gamma B_{\text{eff}} t). \tag{2.24}$$

The counter-rotating field, $\mathbf{B}_L$, causes a shift of the resonance frequency, known as the Bloch-Seigert shift. Assuming $|\omega_0+\omega| \gg |\omega_1|$, to lowest order the shift is [38]

$$\omega = \omega_0 + \frac{\omega_1^2}{4\omega_0}. \tag{2.25}$$

2.2.2 Field switch

For the field switch, instead of applying an oscillating field the B_0 direction is changed suddenly. $\boldsymbol{\mu}$ will move adiabatically with any field rotation unless $t_{\text{switch}} \ll \frac{2\pi}{\omega_0}$, where t_{switch} is the time taken to rotate the magnetic field direction $90°$. The resulting pulse error is $\delta\theta \approx \omega_0 t_{\text{switch}}$. There is an additional error from imperfect coil alignment. An advantage of this technique is pulse consistency; the pulse errors are repeatable along with any associated systematic effects.

2.2.3 Relaxation mechanisms

So far we have describing single system with magnetic moment $\boldsymbol{\mu}$. For an ensemble of spins, the magnetization is

$$\mathbf{M} = \frac{\mathbf{m}}{V} = \frac{1}{V}\sum \langle \boldsymbol{\mu} \rangle \tag{2.26}$$

Once spin precession is induced, the magnetization decays via two modes. Decay of the magnetization component transverse to the applied magnetic field B_0 is described by T_2, and decay of the magnetization component parallel to B_0, the longitudinal magnetization, is described by T_1. The phenomenological description of relaxation is provided by the Bloch equations,

$$\begin{aligned}
\frac{\mathrm{d}M_x(t)}{\mathrm{d}t} &= \gamma(\mathbf{M}\times\mathbf{B})_x - \frac{M_x(t)}{T_2} \\
\frac{\mathrm{d}M_y(t)}{\mathrm{d}t} &= \gamma(\mathbf{M}\times\mathbf{B})_y - \frac{M_y(t)}{T_2} \\
\frac{\mathrm{d}M_y(t)}{\mathrm{d}t} &= \gamma(\mathbf{M}\times\mathbf{B})_z - \frac{M_z(t)-M_0}{T_1}.
\end{aligned} \tag{2.27}$$

Notice that in the limit of $T_2 \to \infty$ and $T_1 \to \infty$ this reduces to the equation of motion for Larmor precession.

T_1 is the decay of the magnetization component parallel to the applied magnetic field and is the characteristic time of thermal equilibration. It is sometimes known as the spin-lattice relaxation time or wall relaxation time because it is caused by energy loss to the environment. This relaxation is accelerated by depolarizing interactions with the walls of the container. Additionally, magnetic field gradients can cause disorientation of the spin after collisions resulting in further decay of the longitudinal magnetization. The gradient dependence of T_1 for a spin-1/2 system is given by [40, 41, 42]

$$\frac{1}{T_1} = D\frac{|\boldsymbol{\nabla}B_x|^2 + |\boldsymbol{\nabla}B_y|^2}{B_0^2(1+\omega_0^2\tau_c^2)} \tag{2.28}$$

where D is the diffusion constant and τ_c is the time between collisions. The factor $(1+\omega_0^2\tau_c^2)^{-1} \approx 1$ for the pressures and magnetic fields used in this experiment. The diffusion

Species (j)	$D^0_{\text{He-j}}$ [bar cm^2/s]	Ref.	$D^0_{\text{Xe-j}}$ [bar cm^2/s]	Ref.
He	1.9	[43]	0.55	[44, 45, 46, 47, 48]
Xe	0.61	[44]	0.06	[44]
N_2	0.77	[44]	0.13 / 0.21	[46, 49] / [50]

Table 2.1: Self and mutual diffusion constants for He, Xe and N_2.

constant for species i in a mixture of gases j is given by

$$\frac{1}{D_i} = \sum_j \frac{p_j}{D_{ij}} \tag{2.29}$$

where p_j is the partial pressure of species j and D^0_{ij} are given in Table 2.1.

T_2 is known as the spin-spin relaxation time. T_2 is caused by dipole-dipole interactions between the spins and by dephasing of the spins in different parts of the cell due to magnetic field inhomogeneity. In the motional narrowing regime [51] the former is negligible [52, 53] and typically the observed transverse decay time is denoted as T_2^*.

For a spherical cell, T_2^* is given by [54]

$$\frac{1}{T_2^*} = \frac{1}{2T_1} + \frac{8\gamma^2 R^4}{175D}|\boldsymbol{\nabla} B_z|^2 \tag{2.30}$$

and for a cylindrical cell with length L and radius R, where the cell axis is aligned with $\hat{\mathbf{z}}$ [54]

$$\frac{1}{T_2^*} = \frac{1}{2T_1} + \frac{\gamma^2 L^4}{120D}\left(\frac{\partial B_z}{\partial z}\right)^2 + \frac{7\gamma^2 R^4}{96D}\left(\frac{\partial B_z}{\partial x}\right)^2 \tag{2.31}$$

2.3 Spin-Exchange Optical Pumping

2.3.1 Introduction

For a two-level system, polarization is defined as

$$P = \frac{|N_\uparrow - N_\downarrow|}{N_\uparrow + N_\downarrow} = \frac{|N_\uparrow - N_\downarrow|}{N} \tag{2.32}$$

where $N_\uparrow$ is the number of atoms in the $m_F = +1/2$ "spin-up" state and $N_\downarrow$ is the number of atoms in the $m_F = -1/2$ "spin-down" state. For a general F,

$$P = \frac{1}{F}\frac{\sum_{m_F} m_F N(m_F)}{\sum_{m_F} N(m_F)} \tag{2.33}$$

The thermal or Boltzmann polarization depends on the temperature and the magnitude of the applied magnetic field. The magnetization is

$$M_0 = \frac{N\gamma\hbar}{Z}\sum_{m_F=-F}^{m=+F} m_F \exp\left(\frac{\gamma\hbar m_F B_0}{k_B T}\right) \tag{2.34}$$

where Z is the Boltzmann distribution

$$Z = \sum_{m_F=-F}^{m_F=+F} \exp\left(\frac{\gamma\hbar m_F B_0}{k_B T}\right) \tag{2.35}$$

The polarization can also be written as $P = M_0/M_{\text{max}}$, where $M_{\text{max}} = N\gamma\hbar/2$ for $F = 1/2$. For $B_0 = 1$ T, $T = 300$ K, for ^{3}He

$$P = \frac{M_0}{M_{\text{max}}} \approx \frac{\gamma\hbar B_0}{2k_B T} = 2.6 \times 10^{-6} \tag{2.36}$$

Similarly, for ^{129}Xe, it is 9.4×10^{-7}. This can be increased with very strong magnetic fields combined with very low temperatures, but a more efficient technique is hyperpolarization using optical pumping.

Ref. [55] provides the detailed theory of optical pumping and Ref. [56] provides the theory of optical pumping of ^{129}Xe and ^{3}He. The general theory is quite complex, but we can make some simplifications for our implementation of spin-exchange optical pumping in the HeXeEDM experiment. Below we provide a brief overview and a model for determining equilibrium polarizations.

Spin-exchange optical pumping (SEOP) is a method to hyperpolarize noble gases. In SEOP, an alkali metal vapor is polarized using circularly polarized light. The alkali valence electron polarization is transferred to the noble gas via spin-exchange collisions. SEOP allows for polarization of large quantities of gas as opposed to metastability-exchange optical pumping (MEOP) which can polarize smaller pressures of ^{3}He. MEOP is not suited for heavier noble gases like ^{129}Xe [57]. SEOP also allows for simultaneous polarization of multiple noble gas species.

2.3.2 Optical pumping of Rubidium

We use Rb as the alkali metal because of its high vapor pressure at temperatures easily achievable in the lab, typically $80 - 150^{\circ}$ C. Additionally, the 794.7 nm laser required for the D1 transition is now readily available in the form of commercial diode lasers, and the D2 transition is sufficiently far away at 780.0 nm.

Alkali metals are characterized by their $n\mathrm{s}^1$ valence electron. For Rb, the unpaired electron is in the 5s orbital. Natural rubidium has stable isotopes ^{85}Rb (72.2%) with nuclear spin $I = 5/2$ and ^{87}Rb (27.8%) with $I = 3/2$. In the presence of an applied magnetic field B_0, the Hamiltonian is

$$\mathcal{H}_a = A_a \mathbf{I}_a \cdot \mathbf{J}_a + g_J \mu_B J_z B_0 - \frac{\mu_a}{I_a} I_{az} B_0 \tag{2.37}$$

where we've introduced the index a is for the alkali, Rb, and $\mathbf{J}_a = \mathbf{S}_a + \mathbf{L}_a$ is the electron total angular momentum. The first term describes the hyperfine interaction; the second

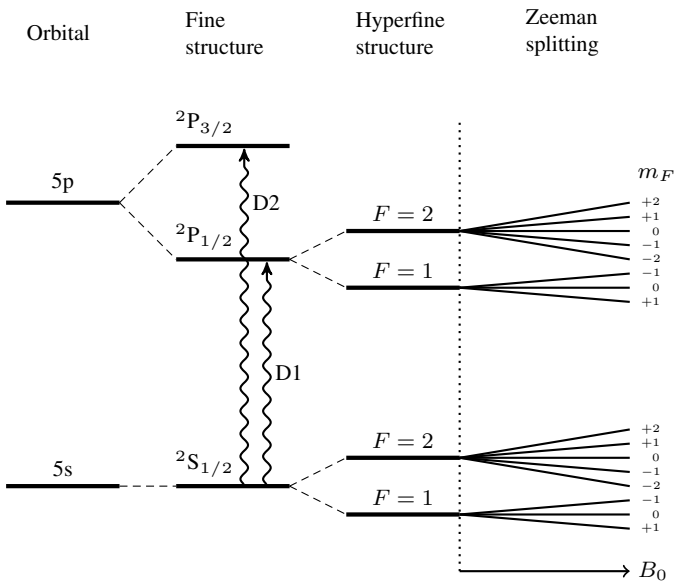

Figure 2.2: ^{87}Rb energy levels under an applied magnetic field, with $I = 3/2$. For ^{85}Rb, $I = 5/2$, so the hyperfine levels will be $F = 2, 3$ instead. Not to scale.

term describes the electron spin coupling to the magnetic field; the last term describes the Rb nuclear spin coupling to the magnetic field. SEOP uses magnetic fields on the order of mT, so the second term is of order 10^{-7} eV and the last term 10^{-10} eV. The hyperfine splittings are of order 10^{-5} eV, so the first term dominates. Therefore, the eigenstates of $\mathcal{H}_a$ are also the eigenstates of total atomic angular momentum $\mathbf{F}_a$.

Our first simplification comes from the fact typical SEOP applications are in the high-pressure regime. For us, the total optical pumping cell pressure is one or more bars. In this regime, the alkali hyperfine structure is unresolved due to pressure broadening caused by collisions with noble gas atoms and nitrogen [58]. The timescale between collisions is short enough that the hyperfine interaction is not able to torque the nuclear spin [59]. Because the pumping and collisional processes are fast with respect to the nuclear polarization, we can treat the nuclear spin as a conserved quantity. Now, the allowed states are $F_a = I_a + 1/2$ or $F_a = I_a - 1/2$. N_2 is included as a buffer gas because Rb-N_2 collisions provide a channel to rapidly transfer Rb excitation energy to rotational and vibrational modes of N_2 and therefore suppress light-trapping from radiative decay of the excited state [60, 61, 62].

The spin-exchange interaction for polarizing noble gases is discussed in the next section. The other relevant spin-dependent collisional Hamiltonians include a spin-rotation interaction [56]

$$\mathcal{H}_{sr} = \gamma \mathbf{N} \cdot \mathbf{S}_a, \tag{2.38}$$

where N is the relative angular momentum of a colliding pair. Here, $\gamma = \gamma(R)$ is the coupling constant and depends on the interatomic separation R between the colliding pair. $\gamma \to 0$ rapidly as R increases. The spin-rotation interaction results in relaxation or "spin destruction" for binary Rb-Rb and Rb-^{3}He collisions. The next interaction is an alkali-alkali spin-exchange interaction [56]

$$\mathcal{H}_{ase} = \eta \mathbf{S}_i \cdot \mathbf{S}_j, \tag{2.39}$$

where again the coupling constant $\eta = \eta(R)$. There is an additional alkali-alkali relaxation channel that couples to the relative angular momentum of the colliding pair. Since this is relevant only at high alkali densities, we will neglect this term. For HeXeEDM we polarize at 70-150°C and additional relaxation due to high Rb density becomes relevant at temperatures $\geq$ 200°C.

With the information above we can define a simplified Rb optical pumping scheme illustrated in Fig. 2.3. In this model, alkali valence electrons in the $S_{1/2}$ state with $m_J = -1/2$ absorb incident 794.7 nm circularly polarized σ^+ light and are excited to the $P_{1/2}$ state with $m_J = +1/2$. The excited state decays to either of the $S_{1/2}$ ground state sublevels via radiative decay and N_2 collisions. Collisions with noble gas and N_2 mix the excited states so that, if radiative decay is effectively suppressed, the excited states decay with equal probability to either ground state. The branching ratio for radiative decay is [62, 63]

$$B_\gamma \approx \frac{3}{3 + p_{\mathrm{N}_2}}, \tag{2.40}$$

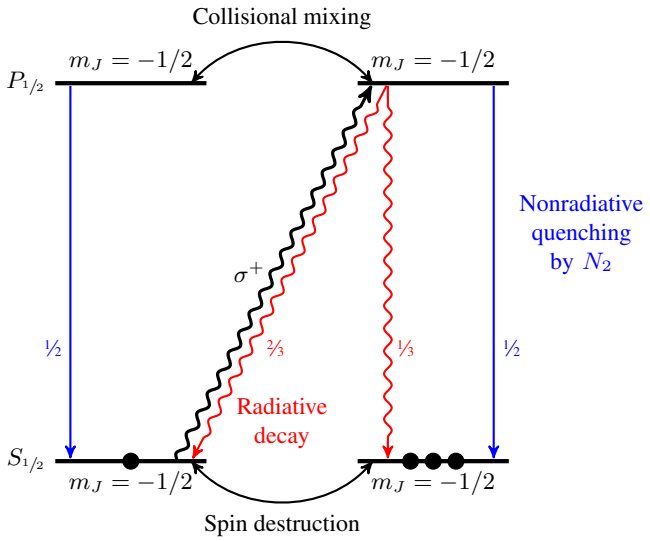

Figure 2.3: Rb optical pumping scheme, neglecting Rb nuclear spin.

where p_{N_2} is the partial pressure of N_2 at 300 K. For the rest of this discussion, we will assume that the N_2 density is sufficient that radiative quenching is negligible. Depolarization, or spin destruction, of the optically pumped Rb is dominated by collisions with other Rb atoms, N_2, and the noble gases. As the σ^+ light penetrates the cell, the Rb vapor toward the front of the optical pumping cell reaches an equilibrium polarization, and since the $m_J = +1/2$ ground state cannot absorb σ^+, the vapor becomes effectively transparent and the light can penetrate further into the cell. Eventually all the vapor in the cell reaches an equilibrium polarization P_{Rb}. A model incorporating the effects described above for estimating P_{Rb} has been detailed in [62]. Briefly, the photon flux $\Phi(\nu, z)$ is a function of frequency and axial position through the cell z. It's z dependence is

$$\frac{\mathrm{d}\Phi(\nu, z)}{\mathrm{d}z} = -\lambda_{\sigma^+}^{-1}(\nu, z)\Phi(\nu, z) \tag{2.41}$$

where λ_{σ^+} is the absorption length of incident, right-circularly polarized light. The scattering rate of circularly polarized photons per alkali atom in an unpolarized vapor is

$$\gamma_{\text{opt}}(z) = \int \Phi(\nu, z)\sigma_s(\nu)d\nu \tag{2.42}$$

where σ_s is the cross-section for scattering of unpolarized light

$$\sigma_s = \frac{(\Gamma/2)^2}{(\nu - \nu_0)^2 + (\Gamma/2)^2}\sigma_0 \tag{2.43}$$

where Γ is the Rb D1 absorption linewidth and σ_0 is the peak scattering cross section. Both are pressure-dependent. The absorption linewidth can be written as

$$\lambda_{\sigma^+}^{-1}(\nu, z) = \lambda_0^{-1}(\nu, z)\frac{\Gamma_{\text{SD}}}{\gamma_{\text{opt}}(z) + \Gamma_{\text{SD}}} \tag{2.44}$$

where Γ_{SD} is the rate of spin destruction given by

$$\Gamma_{\text{SD}} = k^{\text{SD}}_{\text{Rb-Rb}}[\text{Rb}] + k^{\text{SD}}_{\text{Rb-N}_2}[\text{N}_2] + k^{\text{SD}}_{\text{Rb-ng}}[\text{ng}], \tag{2.45}$$

where ng refers to the noble gas and the spin-destruction rate constants can be found in Table 2.2. Rubidium density as a function of temperature can be estimated using [64]

$$[\text{Rb}] = \frac{10^{9.318 - 4040/T}}{k_B T}. \tag{2.46}$$

The above equations can be used to determine $P_{\text{Rb}}(z)$

$$P_{\text{Rb}}(z) = \frac{\gamma_{\text{opt}}(z)}{\gamma_{\text{opt}}(z) + \Gamma_{\text{SD}}} \tag{2.47}$$

from which the average polarization in the cell $\bar{P}_{\text{Rb}}$ can be determined. This model assumes low Rb densities so that diffusion effects can be neglected.

Species (j)	$k^{\mathrm{SD}}_{\mathrm{Rb}-j}$ [cm^3/s]	Ref.	$k^{\mathrm{SE}}_{\mathrm{Rb}-j}$ [cm^3/s]	Ref.
Rb	8×10^{-13}	[65, 66]		
^{3}He	$2 \times 10^{-18^*}$	[66, 67]	6.74×10^{-20}	[67]
^{129}Xe	9.07×10^{-15}	[68]	2.10×10^{-16}	[69]
N_2	$1 \times 10^{-17^*}$	[66, 67]		

Table 2.2: Spin destruction and spin exchange constants for Rb-^{3}He, Rb-^{129}Xe and Rb-N_2. The starred values are temperature dependent and the numbers listed are for 200°C. More detail on alkali-alkali, alkali-^{3}He, and alkali-N_2 measurements is given in Appendix D. of Ref. [67] including a fit to the temperature dependence of the spin destruction constants using all published measurements. There are considerable (factors of 2) uncertainties for these values. $k^{\mathrm{SD}}_{\mathrm{Rb}-\mathrm{Xe}}$ and $k^{\mathrm{SD}}_{\mathrm{Rb}-\mathrm{Xe}}$ are listed for ^{129}Xe-Rb binary collisions. For estimations of polarization in OPCs, $k^{\mathrm{SD}}_{\mathrm{Rb}-\mathrm{Xe}}$ and $k^{\mathrm{SE}}_{\mathrm{Rb}-\mathrm{Xe}}$ were arbitrarily increased by a factor of 2 to account for spin-rotation of Xe in van der Waals molecules. A more precise estimation of the total ^{129}Xe spin-exchange and destruction rates is discussed in Ref. [70].

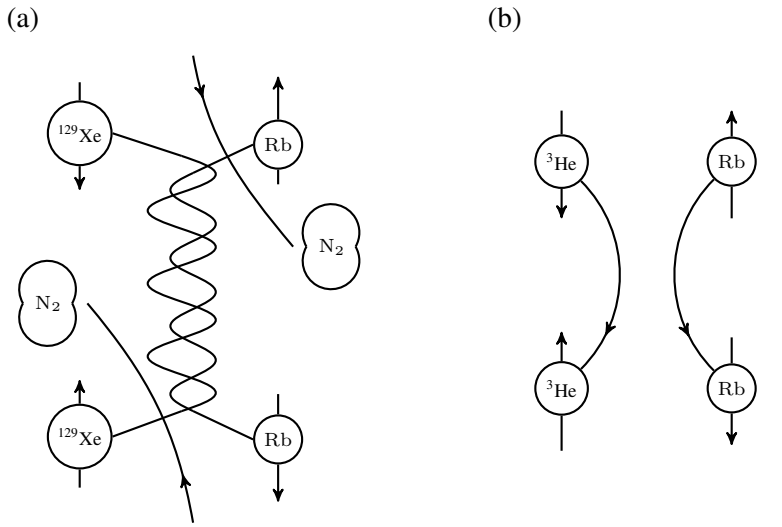

Figure 2.4: Spin exchange collisions between (a) Rb and ^{129}Xe, typically mediated by short-lived van der Waals molecules and (b) Rb and ^{3}He, typically binary collisions. Figure adapted from [58].

2.3.3 Noble gas polarization through spin-exchange collisions

Polarization of the noble gases ^{3}He and ^{129}Xe is achieved via spin-exchange interactions with polarized Rb. The free Hamiltonian for the noble gases is

$$\mathcal{H}_{ng} = -\frac{\mu_{ng}}{I_{ng}} I_{ngz} B_0. \tag{2.48}$$

Spin-exchange occurs through a Fermi contact interaction

$$\mathcal{H} = \alpha \mathbf{I}_{ng} \cdot \mathbf{S}_a \tag{2.49}$$

where $\mathbf{I}_{ng}$ is the noble gas nuclear spin and S_a is the alkali electron spin. $\alpha = \alpha(R)$ and rapidly approaches zero as the interatomic separation increases.

For ^{3}He, electron spin polarization is exchanged through binary Rb-^{3}He collisions. For Xe, spin polarization is exchanged via short-lived van der Waals molecules formed with Rb, ^{129}Xe and N_2. The interaction includes both Eqs. 2.38 and 2.49, where $\mathbf{N}$ is the rotational angular momentum of the molecule and also contributes to spin relaxation.

We can model noble gas polarization with the following rate equation [71]

$$\frac{\mathrm{d}P_{\mathrm{ng}}}{\mathrm{d}t} = k^{\mathrm{SE}}_{\text{Rb-ng}}[\mathrm{Rb}](P_{\mathrm{Rb}} - P_{\mathrm{ng}}) - \Gamma_{\mathrm{ng}} P_{\mathrm{ng}} \tag{2.50}$$

where $k^{\mathrm{SE}}_{\text{Rb-ng}}$ is the spin-exchange rate constant, and $\Gamma_{\mathrm{ng}} = 1/T_1$ is the room-temperature relaxation rate. The steady-state solution is

$$P_{\mathrm{ng}} = P_{\mathrm{Rb}} \frac{k^{\mathrm{SE}}_{\text{Rb-ng}}[\mathrm{Rb}]}{k^{\mathrm{SE}}_{\text{Rb-ng}}[\mathrm{Rb}] + \Gamma_{\mathrm{ng}}} \tag{2.51}$$

It has been shown experimentally [72, 73] that there is a phenomenological factor X dependent on the surface-to-volume ratio of the optical pumping cell that limits the maximum

achievable polarization

$$P_{\text{ng}} = P_{\text{Rb}} \frac{k^{\text{SE}}_{\text{Rb-ng}}[\text{Rb}]}{k^{\text{SE}}_{\text{Rb-ng}}[\text{Rb}](1+X) + \Gamma_{\text{ng}}}. \tag{2.52}$$

There are additional experimental factors that limit the maximum achievable polarization [74, 75].

In the HeXeEDM experiment, we used a 1-2 bar gas mixture of 18%Xe (90 $\pm$ 2% ^{129}Xe), 73% ^{3}He, and 9% N_2 in an optical pumping cell (OPC) containing Rb.

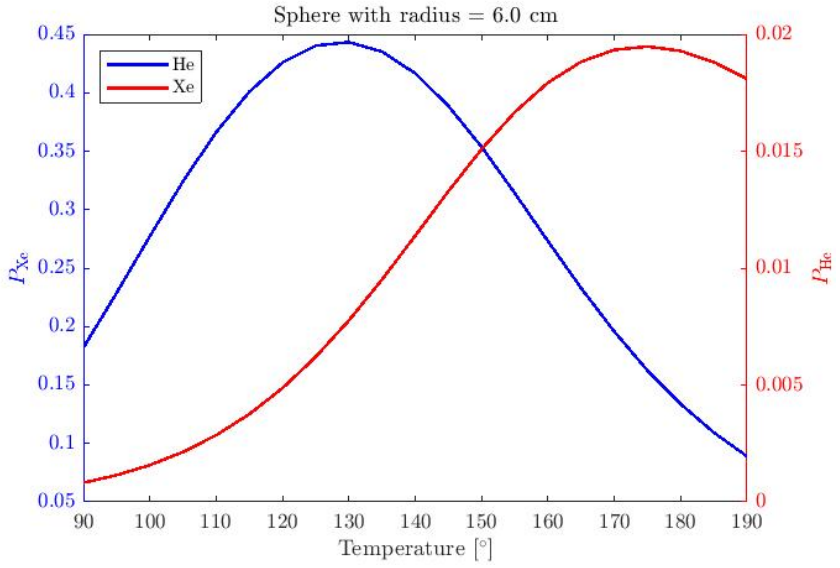

Figure 2.5: Plot of P_{Xe} and P_{He} vs. temperature calculated for a typical refillable SEOP cell using the model in the text and rate coefficients from Table 2.2.

2.4 Magnetically Shielded Rooms

A magnetically shielded room (MSR) is a space enclosed by sheets of a high magnetic permeability material. μ-metal is a nickel-iron soft ferromagnetic alloy with relative permeability $\mu_r = \mu/\mu_0 \sim 80,000 - 100,000$. MSRs provide shielding from external static and slowly varying magnetic fields. They typically also provide shielding from external electromagnetic noise.

HeXeEDM requires a magnetically shielded environment for several reasons: (1) SQUID magnetometers (discussed in the next section) require a magnetically shielded environment; (2) large magnetic field gradients reduce T_2^*, which limits our observation time; (3) the magnetic field must be temporally stable across our smallest analysis time unit, typically 5–20 seconds, in order to make the correction (see Chap. V).

From the first experimental campaign in December 2013 until June 2017, we used the TUM (Technical University of Munich) MSR at the FRM-II (Munich Research Reactor) in Garching, Germany. From June 2017 to present we use the Berlin Magnetically Shielded Room (BMSR-2) at Physikalisch Technische Bundesanstalt (PTB) Berlin.

2.4.1 TUM MSR

The TUM MSR is a portable magnetically shielded room achieving a residual magnetic field $<$1 nT and residual magnetic field gradient of $<$300 pT/m. The room is roughly $2\times2\times2$ m^3 and is enclosed by an outer shield of two 1 mm thick layers of μ-metal and an additional 8 mm thick aluminum layer for rf shielding. The passive shielding factor is $\sim$300 for frequencies less than 0.01 Hz [76]. The TUM MSR was created for a neutron EDM experiment and also has an inner shield [77] that we did not use.

2.4.2 BMSR-2

The BMSR-2 is a 24 ton 8-layer MSR comprised of seven layers of μ-metal of varying thicknesses and a 10 mm thick aluminum rf-shielding layer enclosing a space of $2.9\times2.9\times2.8$ m^3. BMSR-2 features a passive shielding factor of $\sim$75000 for frequencies less than 0.01 Hz and 10^8 above 6 Hz. Similar to the TUM MSR, the residual magnetic field is $<$1 nT in the working area of one cubic meter in the center of the room and the residual magnetic field gradient is $< 0.5\ \mathrm{nT/m}$. There are additional compensation coils outside the room to provide active shielding of external magnetic fields [78, 79].

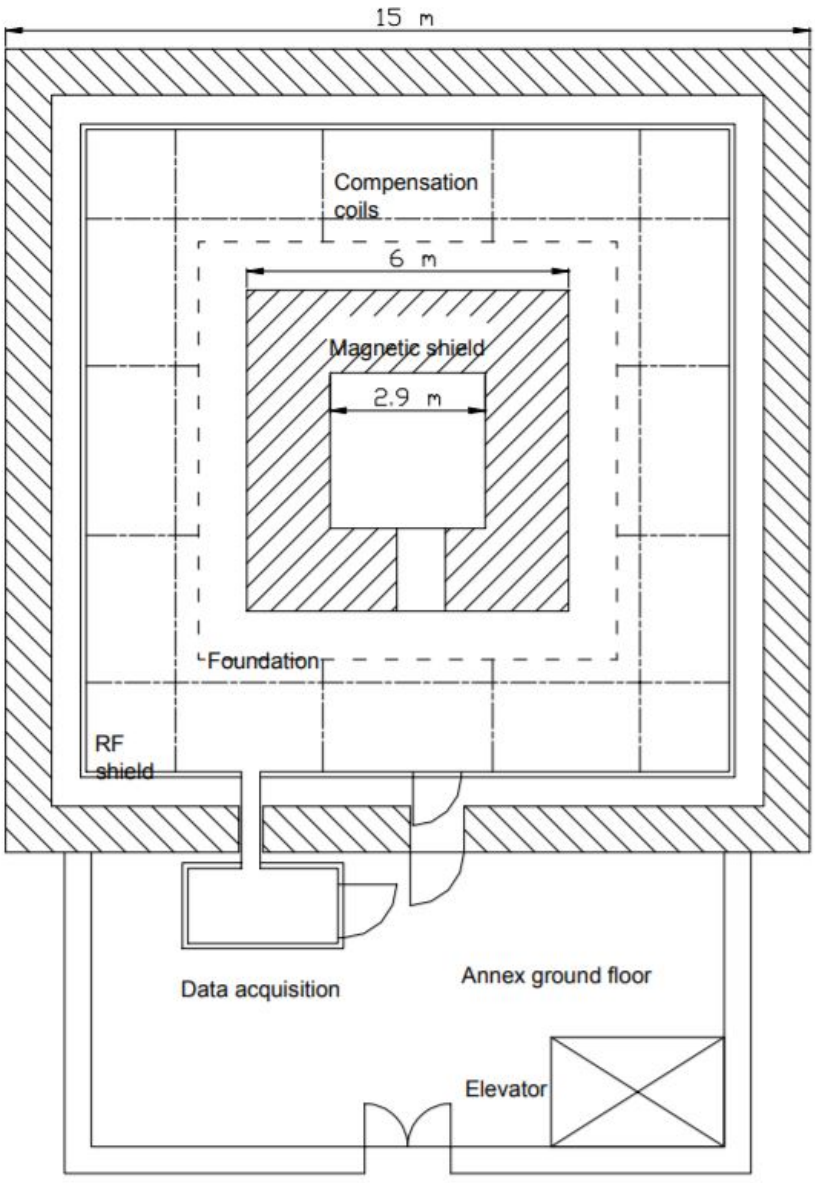

Figure 2.6: Structure of the BMSR-2 and entrance from Ref. [78].

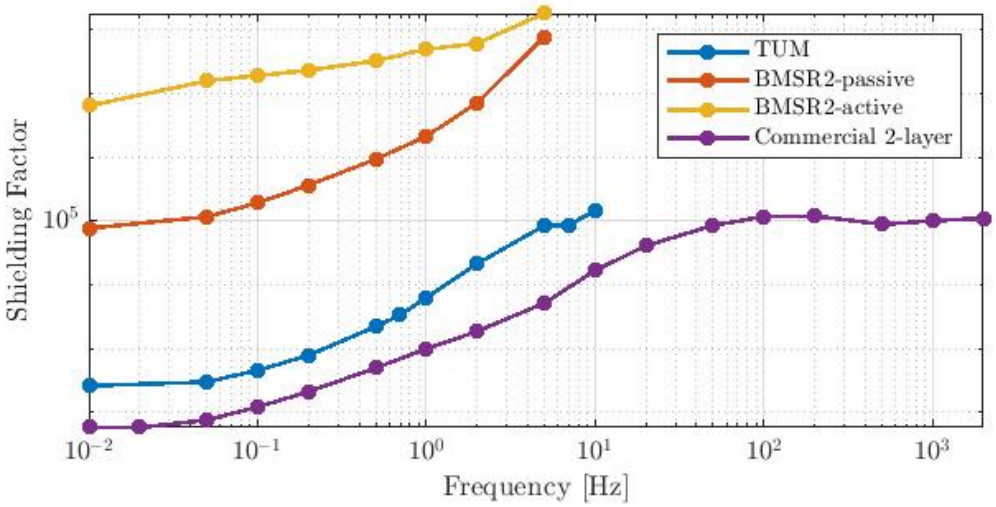

Figure 2.7: Shielding factor of BMSR-2 compared to the TUM MSR.

2.5 SQUID magnetometry

The typical magnitude of the static magnetic field B_0 is 1–3 μT, corresponding to ^{129}Xe and ^{3}He frequencies of $\sim$12–35 Hz and $\sim$32–97 Hz, respectively. For low frequencies, the most sensitive magnetometers are superconducting quantum interference devices (SQUIDs) and spin-exchange-relaxation-free (SERF) magnetometers. However, SERFs require suppression of spin-exchange relaxation by zeroing of the magnetic field [80]. SQUIDs are optimized for a relative magnetic field measurement (like a precessing signal) in a large constant magnetic field. SQUIDs also have large bandwidth so we can simultaneously measure both ^{129}Xe and ^{3}He precession. A trade-off is that they are susceptible to rf and other frequency noise, and therefore need to be operated in a low-noise environment. The dynamic range is limited by the SQUID electronics and environmental noise, but is large at low frequencies [81, 82]. SQUIDs operate below the critical temperature T_c of the superconductor. We used conventional Nb-Al_xO_y-Nb trilayer SQUIDs which require low-noise liquid helium cryostats kept at 4 K.

SQUIDs operate as magnetic-flux-to-voltage transducers. We used low T_c dc SQUIDs, which typically have a sensitivity of $\sim 10^{-6}\ \Phi_0$, where $\Phi_0 = h/(2e)$ is the magnetic flux

quantum [82]. The magnetic field sensitivity is $\delta B = \delta\Phi/A_L$, where A_L is the area of the SQUID loop. All of the dc SQUIDs used were PTB-fabricated W9L chips with a sensitive area of 4.4 mm^2 and intrinsic white noise of 1.3 fT/$\sqrt{\text{Hz}}$ [83, 81]. The operating white noise limit depended on the environmental thermal noise. For us, Johnson noise in the insulating materials of the dewar limits the SQUID noise level. While there is potential for improvement by using different insulating material [84], there is another limitation from the MSR thermal noise, which is 2 fT/$\sqrt{\text{Hz}}$ for the BMSR-2 [79]. The dewar construction limits the distance between the closest SQUID and the cell. The signal-to-noise depends on this distance, since the signal strength decreases as $1/r^3$.

2.5.1 Cube-I

The Cube-I system consists of an array of six SQUIDs in a 30 cm×30 cm×30 cm cube as described in Ref. [85] but in a smaller dewar. The cold-warm-distance (CWD) is the distance between the closest SQUID along the dewar axis, labeled Z1, and the bottom of the dewar. For the Cube-1 distance this was 6.0±0.2 cm [86].

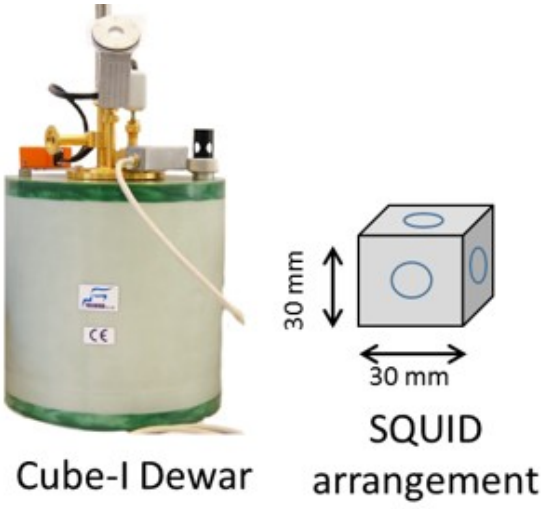

Figure 2.8: The Cube-I SQUID system.

2.5.2 MRX-I

The MRX-I system is similar to the Cube-I system in that it also contains an array of six SQUIDs, but the top SQUID, Z2, is 12 cm away from Z1. The design allows for the Z-SQUIDs to be used as a gradiometer to cancel vibrations and any long-range magnetic disturbances seen in both SQUIDs. A Z-gradiometer was not useful in the Cube-I system because Z2 was close enough to pick up enough precession to reduce the signal strength significantly when combined with Z1. The CWD for the MRX-I system is 1.2±0.2 cm.

For measurements in 2018, we used a similar system, MRX-III, which had only Z1 and Z2 SQUIDs and a cold warm-distance of 0.8±0.2 cm.

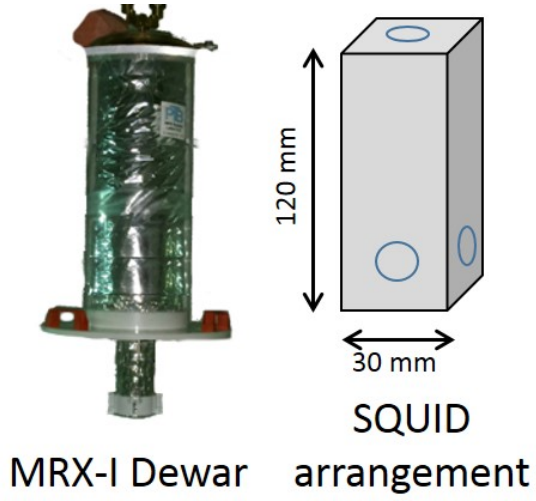

Figure 2.9: The MRX-I SQUID system.

2.6 Cell production

There were three kinds of cells used in the experiment: sealed glass bulbs containing a mixture of Rb, N_2 and ^{3}He and/or ^{129}Xe; refillable optical pumping cells (OPCs) also containing Rb, N_2 and ^{3}He and/or ^{129}Xe; valved EDM measurement cells with silicon electrodes. A few double-chambered sealed cells were made with one chamber for optical pumping and another chamber with electrodes for measuring (see Fig. 2.10). Refillable

OPCs were able to be refilled using a gas-filling station. The OPCs were installed within a SEOP polarizer and were used to fill valved EDM measurement cells.

The sealed cells were used primarily in the early stages of the experiment and for testing purposes thereafter. In the next chapter, we detail the issues faced when using the sealed cells for measurements. Primarily, rubidium vapor in the cell reduces the breakdown high-voltage and eddy currents in the Rb caused by changing magnetic fields during transport result in unwanted magnetic fields and gradients in the measurement volume.

Sealed cells and OPCs for experimental campaigns 1-5 were made at the University of Michigan. The valved cells with smaller electrodes used for the measurement campaigns in the summers of 2017 and 2018 (named HeXe2017 and HeXe2018, respectively) were made at Jülich, Germany, by Patrick Pistel. At the University of Michigan, Roy Wentz did the glass work at the Department of Chemistry Glass Shop. Skyler Degenkolb prepared the sealed glass bulbs and all Michigan cells with electrodes and detailed the procedure in Ref. [87]. We also produced OPCs at Michigan. The setup and procedure are similar and outlined below.

2.6.1 Refillable OPCs

The standard protocol for cleaning is as follows:

1. The cell is cleaned with a warm solution of Alconox detergent in distilled water.
2. Then, it is rinsed three times with methanol, followed by three rinses with deionized water.
3. Pirahna solution, 97% H_2SO_4 and 30% H_2O_2, is mixed in a 7:3 ratio, poured into the cell and allowed to sit for a minimum of one hour.
4. The piranha solution is drained, followed by three rinses with deionized water.
5. To remove additional traces of acid, the cell is rinsed three times with high purity methanol.
6. Finally, the cell is rinsed three times with deionized water.

7. The cell is baked in an oven at 80° to 100° C for 12–24 hours to evaporate any remaining water.

After cleaning, the OPC is attached to the cell filling station. A rubidium ampoule is opened and added to the sidearm, and the open port is sealed using an oxygen-propane torch. The OPC is then pumped out while the main volume is heated using heating tape at 100° to 200° C for 12–48 hours to reach a base pressure of 10^{-7}–10^{-8} Torr. After cooling the OPC, the rubidium is "chased" from the sidearm using the torch into the cell where it recondenses on the unheated surface. The sidearm containing the rubidium ampoule is then pulled off and sealed using the torch. Then, the desired gas mixture is added to the cell. Typically, xenon is added first and condensed using a liquid nitrogen bath outside the cell while ^{3}He and then N_2 is added.

2.6.2 Valved EDM cells

Early cells with electrodes produced at Michigan used a modified hydroxide-catalysis bonding method to attach silicon wafers to the cell [87]. For HeXe2017 and HeXe2018, we used cells produced at Jülich which used diffusion bonding [88] to attach the silicon wafers.

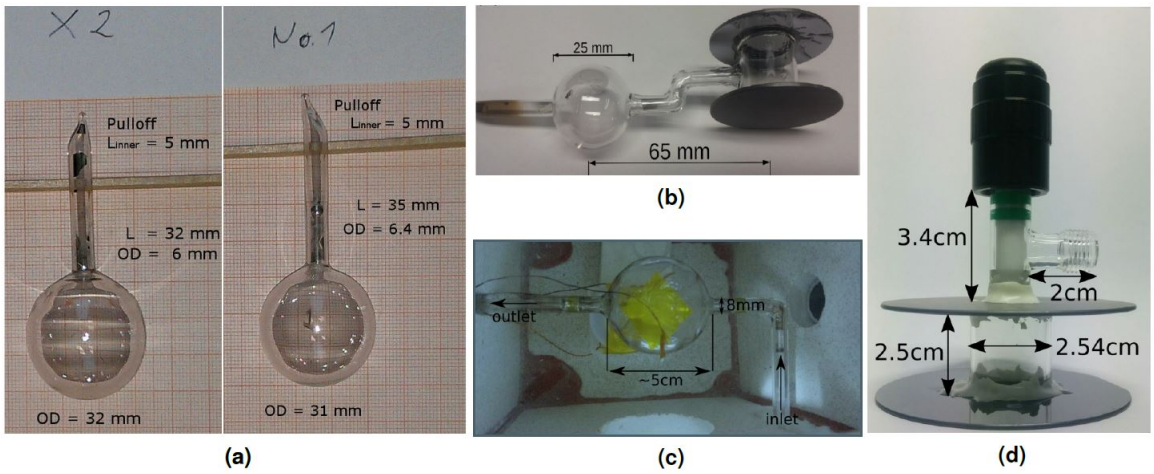

Figure 2.10: Different kinds of cells used in the experiment: (a) sealed cells, (b) a double-chambered cell, (c) refillable optical pumping cell (OPC), and (d) valved EDM measurement cell. Figure from Ref. [37].

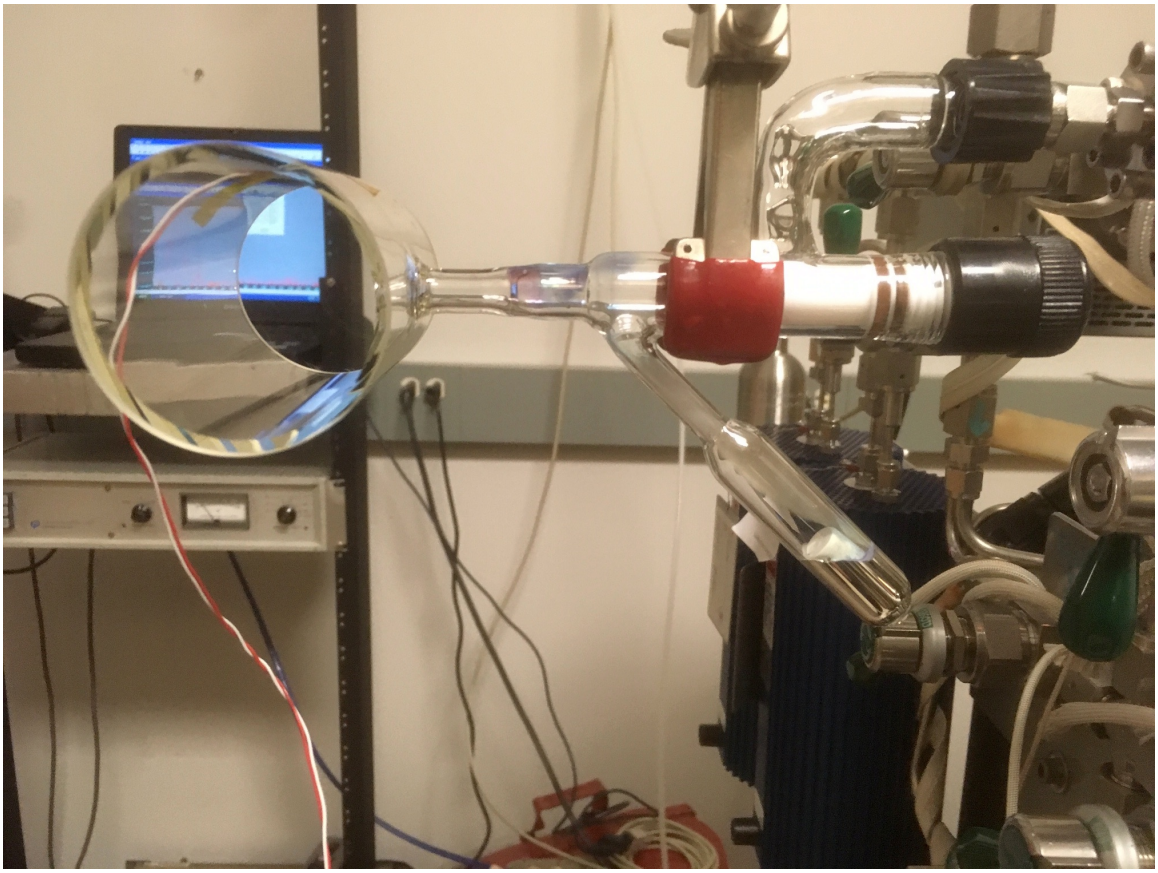

Figure 2.11: A cylindrical OPC used during measurements at PTB. Here, it is attached to the gas system at Michigan prior to chasing rubidium into the cell from the ampoule in the sidearm.

Cell name	Type	Xe / ^{3}He / N_2 [mbar]	Source	Description
Maya	Sealed	∼1000 tot ^{3}He, N_2 only	EB	n/a
SDHX1	Sealed	113 (nat.) / 667 / 67	SD	3 cm bulb
X1	Sealed	150 (nat.) / 560 / 50	SD	3 cm bulb
X2	Sealed	150 (nat.) / 560 / 50	SD	3 cm bulb
X3	Sealed	150 (nat.) / 560 / 50	SD	3 cm bulb
1	Sealed	112 (enr.) / 777 / 47	SD	3 cm bulb
2	Sealed	112 (enr.) / 777 / 47	SD	3 cm bulb
3	Sealed	112 (enr.) / 777 / 47	SD	3 cm bulb
4	Sealed	112 (enr.) / 777 / 47	SD	3 cm bulb
F1	Sealed double-chamber	59 (enr.) / 784 / 51	SD	3 cm bulb, l≈25 mm, OD≈25 mm, ∼50 mm electrodes
F3	Sealed double-chamber	59 (enr.) / 784 / 51	SD	3 cm bulb, l≈25 mm, OD≈25 mm, ∼50 mm electrodes
F4	Sealed double-chamber	59 (enr.) / 784 / 51	SD	3 cm bulb, l≈25 mm, OD≈25 mm, ∼50 mm electrodes
E2	Valved EDM	n/a	SD	2 mm thick GE180, l=24.8 mm, OD 21.2 mm, ∼60 mm electrodes
PP1	Valved EDM	n/a	PP	Duran/Pyrex l=18.5 mm, ID=20.5 mm, electrodes: D=30 mm, 2 mm thick silicon
PP2	Valved EDM	n/a	PP	Duran/Pyrex l=21.8 mm, ID=20.4 mm, electrodes: D=30 mm, 2 mm thick silicon
PP3	Valved EDM	n/a	PP	Duran/Pyrex l=21.8 mm, ID=20.4 mm, electrodes: D=30 mm, 2 mm thick silicon

Table 2.3: Table of all measurement cells mentioned in this work. All sealed cells also contain rubidium. Natural Xe contains $\sim 26\%$ ^{129}Xe and enriched is $\sim 90\%$ ^{129}Xe. Sources: Earl Babcock (EB), Skyler Degenkolb (SD), Patrick Pistel (PP).

CHAPTER III

The HeXeEDM Experiment: Apparatus

Development of the HeXeEDM experiment began in 2013. The first experimental campaign that brought together the collaboration for measurements at an MSR was in 2013 with a goal of measuring spin precession of ^{129}Xe and ^{3}He with SQUIDs. Since then there has been about one experimental campaign per year, with the time between campaigns spent on development of cells, polarization optimization, noise, and analysis. Campaigns 1–5 during 2013–2017 took place at the TUM MSR after which we moved to the BMSR-2 for EDM measurement campaigns HeXe2017 and HeXe2018. In this chapter, we briefly review the development work done in Campaigns 1–4. Campaign 5 was dedicated to a systematic effect investigation detailed in Chapter IV. HeXe2017 was our first complete EDM measurement and was undertaken at PTB. The data and analysis of HeXe2017 discussed in Chapters V and VI are the major motivation and focus of this dissertation.

3.1 Experimental Campaign 1 (December 2013)

The collaboration's first attempt at measuring spin precession signals using the Cube-I SQUID system (see Sect. 2.5) took place in December 2013. The six SQUID channels were connected to two FLL electronic boxes, and the voltage output was acquired with a 24-bit USB DAQ (Data Translation DT9826-16). A 1.2 μT B_0 field was generated using a 3-axis set of $\sim$1.5 m wood-frame Helmholtz coils with current applied from an ultra-low

noise current source from I-Test Systems (BE2100) and later a Magnicon current source. A field switch as discussed in Section 2.2.2 was deployed to initiate spin precession. Initial studies were done using a sealed cell ("Maya," see Table 2.3) that was transported from Earl Babcock's polarizer to the TUM MSR using a 1.5 mT transport coil. Sealed SEOP cells from Michigan (X1, X2, and X3 in Table 2.3) containing Rb, N_2, ^{129}Xe and ^{3}He were also tested. Additionally, a valved 6 cm bulb from PTB was used after being filled with a polarized mixture of ^{129}Xe, ^{3}He, and N_2. Early measurements relied on existing SEOP systems from other projects and did observe some small precession signals from ^{3}He and ^{129}Xe that motivated continued effort toward an EDM measurement of ^{129}Xe [89].

3.2 Experimental Campaign 2 (May–June 2014)

During the second experimental campaign, the HeXeEDM apparatus began to come together more concretely. We installed a SEOP polarizer outside the TUM-MSR and began construction of a cell-filling station. For the polarizer, we used a 100 W water-cooled laser diode array [90]. The emission line was narrowed using a reflecting volume Bragg grating to stimulate 794.8 nm diode emission preferentially [91]. After the grating, a quarter-wave plate was used to circularly polarize the light, and two shaping lenses were used to create an approximately 6 cm diameter beam that shone into the windowed calcium silicate oven. An online NMR system developed at PTB [92] was borrowed and used to study the polarization of sealed cells immediately before being transferred into the room. A LabView program was developed for pulsed NMR [93]. AC pulses were generated using a standard function generator (Agilent 33220A). We began developing computer control for the SEOP laser, HV power supplies, and magnetic fields utilizing an existing database developed by Mike Marino for the TUM nEDM experiment. At the time, we were only able to use the internal clock of the USB DAQ for the SQUID channel data. A LabView interface was also used to read the data stream in real time. AC pulses were used to induce spin precession in the Maya ^{3}He cell and double-chambered cell F3. We observed in the

Maya cell that T_2^* increased after each applied pulse. The increasing T_2^* may have been caused by the large longitudinal magnetization of the polarized ^{3}He causing a magnetic field gradient (see Fig. 3.1) within the cell. In the double-chambered cells, we observed frequency beating resulting from the different magnetic fields of the two chambers (see Fig. 3.2).

Next, we focused on OPC and valved EDM cell development. At Michigan, we worked on the development of a circulating gas system with pressure-actuated valves used to create pressure differentials in segments of the system to encourage gas flow between segments. An early form of this system can be seen in Fig. 3.3. We also worked on a portable pulsed-NMR system for easy installation and permanent use at the polarizer outside the TUM MSR.

3.3 Experimental Campaign 3 (May–June 2015)

In the summer of 2015, we installed a four-coil system at the polarizer following the design in Ref. [92] to provide a uniform magnetic field over a larger volume and allow for a larger oven for polarizing OPCs. The stray field from the four-coil system provided enough of a spin-transport field for the cells into the MSR that a transport coil was no longer required. We also installed a new pulsed NMR system developed at Michigan with a LabView interface for permanent use at TUM. The pulsed NMR system was used to study the polarization buildup of ^{3}He and ^{129}Xe in various sealed cells and characterize the completed SEOP polarizer and then determine our best cells for testing inside the MSR. A rail system was constructed using long plastic rods that extended from a station under the SQUID dewar to the polarizer outside the MSR and a 3D-printed cart and holder for the cells. The pulsed NMR system was used to determine polarization losses during transport. Before the addition of a rail system, cells were passed from a person outside the room to a person inside who would remain in the MSR for the duration of the measurement. The person-in-room method was inconvenient because humans tend to introduce magnetic and

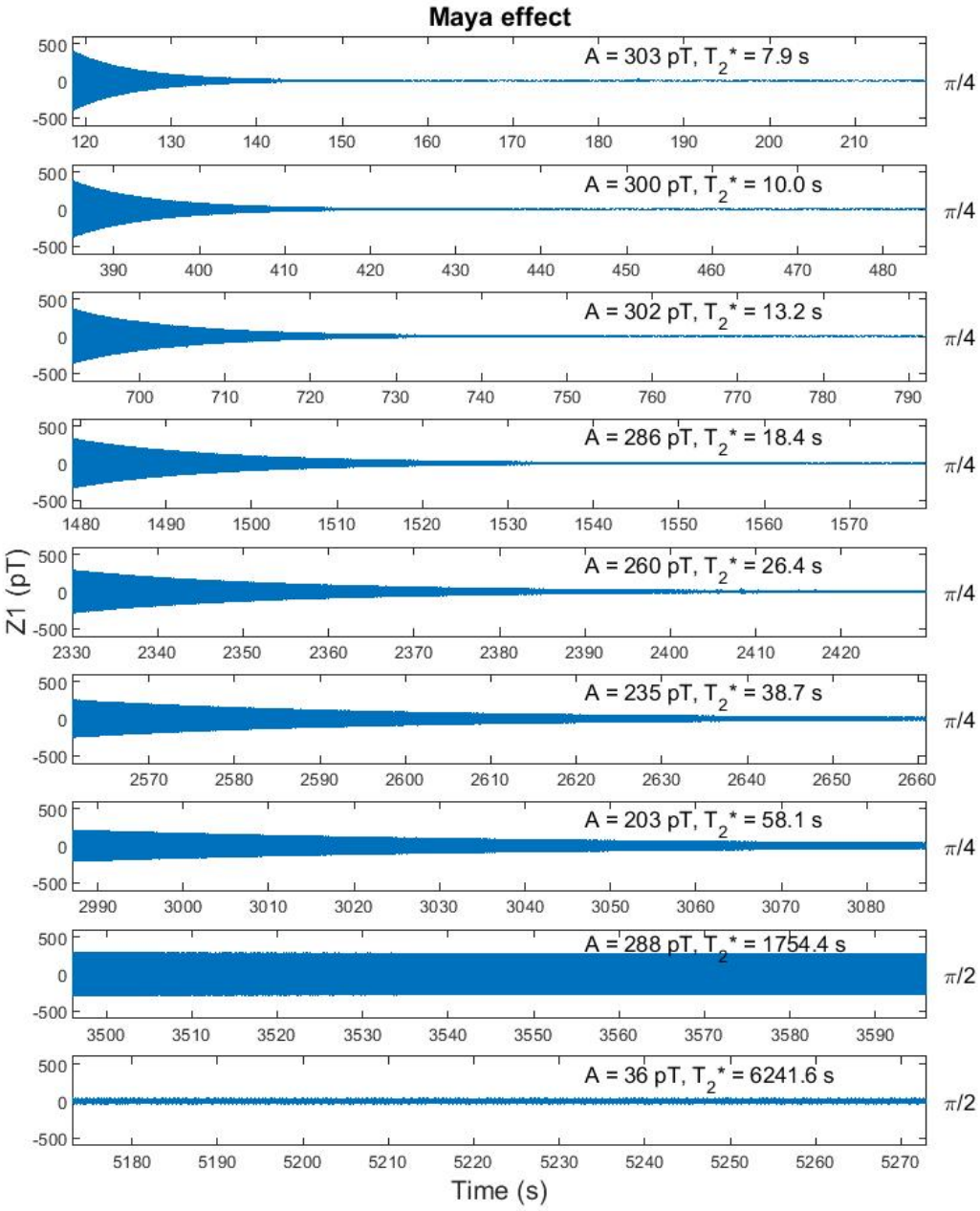

Figure 3.1: Maya effect observed in June 2014. High-pass filtered Z1 data for the first 100 seconds after each nominal $\pi/4$ or $\pi/2$ pulse. T_2^* increased with each pulse as the longitudinal magnetization was destroyed.

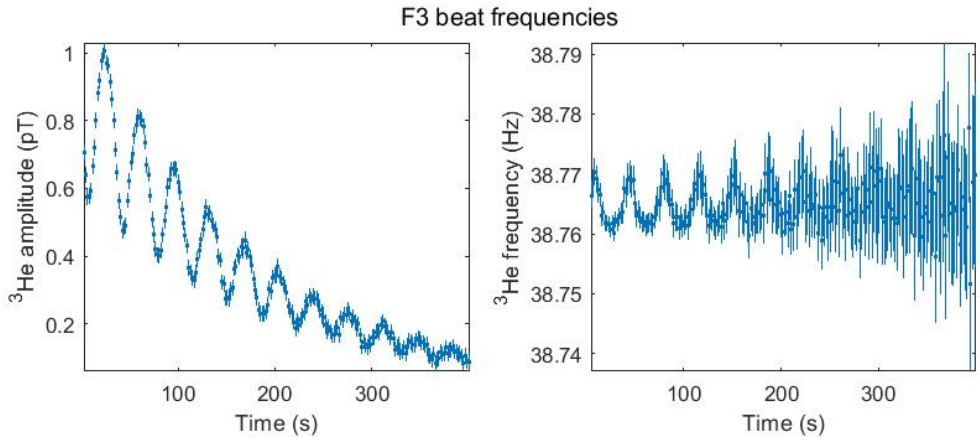

Figure 3.2: Frequency beating of ^{3}He observed in double-chambered cell F3 in June 2014.

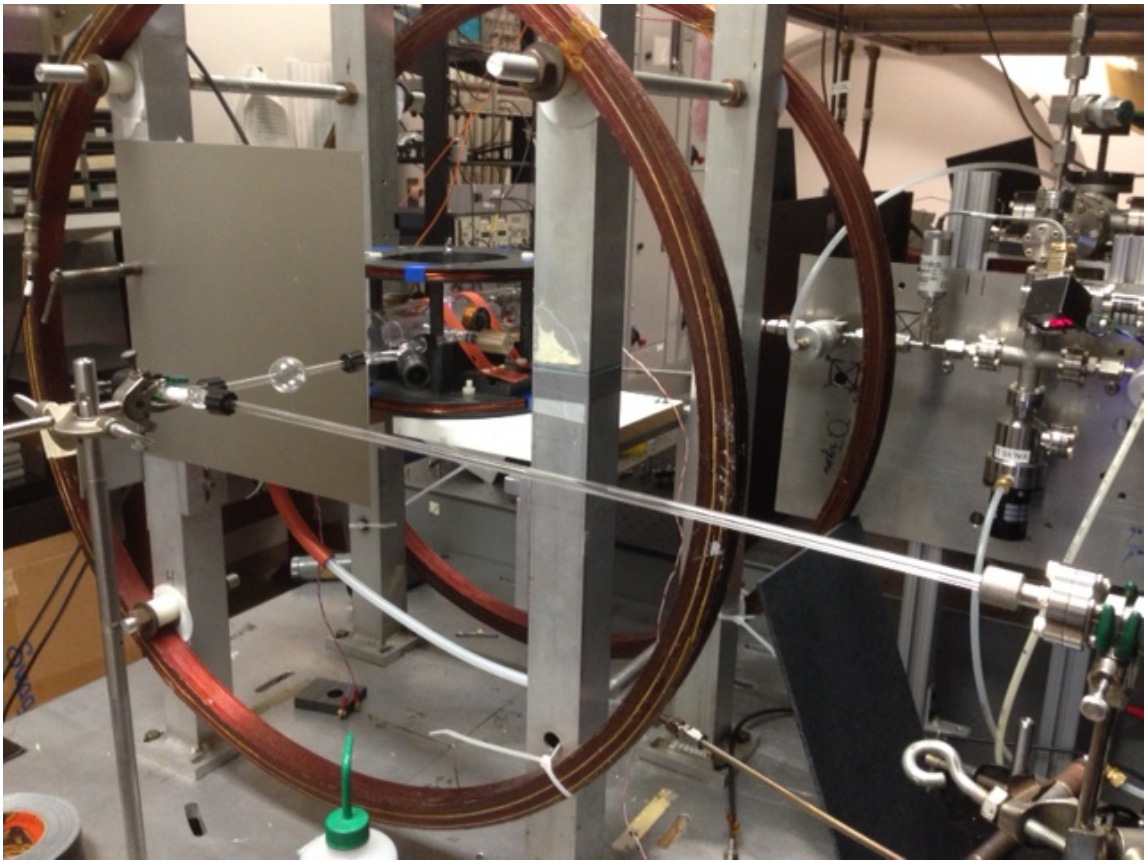

Figure 3.3: Circulating gas system at Michigan. Pressure-actuated valves were controlled by a LabView to activate in a sequence to create gas flow through pressure differentials.

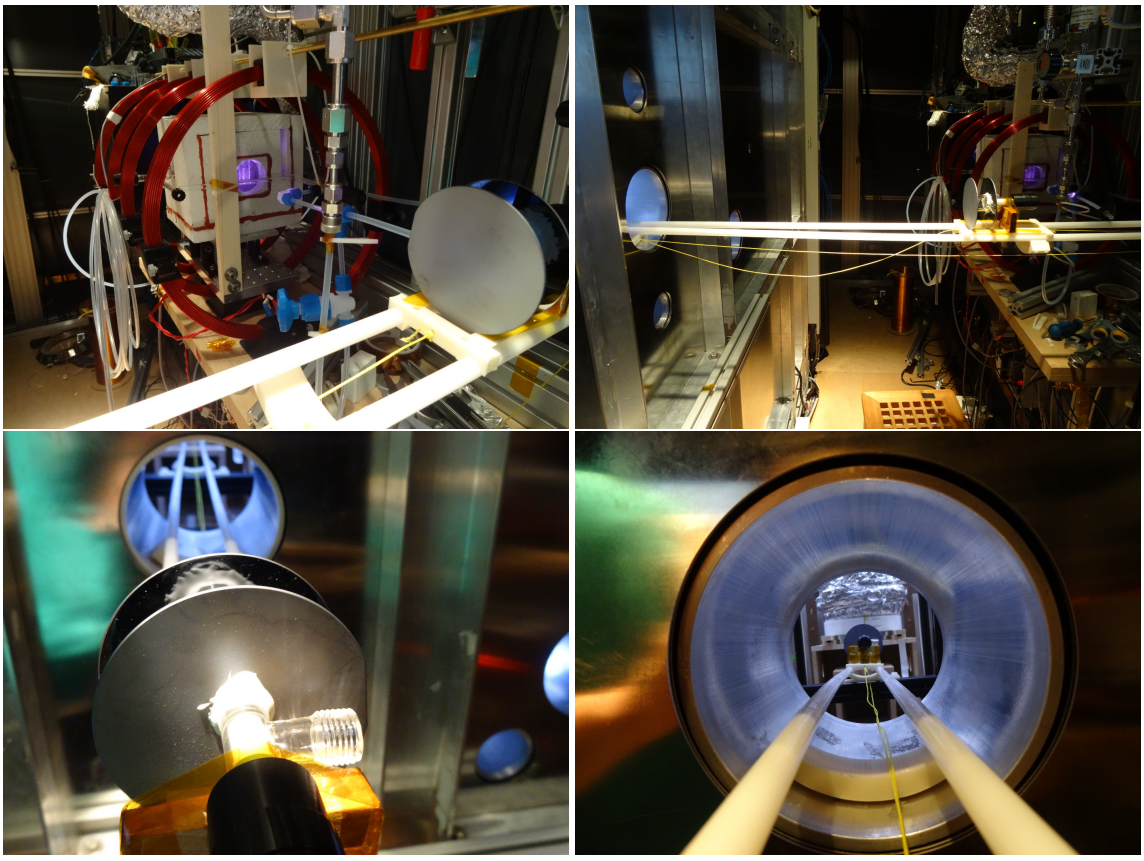

Figure 3.4: Pictures of valved EDM cell filling and transport from June 2015.

vibrational noise.

We obtained our first spin precession measurements using a valved EDM cell (E2) during this campaign. A measurement with high voltage was attempted with 9.4 kV applied across the electrodes, but a breakdown occurred during the measurement. Data was acquired using a 24-bit DAQ (DTacq ACQ437ELF) with the timebase derived from an external SRS 10 MHz Rb frequency standard.

3.4 Experimental Campaign 4 (May–June 2016)

During the Campaign 4, we switched to using the MRX-I SQUID system for a smaller SQUID-cell distance and lower dewar noise. We also replaced the previous wooden coil forms of the 3-axis coil system with a 2-axis coil system with anodized aluminum frames.

The new coils had more rigid mounting to reduce vibrations at low frequency. The design and distances were optimized using COMSOL and featured more accurate mounting and positioning. The goal for this campaign was diagnostic testing and acquisition of spin precession data using the refillable OPCs and valved EDM cells.

HV was applied to one electrode, with the other held at ground potential, to generate the electric field. A grounded silicon wafer was placed between the cell and the SQUIDs to protect them from HV sparks. We set up leakage current monitoring along the return path from the grounded EDM cell electrode to the HV power supply. In test measurements with HV with reasonable ^{129}Xe and ^{3}He amplitudes and T_2^* times we observed large comagnetometer drifts (shown in Fig. 3.5) which became the topic of study for the next experimental campaign discussed in Chapter IV.

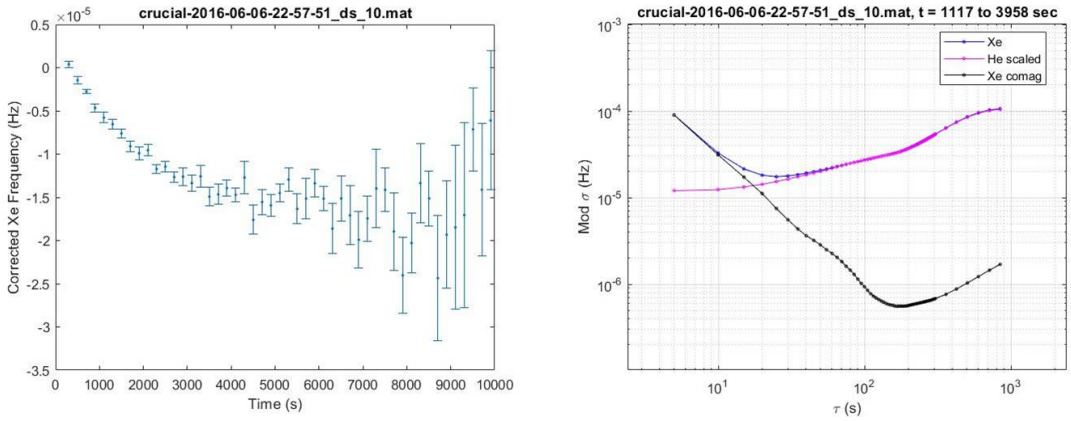

Figure 3.5: Drift in the comagnetometer-corrected ^{129}Xe frequency from data taken during Campaign 4. Left: Corrected ^{129}Xe frequency vs. time. Right: A modified allan deviation plot showing drift dominating over white phase noise after $\sim$150 seconds of integration time.

3.5 HeXe2017 (June–July 2017)

HeXe2017 was the first EDM measurement campaign. The noble gases were polarized in a separate setup similar to that described in Ref. [92]. The gas mixture of 18% Xe ($90 \pm 2\%$ ^{129}Xe), 73% ^{3}He, and 9% N_2 was polarized in a refillable OPC. Typically we

achieved $9-12\%$ polarization for ^{129}Xe and $0.1-0.2\%$ polarization for ^{3}He depending on the total pressure in the OPC. The polarized gas was transferred from the valved OPC to a previously evacuated valved EDM measurement cell and then transported to the magnetically shielded room using a battery-powered $400\ \mu$T shielded solenoid. Before filling, the EDM measurement cell (PP1 or PP2) was degaussed using a magnetic tape eraser. Each time the OPC was filled, the gas was used for two EDM runs with different pressures and polarizations. The first run had higher pressure (~ 1 bar) and lower polarization, and the second run had lower pressure (~ 0.5 bar) and higher polarization. The gas in the OPC was continuously polarized between runs.

Magnetic fields were applied using a 3-axis set of Helmholtz coils with the static magnetic field, $\mathbf{B_0} = B_0\hat{\mathbf{y}}$, of 2.6 μT applied along the y-axis. An AC $\pi/2$ pulse was used to initiate spin precession using the Agilent programmable standard function generator from TUM. After the cell was placed in the measurement position as shown in Fig. 3.6, the door was closed, and the magnetic field was allowed to stabilize for five minutes before the pulse was applied. As the ^{129}Xe and ^{3}He precessed, 6 kV high voltage was applied to one electrode of the measurement cell with the other electrode at ground potential, producing a 2.7 kV/cm field for cell PP2 or 3.3 kV/cm for cell PP1. The voltage was chosen to be safely below the voltage observed to cause a breakdown across the cell at the lowest operating pressure.

Precession frequencies for each species were determined using the data from the Z_1-SQUID, which was located a distance of $50 - -52$ cm from the center of the EDM measurement cell. The SQUID-cell distance was limited by the 3 cm dewar housing and by the grounded safety electrode, a 2 mm thick silicon wafer placed above the cell as shown in Fig. 3.6 to protect the SQUIDs from high voltage discharges. The DAQ used was a commercial system by Lay Audiotechnik [94] and the data acquisition sample rate, nominally 915.5245 Hz, was derived from an Oscilloquartz BVA8607 external clock stable up to 10^{-11} Hz over time scales relevant for the experiment.

Each run, lasting about 15,000 seconds, used a single gas filling. The T_2^* depended on the cell used and the gas pressure. For ^{129}Xe, T_2^* was in the range of $3700 - 8000$ s; for ^{3}He, T_2^* was $4000 - 8000$ s. During each run, the HV polarity was positive, negative, and zero for equal length intervals. The data acquired and analysis are discussed in Chapter V.

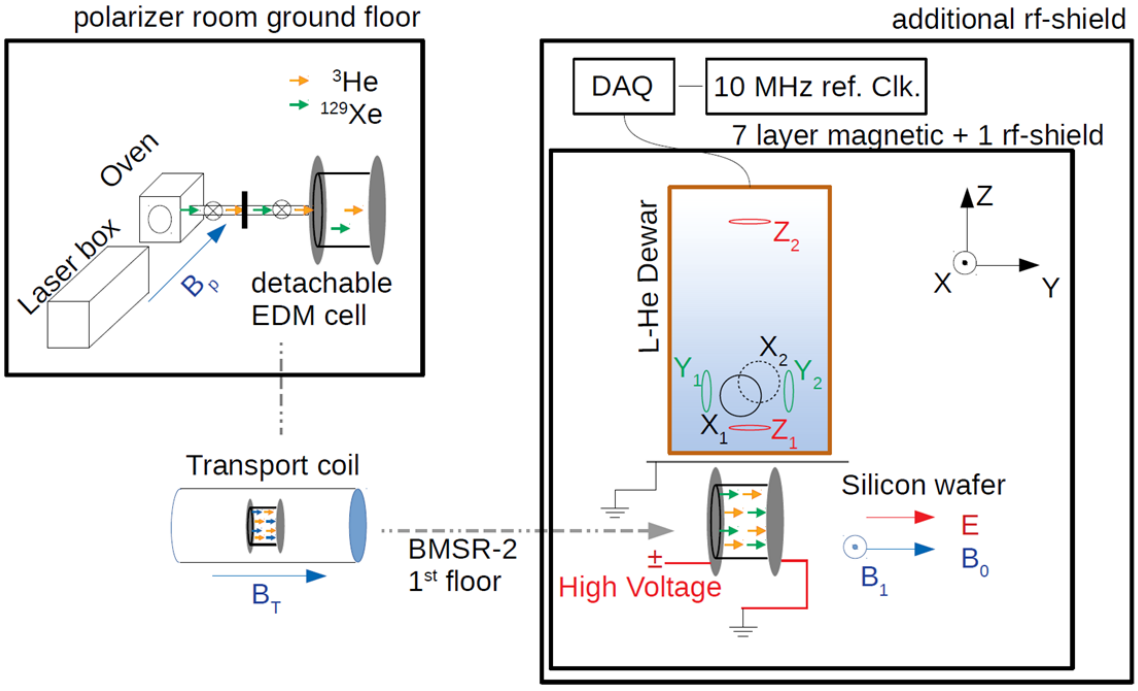

Figure 3.6: The experimental setup at BMSR-2.

Campaign #	**1**	**2**	**3**	**4**	**HeXe2017**	**HeXe2018**
max SNR	800	8000	3000	50000	$\approx 10^5$	$\approx 3\times 10^5$
cell type	sealed	sealed	sealed	valved	valved	valved
noise level [fT/$\sqrt{\text{Hz}}$]	10	10	10	7.5	6	6
max T_2^* [s] (^{129}Xe / ^{3}He)	2000 / 4000	600 / 6000	2700 / 4500	4500 / 9000	8000 / 8000	10000 / 10000
B_0 [μT]	1.2	1.2	1.2	2.6	2.6	2.6
$\pi/2$ method	field switch	AC pulse	AC pulse	AC pulse	AC pulse	field switch

Table 3.1: Summary of HeXeEDM development and measurement campaigns, excluding Campaign 5 which was a separate systematic effect investigation detailed in Chap. IV. The dimensionless signal-to-noise here is SNR $\approx A_{\text{Xe}}^{\text{max}}/(\sigma_{\text{noise level}}/\sqrt{\tau})$ and was determined using maximum ^{129}Xe amplitude and integration time τ =500 s.

CHAPTER IV

Investigations of ^{3}He–^{129}Xe interactions

The drift observed in the comagnetometer frequency (see Fig. 3.5) is the dominant source of systematic error for HeXeEDM and other precision searches using a ^{129}Xe–^{3}He comagnetometer [33, 34] and has been observed since the very first investigations into use of a ^{129}Xe–^{3}He comagnetometer in ^{129}Xe EDM measurements [27]. The drift is caused by previously uncharacterized magnetic interactions between the ^{129}Xe and ^{3}He spins and the bulk magnetization of each polarized species. We've seen some indication of the strength of the internal magnetic fields and gradients in the case of the "Maya effect" (Fig. 3.1) where the T_2^* of ^{3}He was reduced because of the gradient caused by the large ^{3}He longitudinal polarization. In this chapter we review the underlying physics behind the comagnetometer drift and propose a model to explain it, supported by experimental studies performed at the TUM MSR. A preprint summarizing this work is now available [95] and was the subject of Jonas Meinel's master's thesis [96].

4.1 Internal magnetic fields

The origin of the drift has previously been attributed to Ramsey-Bloch-Seigert shifts [34] which has generated some controversy [97, 98]. The Ramsey-Bloch-Seigert (RBS) shift [99, 100] is the generalized Bloch-Seigert shift (Eq. 2.25) in this case due to the rotating internal magnetic fields caused by the precessing atoms. For a system with gy-

romagnetic ratio γ and Larmor frequency $\omega_0 = \gamma B_0$, the RBS shift for a rotating field of amplitude B_1 and frequency ω_1 is

$$\delta\omega_{RBS}(t) = \pm\left[\sqrt{\Delta\omega^2 + \gamma^2 B_1^2(t)} - \Delta\omega\right], \tag{4.1}$$

where $\Delta\omega = |\omega_0 - \omega_1|$. With this model, there are two effects to be considered: one is the "cross-talk" or the shift of the ^{129}Xe precession frequency due to the internal field of ^{3}He and vice versa; the second is the "self-shift" or the shift in the ^{129}Xe due to its own internal field and similarly for ^{3}He. In these cases, B_1 refers to the internal magnetic field B_{int} from ^{129}Xe or ^{3}He. The controversy mentioned above was about the size of such a field. In Ref. [34], the authors propose that the magnetic field created by the transverse magnetization is the classical result for the magnetic field in a uniformly magnetized sphere

$$\mathbf{B}_{\text{int}} = \frac{2\mu_0}{3}\mathbf{M}. \tag{4.2}$$

However, as mentioned in the comment by Romalis *et al*. [97], the above result comes from the classical expression for the field created by a magnetic dipole $\mathbf{m}$

$$\mathbf{B}(\mathbf{r}) = \frac{\mu_0}{2\pi}\frac{2\hat{\mathbf{r}}(\hat{\mathbf{r}}\cdot\mathbf{m}) - \mathbf{m}}{r^3} + \frac{2\mu_0\mathbf{m}}{3}\delta(\mathbf{r}), \tag{4.3}$$

for a uniform density of dipoles $n = M/m$. By integrating over a spherical cell, the first term integrates to zero for a perfect sphere. For real atoms of finite size that are randomly distributed within a spherical volume and are completely noninteracting, the average field value is zero [101, 102]. However, in the case of contact interactions the second term is parametrized by a factor κ

$$\mathbf{B} = \frac{2\mu_0}{3}\kappa\mathbf{M} \tag{4.4}$$

where $\kappa \equiv n(0)/n(\infty)$ and $n(\mathbf{r})$ is the number density of dipoles within a sphere of radius r. Additionally, the first term in Eq. 4.3 contributes a geometric factor to $\kappa_{\text{eff}} \equiv \kappa_{\text{geo}} + \kappa$.

In the studies presented below we expect κ_{geo} to be the dominant contribution to B_{int}. We observed the effect of B_{int} by separately considering the influence of the transverse magnetization M_T and the longitudinal magnetization M_L on the species' frequencies. We performed a study to test the RBS model by observing frequency shifts in ^{3}He after changing the size of the transverse magnetization M_T. We also observed frequency shifts in ^{3}He and ^{129}Xe after changing the direction of the longitudinal magnetization M_L of each species by 180°.

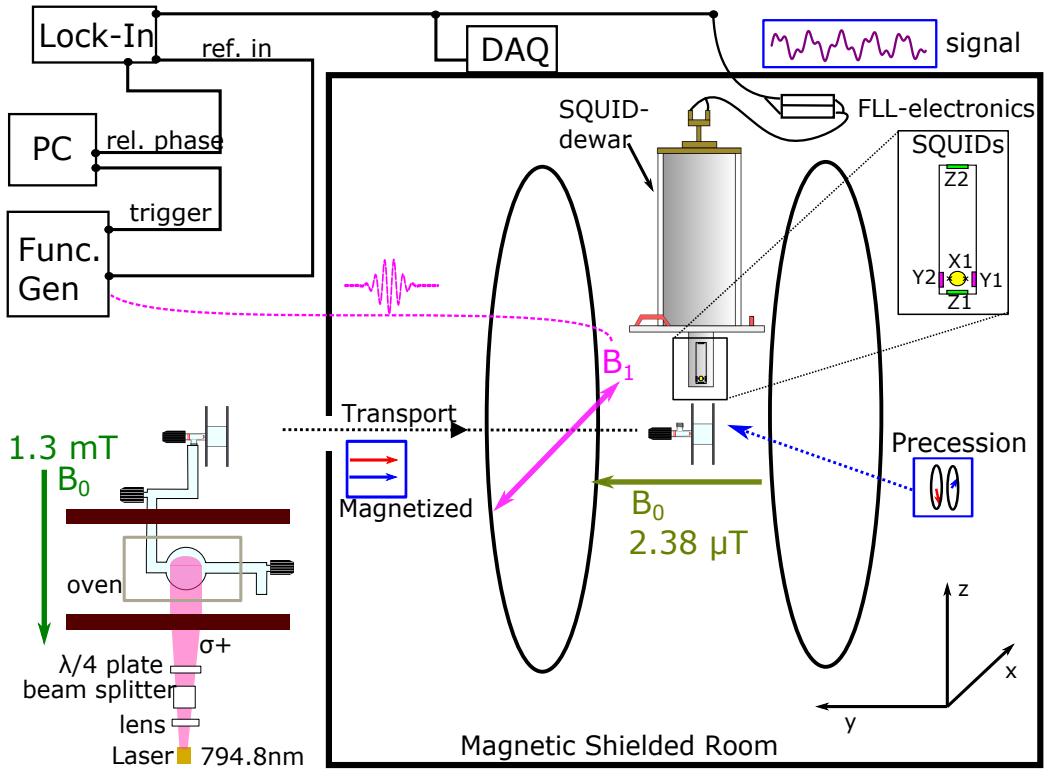

Figure 4.1: Diagram of the apparatus used for investigation of ^{3}He–^{129}Xe interactions [95]. Phase-coherent pulsing was implemented using a lock-in amplifier.

4.2 Experimental setup

The setup used was the same as in Campaign 4 (Section 3.4) at the TUM MSR. Fig. 4.1 shows a diagram of the apparatus.Two cells were used for these experiments: a sealed cell (cell 1 in Table 2.3) and a valved EDM cell (E2). The main difference from Campaign 4 was

the implementation of phase-coherent or in-phase pulsing for the single-species (sealed ^{3}He cell) measurements, which allowed us to apply pulses to already precessing signals. For the phase-coherent pulsing, the Z1-SQUID signal was split from the DAQ to a lock-in amplifier to track the phase difference between the precession frequency and the reference signal used for the pulses. Once a pulse was manually triggered from the operating PC, the AC pulse signal was sent to the B_1 coils at a time when the phase difference $|\phi_{Z1} - \phi_{\text{ref}}| = 0$ according to the lock-in amplifier.

4.3 Analysis method

The general analysis method we use for spin precession data is described in more detail in the next chapter. Briefly, the data were divided into sections called blocks and a time-domain fit to the following function was used for single species data to determine the phase for each block $\phi_i = \arctan(B_i/A_i)$

$$S(t) \quad = \quad A\sin\omega t + B\cos\omega_t + c_1 t + c_0, \tag{4.5}$$

From the block phases, the accumulated phase was determined by adding the appropriate number of cycles $\Phi = \phi + 2\pi N$ where N is the number of cycles. To determine single species frequencies, because of magnetic field drift, a Y-SQUID-comagnetometer was employed. For the SQUID comagnetometer, the data for Y1 and Y2 were averaged first to remove any residual spin precession signal picked up by the SQUIDs and then the SQUID data for each block was averaged to get the relative magnetic field $\tilde{B}_i$ measured by the SQUID for each block. We then defined a SQUID comagnetometer for each species by numerically integrating $\tilde{B}$: $\tilde{\Phi}(t_i) = \Phi(t_i) - \gamma\mathcal{G}\int_0^{t_i}\tilde{B}(t)dt$, where $\mathcal{G}$ is a scaling factor that depends on the SQUID calibration. The single-species frequencies were determined from

a linear fit of $\tilde{\Phi}(t_i)$ vs. t_i. For two-species data we used the following fit function

$$\begin{aligned} S(t) &= A_{\mathrm{Xe}} \sin \omega_{\mathrm{Xe}} t + B_{\mathrm{Xe}} \cos \omega_{\mathrm{Xe}} t + \\ & \quad A_{\mathrm{He}} \sin \omega_{\mathrm{He}} t + B_{\mathrm{He}} \cos \omega_{\mathrm{He}} t + c_1 t + c_0. \end{aligned} \tag{4.6}$$

and the ^{3}He–^{129}Xe comagnetometer frequency was determined from a linear fit of $\Phi_{\mathrm{co}} = \Phi_{\mathrm{Xe}} - R\Phi_{\mathrm{He}}$, where R is the nominal ratio of the gyromagnetic ratios $\gamma_{\mathrm{Xe}}/\gamma_{\mathrm{He}}$.

4.4 Tests by varying transverse magnetization

For the single-species experiment we used a sealed SEOP cell. To vary M_T we applied a sequence of phase-coherent 90° pulses to move the magnetization direction between four angles with respect to $\hat{\mathbf{B}}_\mathbf{0}$, illustrated in Fig. 4.2: (1) 10° (2) 100° (3) 190°, and (4) 280°. If $\theta_1 \equiv 10°$, the states with low $M_T = M\cos\theta_1$ and opposite large $M_L = M\sin\theta_1$ are (1) and (3) and the states with high $M_T = M\sin\theta_1$ and opposite small $M_L = M\cos\theta_1$ are (2) and (4). Averaging pairs with opposite $\hat{\mathbf{M}}_\mathbf{L}$ cancels potential contributions proportional to M_L. Pulses were applied 30 seconds apart in a pattern of $+10°$, $+90°$, $+90°$, $+90°$, $-90°$, $-90°$, $-90°$, $+90°$, etc. to reduce accumulation of pulse error. Therefore, the sequence of states was (1), (2), (3), (4), (3), (2), (1), (2), (3), (4), etc.

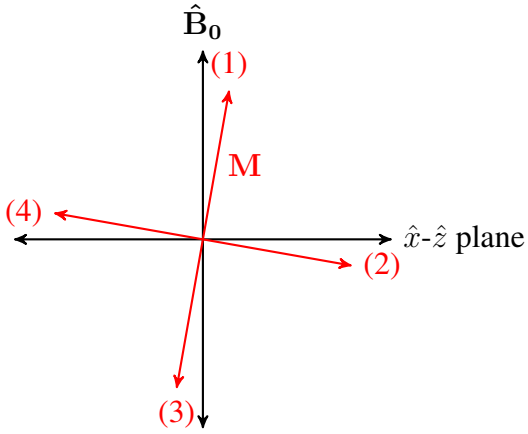

Figure 4.2: Transverse magnetization test pulsing scheme.

The observed frequency shift $\delta\omega_T$ was determined using

$$\delta\omega_T = \left| \left(\frac{\omega_1 + \omega_3}{2} \right) - \left(\frac{\omega_2 + \omega_4}{2} \right) \right|. \tag{4.7}$$

The data are shown in Fig. 4.3 and the weighted average was

$$\frac{1}{2\pi}\delta\omega_T = 0.01 \pm 0.02 \ \mu\text{Hz} \tag{4.8}$$

which is consistent with no observed frequency shift. This result suggests that RBS shifts are not the dominant source of the observed comagnetometer drifts of several μHz.

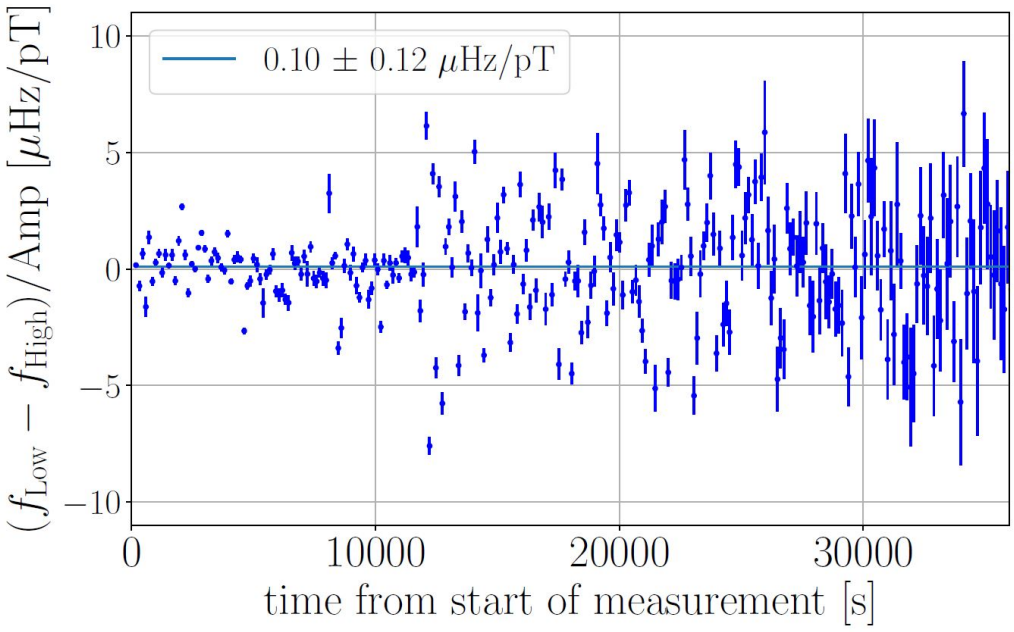

Figure 4.3: $\delta\omega_T/(2\pi)$ vs. time for the transverse shift test [95]. 960 frequencies were used to derive 320 values of $\delta\omega_T/(2\pi)$. The result is consistent with no observed shift.

4.5 Tests by varying longitudinal magnetization

For tests of frequency shifts caused by M_L we first applied an initial pulse with tip-angle θ_{in} followed by a train of 180° pulses, which reverse the direction of M_L. The frequency

shift $\delta\omega_L$ was determined from the difference between $\pm\hat{\mathbf{M}}_\mathbf{L}$

$$\delta\omega_L = \omega(\theta_{\text{in}}) - \omega(\theta_{\text{in}} + 180^\circ) \tag{4.9}$$

4.5.1 Single species

Since we expect the frequency shift to be dependent on B_{int}, which is dominated by the integration of the first term of Eq. 4.3 over the cell, we used the sealed cell to test the geometric dependence of the frequency shift. The sealed cells are spherical with pull-off stems as illustrated in Fig. 4.4 and shown in Fig. 2.10a. We can approximate them as perfect spheres with a small external volume containing a dipole field generated by the polarized ^{3}He gas within. We measured the frequency shifts while rotating the cell stem by an angle α in the $\hat{x}$-$\hat{y}$ plane, essentially moving the location of the external dipole presumed to be dominated by the pull-off stem. The results are shown in Fig. 4.4.

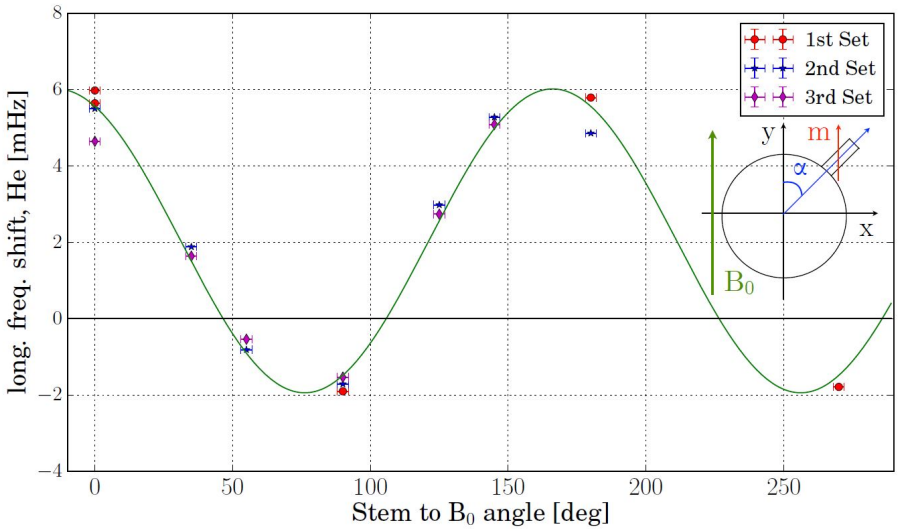

Figure 4.4: $\delta\omega_L/(2\pi)$ vs. α [95]. The data shown is from a single measurement where the angle α was rotated back-and-forth three times. The data was fitted to a modified P_2 polynomial, $a(3\cos^2(\alpha-b)-1)+c$, where $a = -2.74\pm0.06$ mHz, $b = -14\pm0.6^\circ$, and $c = 0.76\pm0.07$ mHz, which is consistent with the angular dependence of the field in the cell produced by an external dipole. The offset may be caused by asphericity of the cell that is α-symmetric.

4.5.2 Two species

For two species measurements, we used the cylindrical valved EDM cell. An initial $45°$ pulse was applied that was resonant with both species, followed by $180°$ single-species resonant pulses, which reversed the magnetization of ^{129}Xe and ^{3}He sequentially. In Fig. 4.5, the ^{3}He frequency shifts are compared with the comagnetometer-corrected ^{3}He frequency $\omega_{\mathrm{co,He}} = \omega_{\mathrm{He}} - \frac{\gamma_{\mathrm{He}}}{\gamma_{\mathrm{Xe}}}\omega_{\mathrm{Xe}}$. The data shows that the comagnetometer does not cancel the observed longitudinal frequency shifts.

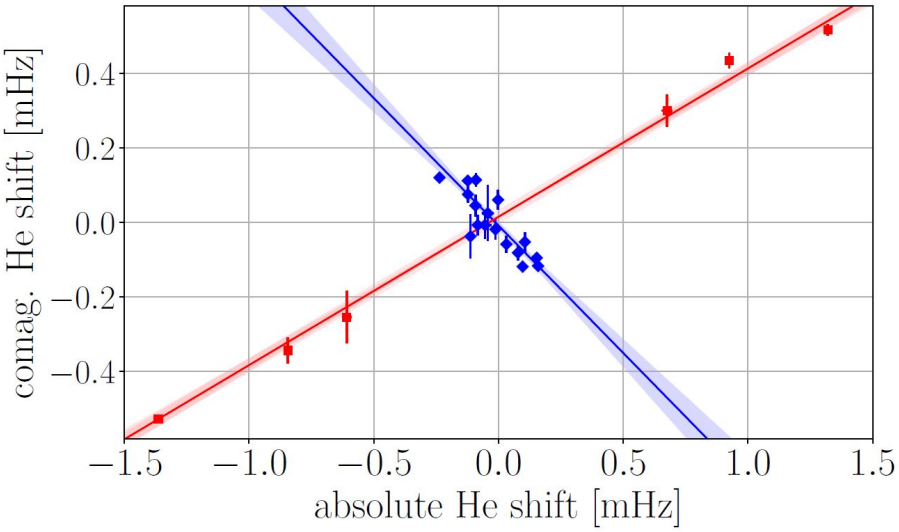

Figure 4.5: $\delta\omega_{\mathrm{co,He}}/(2\pi)$ vs. $\delta\omega_{\mathrm{He}}/(2\pi)$ after a ^{129}Xe $180°$ pulse (blue diamonds) and after a ^{3}He $180°$ pulse (red squares) [95].

4.6 Interpretation of results

The data show there is no observed transverse frequency shift; however, there is significant shift observed in both ^{129}Xe and ^{3}He when M_L is reversed. We refer to the observed shift as the species-dependent shift and as we show below this can arise when the precessing magnetization M_T of one species exerts a torque on M_L of the same-species (a self-shift), rotating the magnetization into the transverse plane that is out of phase with M_T, therefore advancing the phase resulting in a frequency shift.

To interpret our data we parametrize the frequency shifts due to transverse and longitudinal magnetization as

$$\delta\omega_k^{T,m} = \rho_k^m M_m^T \qquad \delta\omega_k^{L,m} = \lambda_k^m M_m^L, \tag{4.10}$$

where indices k, m refer to the species ^{129}Xe or ^{3}He. The time-dependent comagnetometer drifts are

$$\delta\omega_{\text{co},k}^T = \rho_{\text{co}}^k M_k^T(0) e^{-t/T_2^{*k}} - r\rho_{\text{co}}^m M_m^T(0) e^{-t/T_2^{*k}} \tag{4.11}$$

$$\delta\omega_{\text{co},k}^L = \lambda_{\text{co}}^k M_k^L(0) e^{-t/T_1^k} - r\lambda_{\text{co}}^m M_m^L(0) e^{-t/T_1^k}, \tag{4.12}$$

where $r_k^m = \gamma_k/\gamma_m$ and $\rho_{\text{co}}^k = \rho_k^k - r\rho_m^k$ and $\lambda_{\text{co}}^k = \lambda_k^k - r\lambda_m^k$. The internal magnetic field is $\mathbf{B}_{\text{int}}^m = \frac{2\mu_0}{3}\kappa_{\text{eff},k}^m \mathbf{M}^k$. We parametrize the geometric component as

$$B_{\text{int}}^T = \mu_0 \Gamma^T M^T \qquad B_{\text{int}}^L = \mu_0 \Gamma^L M^L \tag{4.13}$$

where Γ^T, Γ^L are dimensionless cell-specific geometric factors.

The effect of B_{int} on the precession frequency can be determined using the Bloch equations. If $\mathbf{B_0} = B_0\hat{\mathbf{z}}$,

$$\begin{aligned}
\frac{\mathrm{d}M_k^x}{\mathrm{d}t} &= \gamma_k \left\{ M_k^y \left[B_{\text{int}}^z(k) + B_{\text{int}}^z(m) \right] - M_k^z \left[B_{\text{int}}^y(k) + B_{\text{int}}^y(m) \right] \right\} \\
\frac{\mathrm{d}M_k^y}{\mathrm{d}t} &= -\gamma_k \left\{ M_k^x \left[B_{\text{int}}^z(k) + B_{\text{int}}^z(m) \right] - M_k^z \left[B_{\text{int}}^x(k) + B_{\text{int}}^x(m) \right] \right\} \\
\frac{\mathrm{d}M_k^z}{\mathrm{d}t} &= \gamma_k \left\{ M_k^x \left[B_{\text{int}}^y(k) + B_{\text{int}}^y(m) \right] - M_k^y \left[B_{\text{int}}^x(k) + B_{\text{int}}^x(m) \right] \right\}.
\end{aligned} \tag{4.14}$$

In a frame rotating at the Larmor precession frequency $\omega_{0,k} = \gamma_k B_0$ around $\hat{\mathbf{z}}$, all the static

B_z components vanish and the self-resonant contribution is

$$\begin{aligned}
\frac{\mathrm{d}M_k^{x'}}{\mathrm{d}t} &= -\gamma_k M_k^{z'} B_{\text{int}}^{y'}(k) \\
\frac{\mathrm{d}M_k^{y'}}{\mathrm{d}t} &= \gamma_k M_k^{z'} B_{\text{int}}^{x'}(k) \\
\frac{\mathrm{d}M_k^{z'}}{\mathrm{d}t} &= \gamma_k M_k^{x'} B_{\text{int}}^{y'}(k) - M_k^{y'} B_{\text{int}}^{x'}(k).
\end{aligned} \tag{4.15}$$

Substituting $B_{\text{int}}^{x',y'} = \mu_0 \Gamma^T M^{x',y'}$,

$$\begin{aligned}
\frac{\mathrm{d}M_k^{x'}}{\mathrm{d}t} &= -\mu_0 \gamma_k M_k^{z'} \Gamma^T M_k^{y'} \\
\frac{\mathrm{d}M_k^{y'}}{\mathrm{d}t} &= \mu_0 \gamma_k M_k^{z'} \Gamma^T M_k^{x'} \\
\frac{\mathrm{d}M_k^{z'}}{\mathrm{d}t} &= 0,
\end{aligned} \tag{4.16}$$

we see that in the rotating frame $\mathbf{M}'$ precesses with frequency $\delta\omega_k = -\gamma_k \mu_0 \Gamma^T M_k^{z'}$ or $\delta\omega_k = -\gamma_k \mu_0 \Gamma^T M_k^L$. We interpret this as a frequency shift due to the torque on M_k^z from the resonant rotating component of $\mathbf{B}_{\text{int}}$. There are two frequency shifts, one is from B_{int}^L adding to B_0. The other is $\delta\omega_k$. Combining them,

$$\omega_k = \omega_{0,k} + \mu_0 \gamma_k \left[(\Gamma^L - \Gamma^T) M_k^L + \Gamma^L M_m^L \right]. \tag{4.17}$$

For the comagnetometer frequency, $\omega_{\text{co}} = \omega_k - \frac{\gamma_k}{\gamma_m}\omega_m$, we find

$$\omega_{\text{co}} = -\mu_0 \gamma_k \Gamma^T \left(M_k^L - M_m^L \right), \tag{4.18}$$

which is a frequency shift proportional to the difference of longitudinal magnetizations that decays as $M_{\text{Xe}}^L e^{-t/T_1^{\text{Xe}}} - M_{\text{He}}^L e^{-t/T_1^{\text{He}}}$, which is consistent with our observations. To mitigate the drift, we can investigate geometries that reduce Γ^T as well as reduce residual M_k^L through more accurate 90° pulses.

CHAPTER V

Analysis

This chapter describes the analysis method used for spin precession data. For HeXe2017, the EDM data for the experiment were collected in 16 separate runs defined as a spin precession measurement with applied high-voltage that begins with a $\pi/2$ pulse. To extract frequencies for ^{129}Xe and ^{3}He used in the analysis, the data for each run were divided into blocks and segments. Blocks are the shortest data selections, typically 5 to 20 seconds and used to determine the phases of ^{129}Xe and ^{3}He at a specific time within each block. The length of the block is chosen to be short enough that B_0 drift did not affect that validity of the fit function but long enough to separate the two frequencies. Segments are the set of consecutive blocks at an applied high-voltage. They are typically 400 or 800 seconds long. A linear fit of the comagnetometer-corrected xenon phase per segment provides the comagnetometer frequency of each HV state, from which the EDM frequency is derived.

The analysis of data for a block of length τ was done by a time-domain fit of the data to determine the ^{129}Xe and ^{3}He phase for each block. For unfiltered data, there was typically some SQUID baseline drift, so the fitting function was

$$\begin{aligned} S_{\text{8par}}(t) &= A_{\text{Xe}} \sin \omega_{\text{Xe}} t + B_{\text{Xe}} \cos \omega_{\text{Xe}} t + \\ & \quad A_{\text{He}} \sin \omega_{\text{He}} t + B_{\text{He}} \cos \omega_{\text{He}} t + c_1 t + c_0, \end{aligned} \tag{5.1}$$

where the last two terms describe offset and baseline drift. In order for this model to

describe the data effectively, the blocks must be short enough that the drift is purely linear. An F-test [103] was used to determine the significance of adding the baseline drift terms in Eq. 5.1. Alternatively, baseline drift can be removed using a finite impulse response (FIR) high-pass filter. An FIR filter has the advantage of having an exactly linear phase response, and the resulting group delay can be easy corrected. The specific filter used was an equiripple linear-phase FIR filter designed using Matlab's Signal Processing Toolbox with a passband frequency of 5 Hz and a stopband frequency of 0.5 Hz. For filtered data, SQUID offset and drift may be neglected and the fit model is

$$\begin{aligned} S_{\text{6par}}(t) \quad &= A_{\text{Xe}} \sin \omega_{\text{Xe}} t + B_{\text{Xe}} \cos \omega_{\text{Xe}} t + \\ &\quad A_{\text{He}} \sin \omega_{\text{He}} t + B_{\text{He}} \cos \omega_{\text{He}} t. \end{aligned} \tag{5.2}$$

The fits were performed using the separable non-linear least squares method described in [104] using Levenberg-Marquardt least-squares minimization over a fixed time interval $[-\tau/2, \tau/2]$. The phase for each species at the center for each block, labeled by index m, was $\phi^m_{\text{Xe/He}} = \arctan\left(B^m_{\text{Xe/He}}/A^m_{\text{Xe/He}}\right)$. The two-argument four-quadrant inverse tangent function (`atan2` in Matlab) was used to return a phase in the domain $[-\pi, \pi]$. The unwrapped phase is $\Phi^m_{\text{Xe/He}} = \phi^m_{\text{Xe/He}} + 2\pi N_m$, where N_m is the integer number of cycles. The phase at each time $t_m = m\tau$ was determined using

$$\begin{aligned} \Phi^m_{\text{Xe/He}} \quad &= \phi^m_{\text{Xe/He}} + \left\{ \Phi^{m-1}_{\text{Xe/He}} + \omega^{m-1}_{\text{Xe/He}} \tau \right. \\ &\quad \left. - \left(\Phi^{m-1}_{\text{Xe/He}} + \omega^{m-1}_{\text{Xe/He}} \tau \right) \bmod (2\pi) \right\}, \end{aligned} \tag{5.3}$$

where the term in brackets is $2\pi N_m$. The uncertainty of $\Phi^m_{\text{Xe/He}}$ is estimated from standard gaussian error propagation using the parameter uncertainties of $A^m_{\text{Xe/He}}$ and $B^m_{\text{Xe/He}}$, obtained from computation of the covariance matrix of the fit to Eq. 5.2, which was scaled by the mean-squared-error of the residuals from the fit. Frequencies were determined by a linear least-squares fit of the phase vs. time. To get the comagnetometer frequency, the

correction was applied to the ^{129}Xe phase using $\Phi_{\mathrm{Xe,co}} = \Phi_{\mathrm{Xe}} - R\Phi_{\mathrm{He}}$, where $R = 1/r$ and $r \equiv 2.7540816 \approx \gamma_{\mathrm{He}}/\gamma_{\mathrm{Xe}}$, is the number used in the analysis which is the nominal ratio of the shielded ^{3}He and ^{129}Xe gyromagnetic ratios [105].

For the main analysis, the 20 second block length τ was chosen so that amplitude decay and frequency drift were small enough not to affect the validity of the fit model but long enough to separate the ^{129}Xe and ^{3}He frequencies. Longer block lengths were preferable because they decreased computational time. The comagnetometer correction was applied to each block so that B_0 drifts over periods longer than τ were compensated. Fig. 5.1 illustrates the limitation of B_0 drift on block length.

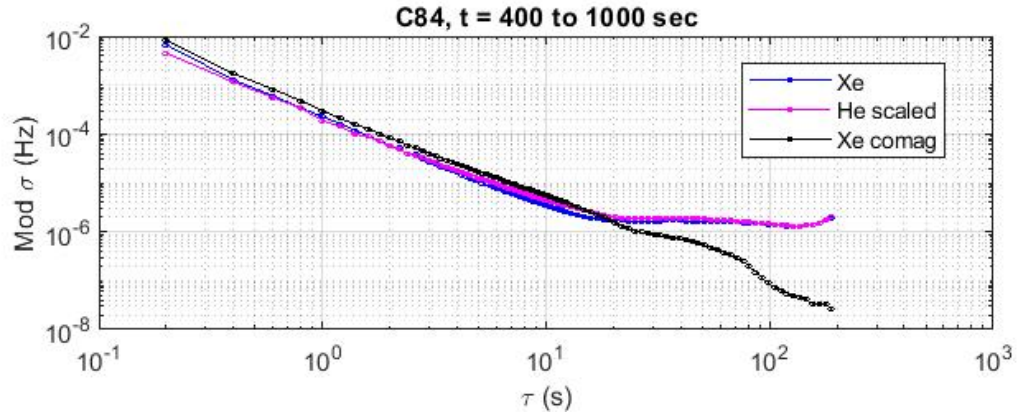

Figure 5.1: Modified Allan deviation of run C84 from June 2017. B_0 drift is observed beyond 20 seconds, our typical analysis block length.

Similarly, comagnetometer drift limits the integration time for a measurement of the comagnetometer frequency, ω'. For the analysis, this means the length of time for which the comagnetometer phase $\Phi_{\mathrm{Xe,co}}$ is linear. An estimate of the size of the comagnetometer drift was determined from Modified Allan deviation plots of early spin precession runs and was used to determine how often we switched the applied HV polarity. [1]

A HV **segment** is the portion of data at a given HV polarity. We chose this length to be 400 or 800 seconds and for each run all segments had equal length. To account for drift

[1]The Modified Allan deviation in contrast to the regular Allan deviation can separate white phase noise (slope $\tau^{-3/2}$) from white frequency noise (slope $\tau^{-1/2}$). From Ref. [106], the Modified Allan variance from a set of M frequency measurements y for averaging time $\tau = m\tau_0$ where τ_0 is the basic measurement interval

when we combined segments to determine the EDM frequency ω_d, we used the following HV polarity pattern for all runs: $\pm[0+--+-++--++-+--+0, 0-++-+--++--+-++-0]$. Two runs, C82 and C13, were ended after the first 18 states. The HV polarity pattern allowed us to combine the frequencies from each HV segment i to determine ω_d in a way that compensated for comagnetometer drift. For example, if the comagnetometer drift is purely linear over four HV segments,

$$\omega' = a^0 + a^1 t + \omega_d, \tag{5.6}$$

then, for a sequence of $+--+$ and equal length segments $t_i = i\Delta t$,

$$\begin{aligned}
\omega'_1 - \omega'_2 - \omega'_3 + \omega'_4 &= a^0 + a^1 t_1 + \omega_d - (a^0 + a^1 t_2 - \omega_d) \\
&\quad - (a^0 + a^1 t_3 - \omega_d) + a^0 + a^1 t_4 + \omega_d \\
&= a^1 t_1 - a^1 t_2 - a^1 t_3 + a^1 t_4 + 4\omega_d \\
&= a^1(\Delta t - 2\Delta t - 3\Delta t + 4\Delta t) + 4\omega_d \\
&= 4\omega_d.
\end{aligned} \tag{5.7}$$

Similarly, a sequence of eight cancels quadratic drifts; a sequence of 16 cancels drifts up to 3rd order; and the full sequence is insensitive to drifts up to 4th order. Because this is an unweighted average, longer sequences resulted in lower statistical sensitivity due to loss of signal amplitude by the end of the run from T_2^* decay. Because our drifts were mostly linear over four segments, we chose to use a sequence of four for our analysis. The

---

is

$$\mathrm{Mod}\sigma_y^2(t) = \frac{1}{2m^4(M-3m+1)} \sum_{j=1}^{M-3m+2} \left\{ \sum_{i=j}^{j+m-1} \left(\sum_{k=i}^{i+m-1} [y_{k+m} - y_k] \right) \right\}^2, \tag{5.4}$$

or with phase data x from $N = M + 1$ measurements

$$\mathrm{Mod}\sigma_y^2(t) = \frac{1}{2m^2\tau^2(N-3m+1)} \sum_{j=1}^{N-3m+1} \left\{ \sum_{i=j}^{j+m-1} [x_{i+2m} - 2x_{i+m} + x_i] \right\}^2. \tag{5.5}$$

process for determining the systematic error from higher order drifts is discussed in Ch. VI. A sequence of segments used for a ω_d determination we refer to as an **EDM set**.

There were two irregular runs. In C82, there was a significant SQUID perturbation in the second HV segment. In C93, the HV did not switch on until the last 100 seconds of the first intended HV segment. For both these runs the affected HV segment was shortened to only include the unaffected data. The other three segments in the EDM set were also shortened by the same amount so that the linear comagnetometer drift could be compensated. For another run, C13, an F-test showed that the $\Phi^m_{\mathrm{Xe,co}}$ vs. $m\tau$ was not linear for the first 5 segments, so they were shortened by six blocks or 120 seconds until the F-test showed a $P \leq 0.5$ that a quadratic term was significant[2].

For each HV segment, the extracted comagnetometer frequencies ω_i' were blinded by adding or subtracting, depending on $\hat{\mathbf{E}}\cdot\hat{\mathbf{B}}$, a previously computer-generated pseudorandom number of magnitude $\leq 5\times10^{-8}$ Hz. The blinding offset was saved separately from the data in a binary format. After all cuts and systematic corrections were determined, the last step was removing the blinding offset and reanalyzing to produce a set of frequencies for the final analysis.

[2]The F-test [103] uses the χ^2 statistics of two fits to determine the validity of adding an $(m+1)$th term

$$F_{m,m+1} = \frac{\chi^2(m) - \chi^2(m+1)}{\chi^2(m+1)/(N-m-1)}, \tag{5.8}$$

where N is the number of data points and $F_{m,m+1}$ follows the F distribution $P_F(F;\nu_1,\nu_2)$ for degrees of freedom $\nu_1 = 1$ and $\nu_2 = N-m+1$. Then, the probability $P_{m,m+1} = \int_{F_{m,m+1}}^{\infty} P_F(F;1,N-m+1)$.

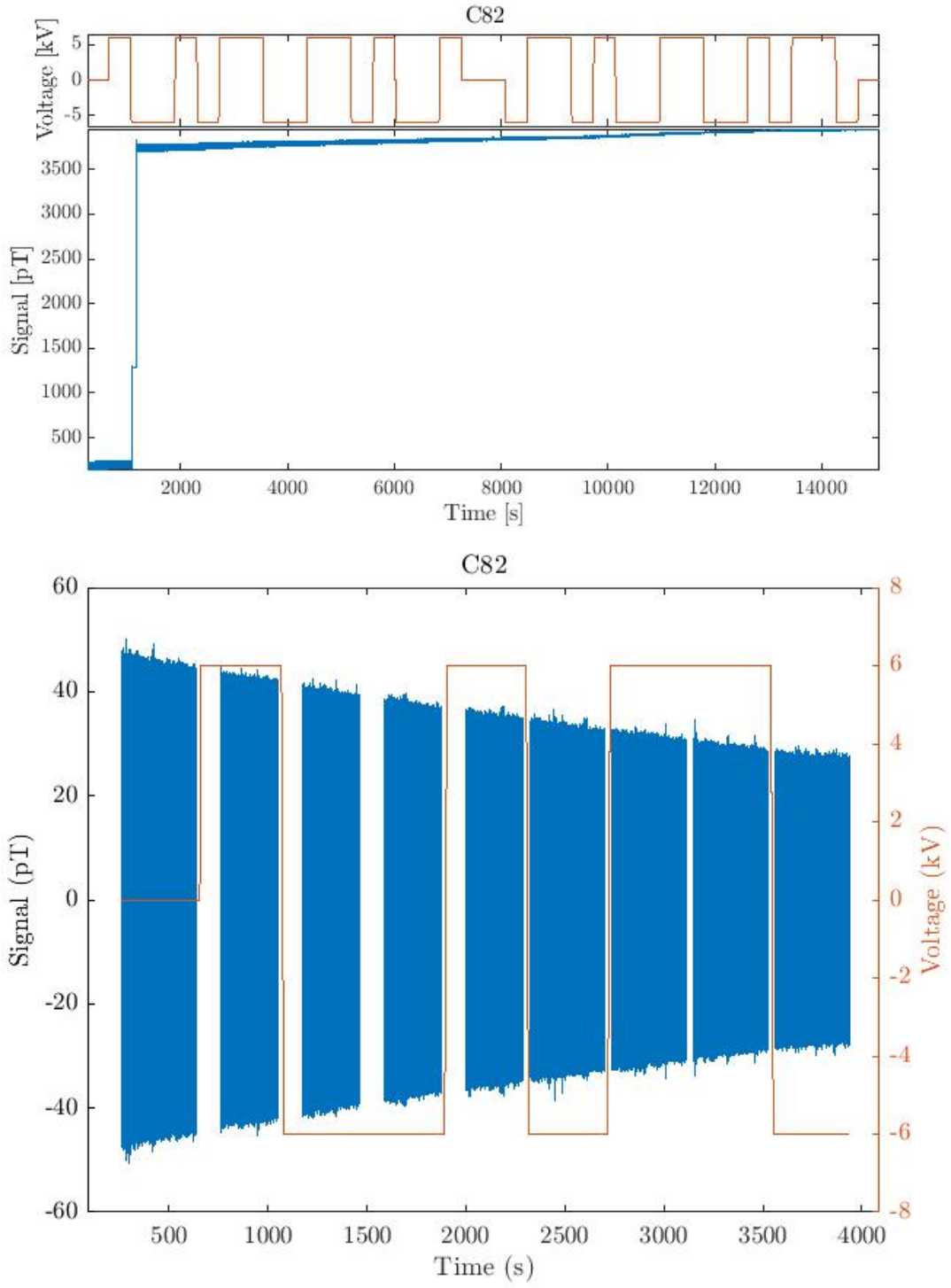

Figure 5.2: The top plots are the raw HV monitor and Z1 data from C82. Below, the filtered data divided into the first nine segments, including shortened segments from the SQUID jump.

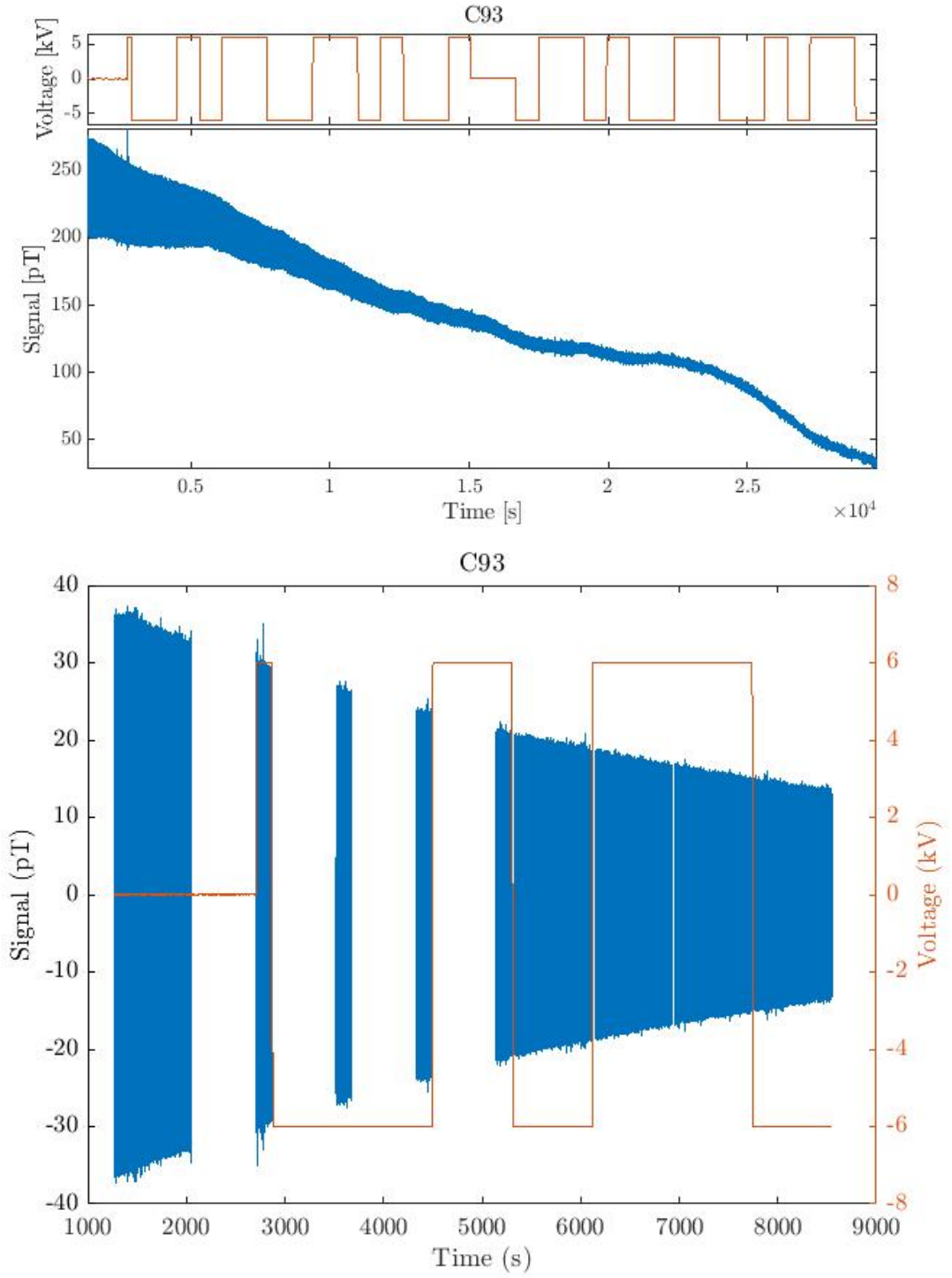

Figure 5.3: The top plots are the raw HV monitor and Z1 data from C93. Below, the filtered data divided into the first nine segments, including segments that were shortened because the HV did not turn on as intended.

Run	Cell	p [mbar]	$\hat{\mathbf{B}}_\mathbf{0}$	$T^*_{2,\mathrm{Xe}}$ [s]	$T^*_{2,\mathrm{He}}$ [s]	r_{HV} [V/s]	t_{HV} [s]	Seq.	N_{tot}	$\lvert B_0\rvert$ [μT]
C82	PP2	960	$\hat{y}$	6593	6106	1000	400	A	36	2.622
C83	PP2	420	$\hat{y}$	7583	7132	1000	400	B	36	2.622
C84	PP2	976	$\hat{y}$	6929	6420	1000	400	B	36	2.622
C85	PP2	420	$\hat{y}$	7927	7462	1000	400	A	36	2.621
C86	PP1	950	$\hat{y}$	3727	5875	1000	400	A	36	2.621
C89	PP1	443	$\hat{y}$	3798	6488	1000	400	A	36	2.621
C91	PP1	1160	$\hat{y}$	4000	6557	2000	400	B	36	2.621
C92	PP1	510	$\hat{y}$	4040	7052	2000	800	B	18	2.621
C93	PP2	975	$\hat{y}$	7245	6807	1000	800	A	35	2.621
C02	PP2	970	$\hat{y}$	5344	4867	1000	800	B	36	2.621
C08	PP2	910	$-\hat{y}$	5366	4985	1000	400	A	36	2.630
C10	PP1	1020	$-\hat{y}$	3705	5783	1000	400	B	36	2.630
C12	PP2	450	$-\hat{y}$	8579	8082	1000	400	B	36	2.630
C13	PP2	950	$-\hat{y}$	7835	7301	1000	800	A	18	2.630
C14	PP2	456	$-\hat{y}$	7697	7281	1000	400	B	36	2.630
C15	PP1	560	$-\hat{y}$	3858	6650	1000	400	A	36	2.630

Table 5.1: Run names, pressures, B_0 direction, and T_2^* times. r_{HV} is the HV ramp rate and t_{HV} is the HV dwell time or HV segment length. Sequence A is the HV polarity pattern $[0+--+-++--++-+--+00-++-+--++--+-++-0]$ and sequence B is the opposite polarity $[0-++-+--++-+-+-++-00+--+-+-++--+-+--+-+0]$. N_{tot} is the total number of segments. For runs with $N_{tot} = 18$, only the first half of the sequence was used. Data collection for C93 was accidentally stopped during the last segment with 0 HV, so it only has 35 segments.

CHAPTER VI

Systematics

6.1 Introduction

Systematics for HeXeEDM are shifts of the comagnetometer frequency that correlate with $\hat{\mathbf{E}}_\mathbf{0} \cdot \hat{\mathbf{B}}_\mathbf{0}$ or false EDMs. In this chapter, we review the systematic effect measurements and analysis for the EDM measurement data of HeXe2017. Some auxiliary measurements from HeXe2018 were used. At the end of the chapter, we tabulate the results for the total systematic error. Our approach for systematic studies for the EDM measurement is to, whenever possible, amplify an effect we expect to induce a comagnetometer response, measure that response, then scale down to the actual size determined through consistent monitoring during the experiment. The main systematic effects that can be studied in this manner are false EDMs due to leakage currents, charging currents, and HV-correlated cell motion.

6.1.1 EDM definition and sign, analysis units

Recall from Fig. 2.1 that the frequency shift due an EDM ω_d, depends on the sign of the applied electric and magnetic fields. For $\mathbf{B}_0 = +B_0\hat{\mathbf{y}}$ in the coordinate system of the BMSR-2 (see Fig. 3.6), a positive electric field $\mathbf{E}_0 = +E_0\hat{\mathbf{y}}$ reduces the precession frequency and a negative electric field $\mathbf{E_0} = -E_0\hat{\mathbf{y}}$ increases it for positive d. For $\mathbf{B_0} =$

$-B_0\hat{\mathbf{y}}$, the opposite is true. This means the EDM shift to ω' is (Eq. 2.10 for positive d)

$$\omega_d = -\frac{2d}{\hbar}\mathbf{E_0}\cdot\hat{\mathbf{B}}_\mathbf{0} \tag{6.1}$$

To review the analysis time-scales described in Ch. V, a **block** is the smallest analysis unit and describes a set of data typically over 5–20 seconds from which a time-domain fit is used to determine the phase at a well-defined time t_m at the center of the block. A **segment** describes the set of data comprised of an integral amount of blocks during which the high-voltage is constant. The comagnetometer frequency ω' is determined per segment from a linear fit of the corrected phase per block. An **EDM set** is a sequence of $N = 4$ or 8 segments with HV applied in a drift-canceling pattern. An **EDM measurement** is derived from an unweighted average of ω' from an EDM set as shown in Eq. 5.7:

$$\omega'_d = \frac{1}{N}\sum_{i=1}^{N}\mathrm{sgn}(\mathbf{E_0}\cdot\hat{\mathbf{B}}_\mathbf{0})\,\omega' = \omega_d + \omega^{\text{false}} \tag{6.2}$$

where ω^{false} is the contribution from systematic effects that manifest as a false EDM. A **run** is a single fill of a cell and consists of 16 or 32 segments with applied HV, and two or four segments with no applied HV.

6.1.2 Comagnetometer model

A false EDM is a shift of the comagnetometer frequency ω' that is correlated with $\hat{\mathbf{E}}_\mathbf{0}\cdot\hat{\mathbf{B}}_\mathbf{0}$. In order to understand false EDM signals, let us first look at the contributions to the precession frequencies of ^{129}Xe and ^{3}He in the absence of an applied electric field

$$\begin{aligned}\omega_{\text{He}} &= \gamma_{\text{He}}(1-\delta_{\text{He}})\,\langle B\rangle_{\text{He}} + \omega^{sd}_{\text{He}} + \mathbf{\Omega}\cdot\hat{\mathbf{B}}_\mathbf{0}\\ \omega_{\text{Xe}} &= \gamma_{\text{Xe}}(1-\delta_{\text{Xe}})\,\langle B\rangle_{\text{Xe}} + \omega^{sd}_{\text{Xe}} + \mathbf{\Omega}\cdot\hat{\mathbf{B}}_\mathbf{0}\end{aligned} \tag{6.3}$$

where $\gamma_{\text{He/Xe}} = 2\mu_{\text{He/Xe}}/\hbar$ is the intrinsic nuclear gyromagnetic ratio, $\delta_{\text{He/Xe}} = \sigma_{\text{He/Xe}} + \delta'_{\text{He/Xe}}$ is the species-specific chemical shift, $\sigma_{\text{He/Xe}}$ is the atomic diamagnetic shielding and $\delta'_{\text{He/Xe}}$ depends on several factors including cell pressure, temperature, and surrounding materials. $\langle B \rangle_{\text{He/Xe}}$ is the averaged magnetic field in the cell and generally is different for both species due to the different diffusion constants and $\omega^{sd}_{\text{He/Xe}}$ is the species-dependent frequency shifts discussed in Ch. IV that result in the observed comagnetometer drift. $\mathbf{\Omega}\cdot\hat{\mathbf{B}}_{\mathbf{0}}$ is the projection of the earth's rotation frequency $\mathbf{\Omega}$ onto the magnetic field $\mathbf{B_0}$. Note that contributions to $\mathbf{B_0}$ include the applied magnetic field, the residual magnetic field in the room, and any nearby magnetized materials. The earth's rotation contribution is

$$\mathbf{\Omega} \cdot \mathbf{B_0} = \Omega \cos\phi_{\text{Berlin}} \cos(\rho - 90^\circ \text{sgn}[B_0]) \tag{6.4}$$

where the earth rotation frequency $\Omega = 72.921 \times 10^{-6}$ rad/s, the latitude $\phi_{\text{Berlin}} = 52.5164^\circ$ and $\rho = 208^\circ$ is the angle of $\hat{x}$ in the coordinate system of the BMSR-2 relative to due north.

The comagnetometer frequency is the combination of the two species frequencies

$$\omega' = \omega_{\text{Xe}} - R\omega_{\text{He}}, \tag{6.5}$$

where $R = 1/r \equiv 1/2.7540816$ is the nominal ratio of the shielded gyromagnetic ratios $\frac{\gamma_{\text{Xe}}(1+\sigma_{\text{Xe}})}{\gamma_{\text{He}}(1+\sigma_{\text{He}})}$ used in the analysis. Then,

$$\omega' = [\gamma_{\text{He}}(1-\delta_{\text{Xe}})\langle B\rangle_{\text{Xe}} - R\gamma_{\text{He}}(1-\delta_{\text{He}})\langle B\rangle_{\text{He}}] + (\omega^{sd}_{\text{Xe}} - R\omega^{sd}_{\text{He}}) + (1-R)\mathbf{\Omega}\cdot\hat{\mathbf{B}}_{\mathbf{0}}. \tag{6.6}$$

For small changes in $\delta_{\text{Xe/He}}$ and $\langle B\rangle_{\text{Xe/He}} = B_0 + \Delta B_{\text{Xe/He}}$, the comagnetometer frequency

Parameter	Value
Electric field	$\lvert E\rvert$ = 2.94 kV
Magnetic field gradient	$\left\lvert\frac{\partial B_y}{\partial y}\right\rvert = \lvert G_{yy}\rvert$ = 30 nT/m
Comagnetometer B_0 response	$\frac{1}{2\pi}\frac{\partial \omega'}{\partial B}$ = 3 Hz/T
Comagnetometer gradient response	$\frac{1}{2\pi}\frac{\partial \omega'}{\partial H_{yy}} = 0.17 \pm 0.09$ Hz/(T/m^2)

Table 6.1: Parameters used for estimates of systematic effects.

is

$$\begin{aligned}\omega' \approx & - \gamma_{\mathrm{He}}(1-\sigma_{\mathrm{He}})\Delta R B_0 \\ & + \gamma_{\mathrm{Xe}}(1-\sigma_{\mathrm{Xe}})(\Delta B_{\mathrm{Xe}} - \Delta B_{\mathrm{He}}) \\ & + \omega^{sd}_{\mathrm{Xe}} - R\omega^{sd}_{\mathrm{He}} \\ & + (1-R)\boldsymbol{\Omega}\cdot\hat{\mathbf{B}}_{\mathbf{0}}. \end{aligned} \tag{6.7}$$

The first term in Eq. 6.7 refers to an offset in the comagnetometer frequency proportional to B_0 that results from varying chemical shift ΔR caused by different pressures, etc. The second term refers to frequency shift caused by a difference in the averaged magnetic field by the two species because of different diffusion and 2$^{\text{nd}}$ and higher order gradients across the cell. The third term refers to the comagnetometer drift discussed in Ch. IV. The last term is the contribution from the earth's rotation and couples any change in the direction of $\hat{\mathbf{B}}_{\mathbf{0}}$. Note that in Eq. 6.7 we've neglected $v \times E$ effects which are negligible as discussed in Section 6.6.

6.1.3 Assumed parameters

6.1.3.1 Electric field strength

The same high-voltage of 6 kV was applied to the cells for all runs. However, each cell has a different length with $l_{\mathrm{PP1}} = 1.85$ cm and $l_{\mathrm{PP2}} = 2.18$ cm. Then, for the six runs using

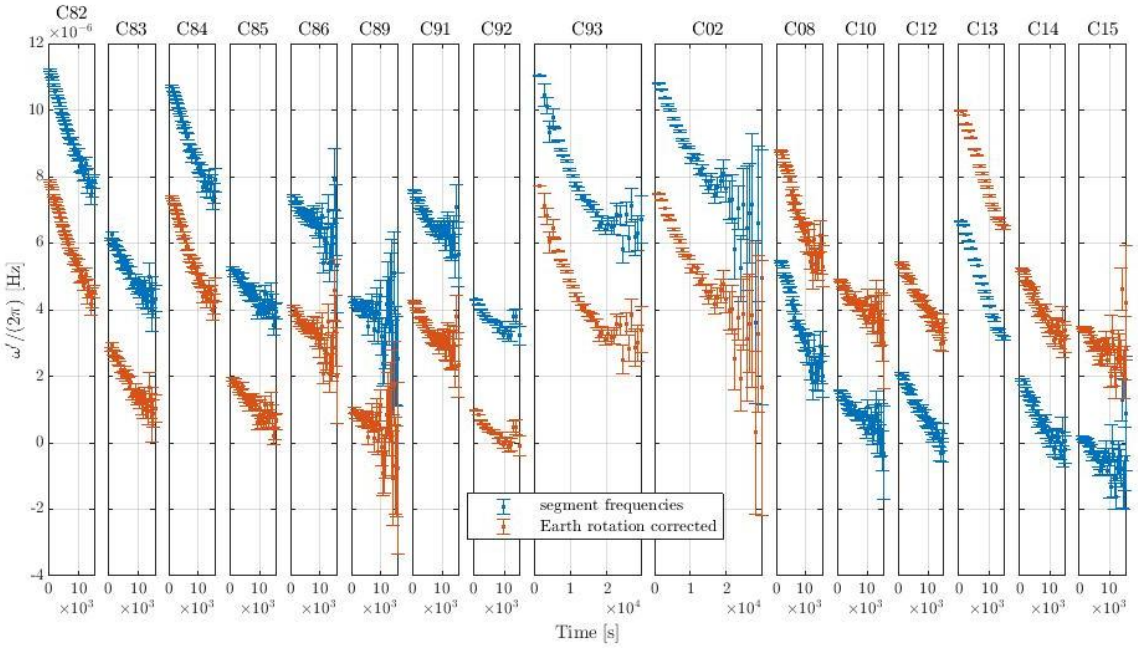

Figure 6.1: All blinded HV segment frequencies as extracted during analysis ω' and after correction for the earth's rotation. Note that the blinding frequency is small ($|\omega_{\text{blind}}|/(2\pi) < 50$ nHz) compared to the absolute frequency. The drift observed is a result of the comagnetometer drift discussed in Ch. IV and Ref. [95].

PP1, the electric field is $|E| = 3.24$ kV/cm and for the remaining ten runs with PP2 $|E| = 2.75$ kV/cm. For some systematic effect calculations, the different electric field strengths are taken into account. For global estimates, we use the average $|E| = 2.94$ kV/cm, which is a weighted average of E for each run.

6.1.3.2 Magnetic field gradients

The first-order gradient $G_{yy} = \frac{\partial B_y}{\partial y}$ is estimated from the T_2^* times for ^{129}Xe and ^{3}He provided in Table 5.1. The minimum observed T_2^* values were $T^*_{2,\text{Xe}} = 3705$ s in run C10 and $T^*_{2,\text{He}} = 4867$ s in run C02. Using Eq. 2.31 to estimate the worst-case gradient, we find $|G_{yy}|$ =30 nT/m.

6.1.3.3 Comagnetometer B_0 sensitivity

The comagnetometer-B sensitivity $\frac{\partial\omega'}{\partial B}$ refers to the ω' frequency offset resulting from uncertainty in R due to chemical shifts, variations in the cell glass, pressure, and other effects, ΔR. In Fig. 6.1, we see that the comagnetometer drift dominates at the beginning of a run. We used the absolute frequencies at the end of each run to estimate $\frac{\partial\omega'}{\partial B}$. The difference between the maximum and minimum value was used as $\Delta\omega'$.

$$\frac{1}{2\pi}\frac{\partial\omega'}{\partial B} = \frac{8.2\ \mu\text{Hz}}{2.6\ \mu\text{T}} = 3\ \text{Hz/T} \tag{6.8}$$

6.1.3.4 Comagnetometer gradient sensitivity

The comagnetometer gradient sensitivity is the response of ω' to magnetic field gradients. The second term in Eq. 6.7 arises from a difference in the magnetic field averaging by the two species due to diffusion. As long as the diffusion time for each species is much less than T_2^*, a first order gradient will be averaged the same way for each species. However, a second-order and higher magnetic gradient will be averaged differently [107]. We studied the comagnetometer response to gradients by "loop-tests," where a wire was looped around the stem of a valved EDM cell or taped to the opposite electrode and current on the order of μA was applied. The change in ω' for different applied currents was measured. For a loop of radius a, the magnetic moment and magnetic field along its axis $\hat{y}$ are

$$\mu^{\text{loop}} = \pi a^2 I \qquad B_z^{\text{loop}} = 2\frac{\mu_0 I \pi a^2}{4\pi r^3}, \tag{6.9}$$

where $r = \sqrt{a^2 + z^2}$. The 1st, 2nd, and 3rd order gradients are

$$\begin{aligned} G_{yy}^{\text{loop}} &= \frac{\partial B_z}{\partial z}^{\text{loop}} = -6\frac{\mu_0 I \pi a^2 z}{4\pi r^5} \\ H_{yy}^{\text{loop}} &= \frac{\partial^2 B_z}{\partial z^2}^{\text{loop}} = 6\frac{\mu_0 I \pi a^2}{4\pi r^5}\left[5\frac{z^2}{r^2} - 1\right] \\ K_{yy}^{\text{loop}} &= \frac{\partial^3 B_z}{\partial z^3}^{\text{loop}} = 6\frac{\mu_0 I \pi a^2}{4\pi r^7}\left[15z - 35\frac{z^3}{r^2}\right] \end{aligned} \tag{6.10}$$

There were two such measurements performed: one was during HeXe2017 using cell PP1 and the a = 0.5 cm loop wrapped around the stem approximately 1 cm away from the electrode; the other measurement was performed at the TUM MSR a month later using a valved EDM cell E2 with a loop of radius a = 0.5 cm attached directly to the electrode opposite the stem. Both results are presented below, but for the HeXe2017 systematic analysis we used the latter measurement because the loop was closer to the cell and therefore higher order gradient terms were more significant. The size of the 1st, 2nd, and 3rd order gradients in the cell for each measurement is illustrated in Fig. 6.2.

For the HeXe2017 loop-test measurement, current was applied to the loop in the following order: 0, 2, 0, -2, 0, 2, 4, -2, -4, 0 uA. The data were divided into segments based on the applied current, and then further divided into blocks. Similar to the analysis in Ch. V, the data in the blocks were fit to determine the phase, and a linear fit of the comagnetometer-corrected phases provided the comagnetometer frequency of each segment. The ^{3}He frequencies per segment were determined similarly. Fig. 6.3 shows ω' vs. applied current as well as the change in the comagnetometer frequency between consecutive segments, $\delta\omega'$ vs. the change in the ^{3}He frequency, $\delta\omega_{\text{He}}$.

For the loop-test measurement at the TUM MSR in August 2017, current was applied in the following order: 0, 10, 100, 0, 100 μA. The results are summarized in Fig. 6.4. Using Eq. 6.10 we can estimate the size of the magnetic field gradient in the cell and use the slope in Fig. 6.5a for

$$\frac{1}{2\pi}\frac{\partial\omega'}{\partial H_{yy}} = 0.16 \pm 0.09 \ \frac{\text{Hz}}{\text{T/m}^2}. \tag{6.11}$$

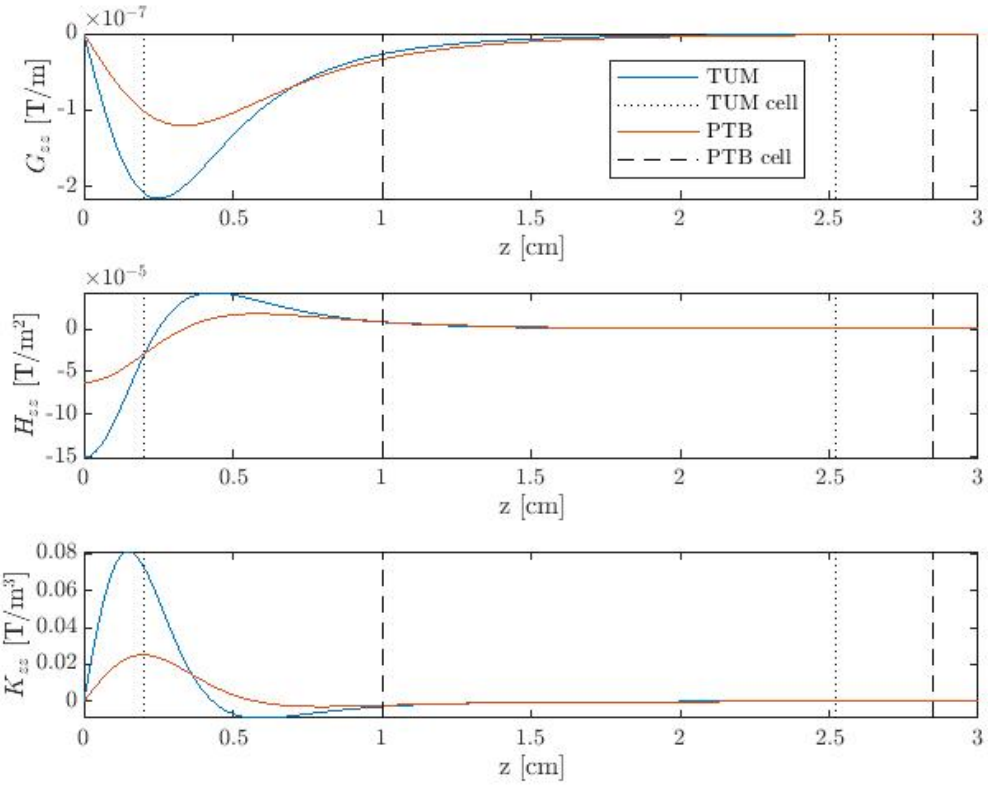

Figure 6.2: Calculation of the 1st through 3rd order magnetic field gradients using Eq. 6.10 for the TUM and PTB loop tests. The dotted and dashed black lines indicate the cell boundary for the TUM and PTB cells, respectively. Gradients were calculated for a 10 μA applied current.

In Ref. [107] the authors present a scaling argument that the comagnetometer frequency dependence is proportional to H_{yy}^3. A fit to the dependence on H_{yy}^3 is

$$\frac{1}{2\pi}\frac{\partial\omega'}{\partial(H_{yy})^3} = 2.1 \times 10^7 \pm 9.3 \times 10^6 \ \frac{\text{Hz}}{(\text{T/m}^2)^3} \tag{6.12}$$

6.2 Leakage current

When HV is applied to the EDM measurement cell, current may flow between the electrodes, following an unknown path dependent on the bulk resistance of the cell glass

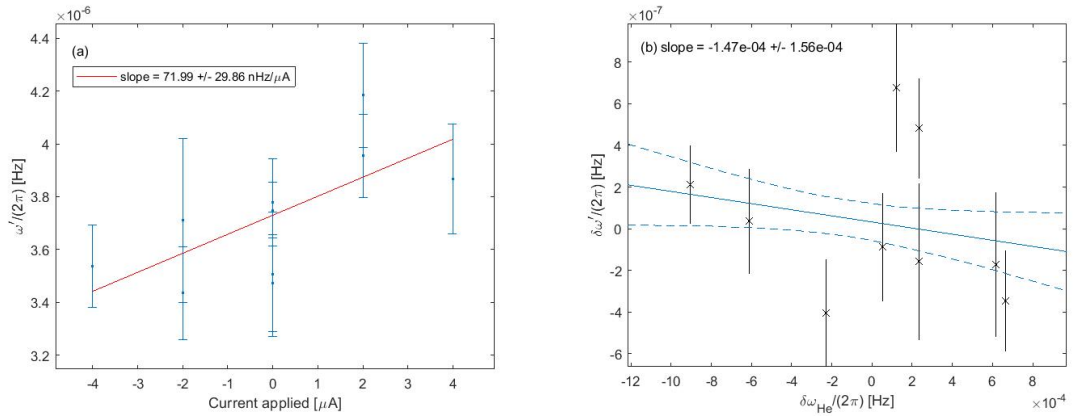

Figure 6.3: Results of the loop-test measurement during HeXe2017 in June 2017. (a) The extracted comagnetometer frequency $\omega'/(2\pi)$ vs. applied current and (b) $\delta\omega'$ vs. $\delta\omega_{\mathrm{He}}$. $\delta\omega$ is the change in ω from the previous segment. Analysis using $\delta\omega$ instead of ω is less sensitive to comagnetometer and B_0 drift.

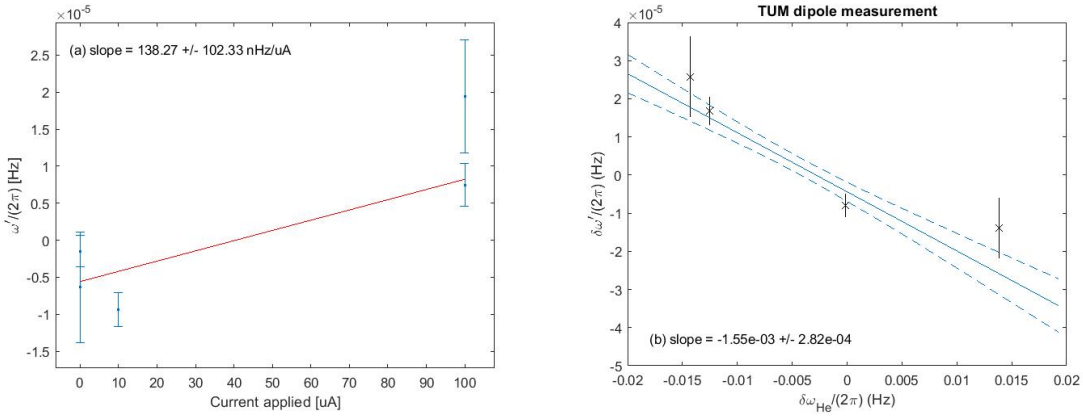

Figure 6.4: Results of the loop test at TUM in August 2017. (a) The extracted comagnetometer frequency $\omega'/(2\pi)$ vs. applied current and (b) $\delta\omega'$ vs. $\delta\omega_{\mathrm{He}}$.

and inner and outer surfaces. The worst-case scenario would be if the current followed a spiral path between the electrodes to produce a HV-dependent magnetic field that adds to $\mathbf{B_0}$, imitating an EDM. The comagnetometer mitigates the effect of a leakage current since the ^{3}He couples to the same leakage-current-induced magnetic field. To test the effectiveness of the comagnetometer cancellation, we performed a test by wrapping a wire one full turn around the cell and applying currents ranging from -1 μA to +1 μA. The result

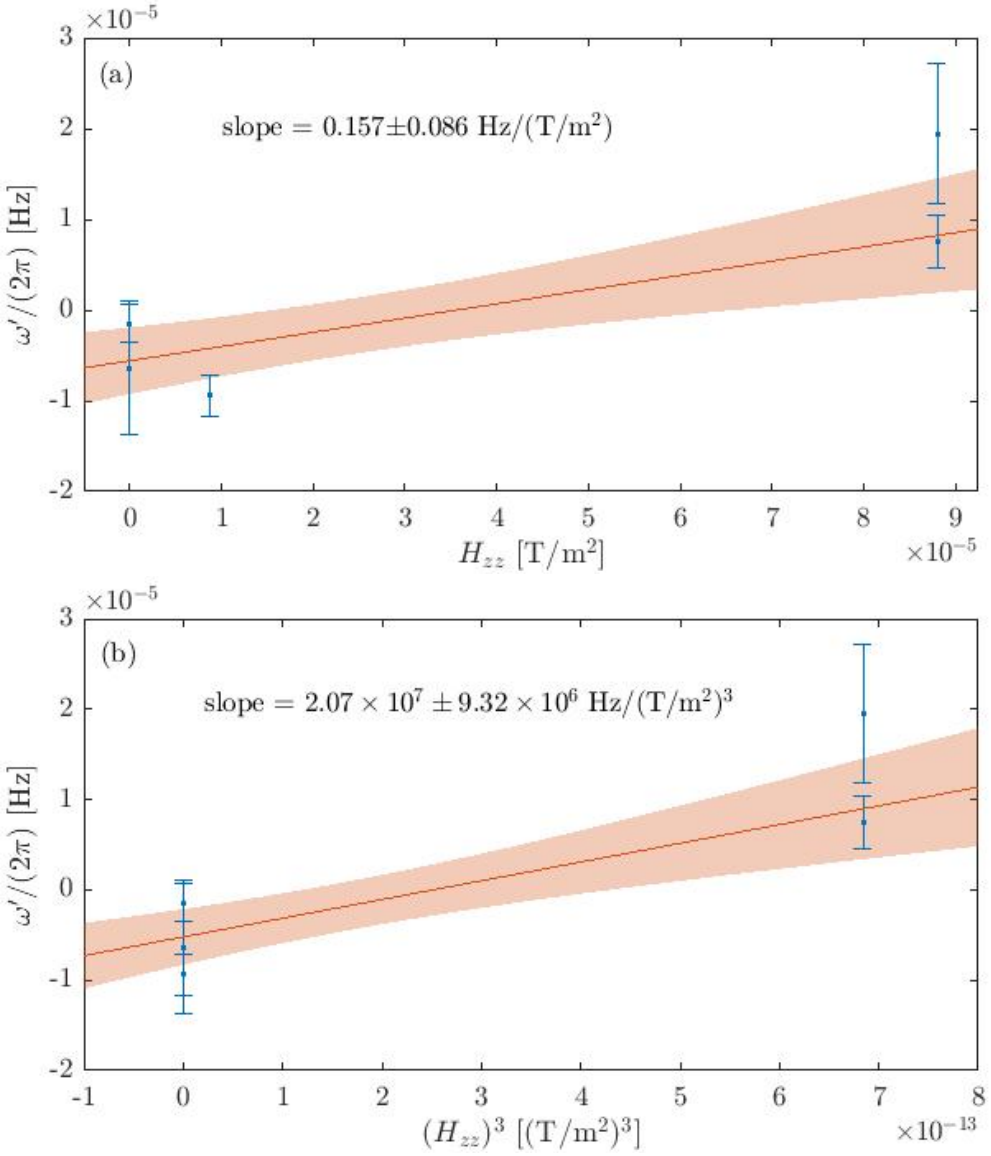

Figure 6.5: (a) ω' vs H_{yy}^{loop} and (b) vs. $H_{yy}^{3,\text{loop}}$ from the TUM dipole measurement, using Eq. 6.10.

of this test is summarized in Fig. 6.6 and the comagnetometer response measured was

$$\frac{1}{2\pi}\frac{\partial\omega'}{\partial I_{\text{applied}}} = -1.36 \pm 0.90\ \mu\text{Hz}/\mu\text{A} \leq 1.77\ \mu\text{Hz}/\mu\text{A}\ (68\%\ \text{c.l.}) \tag{6.13}$$

To estimate the systematic error from a leakage current for HeXe2017, we scaled this result by the maximum leakage current measured. The leakage current was monitored throughout

each run and recorded on a channel in the DAQ. The maximum leakage current measured per run is provided in Table 6.2. We opted to use the maximum leakage current observed to estimate a global false EDM rather than a run-by-run correction. Note that the sign of the correction is unknown. Aside from different cells, the leakage current may be different run-to-run because of cell-handling and may change even within a run. The maximum leakage current was 97 pA observed in run C92. Combined with the average $|E| = 2.94$ kV, the 68% upper limit on the magnitude of the false EDM is $|d^{\text{false}}_{\text{leakage}}| \leq 1.2 \times 10^{-28}\, e\,\text{cm}$.

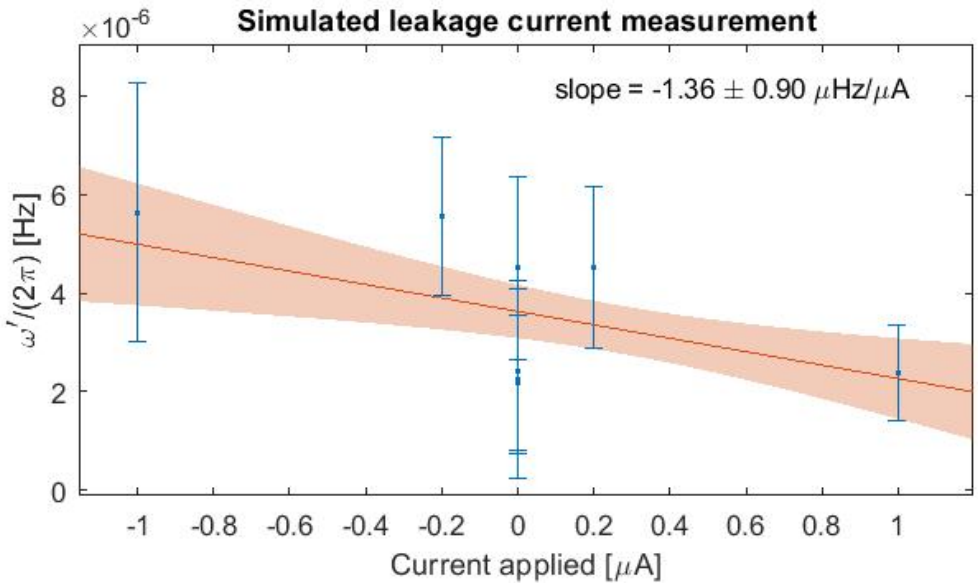

Figure 6.6: ω' vs. I_{applied} from the simulated leakage current measurement.

6.3 Charging current

Charging currents during HV ramping $I_{\text{charging}} = C\frac{\text{d}V}{\text{d}t}$ can magnetize materials on or near the measurement cell, like the valve o-ring. If a nearby material is magnetized by charging currents, it may contribute to a false EDM by changing $|B|$ (first term in Eq. 6.7), creating a gradient (second term), or changing $\hat{B}$ (fourth term). The comagnetometer response to an exaggerated "charging current" was measured by applying current to the cell in a pattern similar to an actual charging current. Similar to the leakage current test, the re-

Run	Cell	$\left\lvert I^{\max}_{\text{leakage}} \right\rvert$ [pA]	$\left\lvert I^{\max}_{\text{charging}} \right\rvert$ [nA]
C82	PP2	23	15
C83	PP2	33	19
C84	PP2	33	19
C85	PP2	24	18
C86	PP1	28	18
C89	PP1	23	18
C91	PP1	33	16
C92	PP1	97	11
C93	PP2	53	11
C02	PP2	23	11
C08	PP2	33	12
C10	PP1	20	N/A
C12	PP2	24	N/A
C13	PP2	17	N/A
C14	PP2	17	N/A
C15	PP1	20	N/A

Table 6.2: Magnitude of the maximum leakage current and charging current measured per run. For the last few runs the readout was blanked for the charging current so that the leakage current could be monitored more accurately without having to rescale the voltmeter.

sult was scaled by the maximum measured charging current during HeXe2017 to determine the false EDM.

The charging current test was performed in the summer of 2018 by applying fixed charging currents of 10 μA and 20 μA to the cell by shorting out the cell with a wire and applying ± 100 or 200 V from the HV supply with current limited by a 10 MΩ series resistor. The voltage was applied over a time interval and with polarity according the charging current pattern for a HV sequence of $+--+-++-$ and $-++-+--+$

and a segment length of 100 seconds. The comagnetometer response observed was

$$\frac{1}{2\pi}\frac{\partial\omega'}{\partial I_{\text{charging}}} = -0.3 \pm 1.2 \text{ nHz}/\mu\text{A} \leq 1.23 \text{ nHz}/\mu\text{A } 68\% \text{ c.l.}, \tag{6.14}$$

combined with a maximum measured charging current of 20 nA, we find for the false EDM due to charging currents $|d^{\text{false}}_{\text{charging}}| \leq 1.7 \times 10^{-29}\, e\,\text{cm}$.

6.4 Comagnetometer drift

Comagnetometer drift is caused by the third term in Eq. 6.7 which refers to the species-dependent drifts discussed in Ch. IV. To extract an EDM, we must separate the comagnetometer drift from an EDM frequency which is modulated by $\hat{\mathbf{E}} \cdot \hat{\mathbf{B}}_{\mathbf{0}}$. Eq. 5.7 illustrates how a linear drift is separable from an EDM using a $\hat{\mathbf{E}}$ flip pattern of $+--+$. Similarly, a pattern of eight cancels up to a quadratic drift, a pattern of 16 cancels up to cubic drift, and a pattern of 32 cancels up to a quartic drift. We chose to apply HV in a pattern of 36, including zero HV segments at the beginning and middle, for all runs except two runs that used a half-pattern of 18. It can be shown that the zero HV segments in the middle do not affect the quartic drift cancellation. Combining segments in a drift-canceling pattern is essentially an unweighted average. Because the signal-to-noise decreases with T_2^* decay of both species, longer patterns have reduced statistical sensitivity.

There were two approaches considered for evaluating the comagnetometer drift. The first approach was to compare the results from four, eight, 16, and 32 segment blinded EDM measurements, and the second approach was to parametrize the drift as a polynomial and determine the correction $\omega^{\text{false}}_{\text{drift}}$ by fitting ω' vs. time. Both are discussed below. For the final analysis, we used combined segment frequencies in a sequence of four and used the polynomial correction method to determine the systematic error from higher order drifts. Initial corrections were determined with blinded data. Because the blinding EDM shift is different for each cell, the final correction may change after unblinding.

6.4.1 Comparing sequence lengths

For the pattern-combination, all segments within a set must be of equal length. For the runs with shortened segments discussed in Ch. V, a total of N segments were shortened, where N is the pattern length. For this comparison, a data set was generated for $N = 16$ where the first 16 nonzero HV segments of the three irregular data sets (C82, C93, and C13) were shortened by equal amounts. For a pattern of N, the EDM frequency of a set is determined from the segment frequencies ω'_i as shown in Eq. 6.2. The results are provided in Table 6.3. The blinding was applied as an added frequency, which means the EDM shift is different for each cell. For comparing the correction from different sequence lengths, we look at the blinded frequency shifts for each cell separately. For unblinded data, we perform a E^2-weighted average ($w_i = E_i^2/\sigma_i^2$) for the full data set. This average is added Table 6.3 for completeness.

Cell	PP1	PP2	avg.
$\frac{1}{2\pi}\bar{\omega}'_d(N=4)$ [nHz]	-21.73 $\pm$ 6.61	-19.48 $\pm$ 4.15	-19.98 $\pm$ 3.40
$\frac{1}{2\pi}\bar{\omega}'_d(N=8)$ [nHz]	-21.91 $\pm$ 7.42	-19.17 $\pm$ 4.48	-19.74 $\pm$ 3.70
$\frac{1}{2\pi}\bar{\omega}'_d(N=16)$ [nHz]	-20.21 $\pm$ 10.74	-24.52 $\pm$ 5.91	-23.75 $\pm$ 4.96
$\frac{1}{2\pi}\left[\bar{\omega}'_d(4)-\bar{\omega}'_d(8)\right]$ [nHz]	0.19 $\pm$ 3.37	-0.31 $\pm$ 1.69	-0.24 $\pm$ 1.46
$\frac{1}{2\pi}\left[\bar{\omega}'_d(4)-\bar{\omega}'_d(16)\right]$ [nHz]	-1.51 $\pm$ 8.46	5.04 $\pm$ 4.02	3.77 $\pm$ 3.62

Table 6.3: Comparison of the blinded EDM determined from a weighted average of ω'_d for each cell and sequence length.

6.4.2 Polynomial parametrization

The comagnetometer frequency can be parametrized as

$$\omega' = a_0 + a_1 t + a_2 t^2 + \cdots + \mathrm{sgn}(\hat{\mathbf{E}}\cdot\hat{\mathbf{B}})\,\omega_d \tag{6.15}$$

where a_n has units of rad/s^{1+n}. For a sequence of $N = 4$ and equally spaced segments of length Δt the frequency extracted from an EDM set is

$$\omega'_d = \frac{1}{4}\sum_i^4 \omega'_i = \omega_d + a_2(\Delta t)^2 + 7.5a_3(\Delta t)^3 + 40a_4(\Delta t)^4 + \cdots = \omega_d + \omega_{\text{drift}}^{\text{false}} \quad (6.16)$$

For each run, ω' vs. time (as seen in Fig. 6.1) was fit to 2$^{\text{nd}}$, 3$^{\text{rd}}$, and 4$^{\text{th}}$ order polynomials. An F-test (Eq. 5.8) was used to determine the significance of each increasing order and the results for each run are provided in Table 6.4. The corrections for each run were determined from the fitted polynomial coefficients and $\omega_{\text{drift}}^{\text{false}}$ was evaluated using Eq. 6.16 and the appropriate segment numbers and intervals. The blinded, drift-uncorrected result using a

Run	Cell	$P_{1,2}$	$P_{2,3}$	$P_{3,4}$	order
C82	PP2	1.0000	0.8644	0.8460	4
C83	PP2	0.9756	0.8489	0.0795	3
C84	PP2	1.0000	0.9756	0.4538	3
C85	PP2	0.9004	0.4811	0.1358	2
C86	PP1	0.9792	0.8852	0.8569	4
C89	PP1	0.1351	0.5741	0.4716	none
C91	PP1	1.0000	0.3362	0.6506	4
C92	PP1	1.0000	0.7330	0.7044	4
C93	PP2	1.0000	0.9855	0.5512	3
C02	PP2	1.0000	0.0412	0.9432	4
C08	PP2	0.9947	0.9992	0.0080	3
C10	PP1	1.0000	0.8880	0.8583	4
C12	PP2	0.9851	0.3748	0.0845	2
C13	PP2	0.5387	1.0000	0.6687	4
C14	PP2	0.9998	0.7233	0.5158	3
C15	PP1	0.9936	0.8500	0.7783	4

Table 6.4: Probabilities from F-tests of increasing polynomial order. The last column is the order used to fit and obtain the correction coefficients based on a probability threshold $P \geq 0.6$. No correction was applied to C89.

sequence length of $N = 4$ and weighting by $w_i = E_i^2/\sigma_i^2$ for the different cells

$$\frac{1}{2\pi}\omega_d' = -20.14 \pm 3.39 \text{ nHz} \tag{6.17}$$

After drift correction using the polynomial orders for each run provided in Table 6.4 based on an F-test probability $P \geq 0.6$ for adding another order and $\omega_{\text{drift}}^{\text{false}}$ evaluated for each EDM set,

$$\frac{1}{2\pi}\omega_d = -20.25 \pm 3.53 \text{ nHz} \tag{6.18}$$

The difference between these two numbers gives a false EDM frequency of $\frac{1}{2\pi}\omega_{\text{drift}}^{\text{false}} = -0.11 \pm 0.98$ nHz and a false EDM of $d_{\text{drift}}^{\text{false}} = (-2.16 \pm 6.73) \times 10^{-28}\, e\,\text{cm}$. After unblinding, these numbers changed slightly because the blind EDM shift was slightly different for each cell. Therefore, the final EDM correction was

$$d_{\text{drift}}^{\text{false}} = (-0.75 \pm 6.67) \times 10^{-28}\, e\,\text{cm} \tag{6.19}$$

6.5 Cell motion

Electrostatic force between the HV electrode and the grounded safety electrode may cause HV-correlated cell movement. There are a few sources of false EDMs due to translation and rotation of the cell. Translation of the cell causes the cell to experience a different magnetic environment; in particular different magnetic gradients couple to ω' through the second term in Eq. 6.7 and a slightly different B_0 couples to the first term. Rotation of the cell additionally may cause rotation of $\hat{\mathbf{B}}_\mathbf{0}$ in the case of magnetized cell components like the o-ring, which couples to ω' through the earth rotation term in Eq. 6.7 and species-dependent shifts. We were unable to complete a direct study of the comagnetometer response due to cell motion but were able to set a limit of the cell motion systematic effect

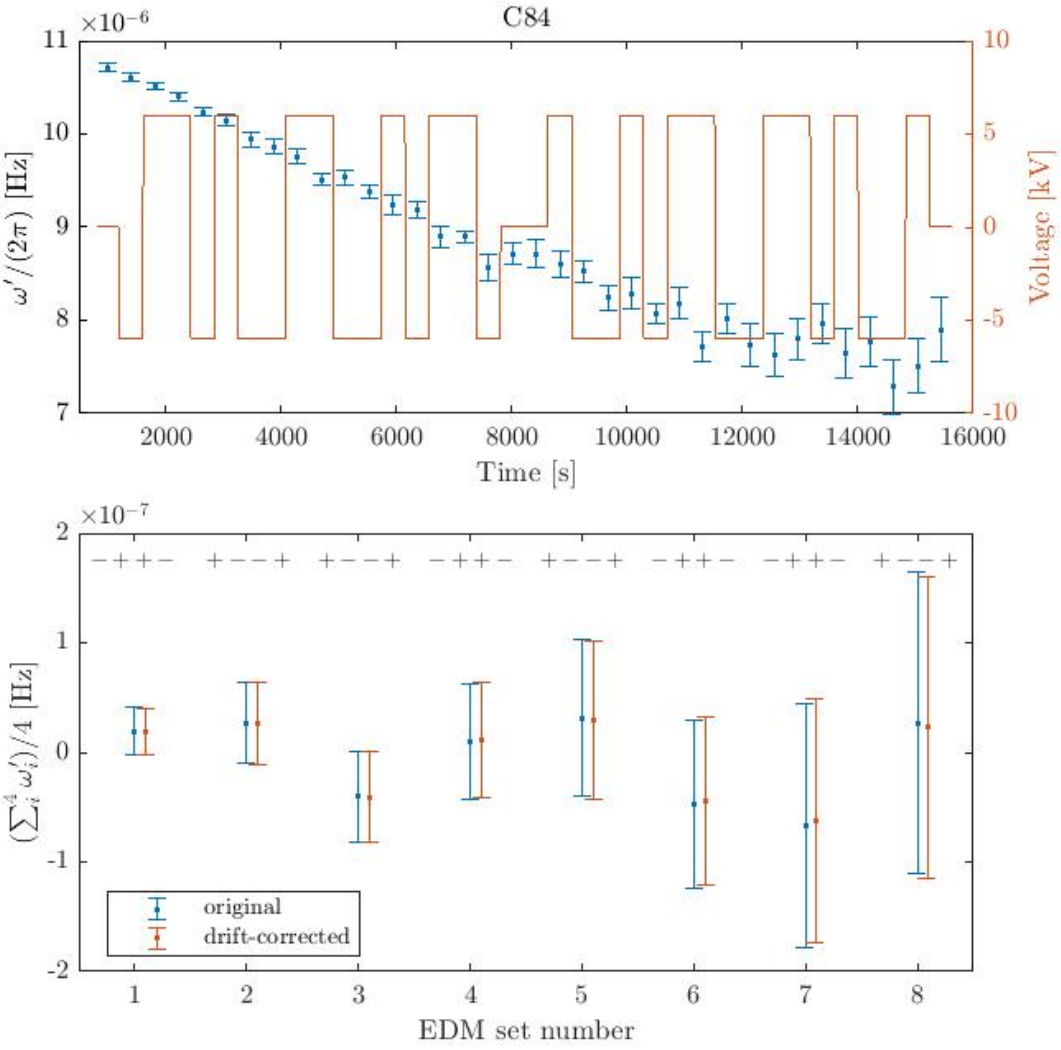

Figure 6.7: ω' and applied HV vs. time for run C84 (top). Linear drift can be canceled by combining frequencies in a sequence of four (bottom). Higher order drifts can be further corrected using the procedure outlined in the text.

by other means discussed below.

6.5.1 Estimates of cell motion

6.5.1.1 Laser beam measurement

A limit of the HV-correlated cell motion was obtained in 2018 through a test using a laser beam aimed at the cell electrode and reflected on the wall of the BMSR-2. The cell axis was along $\hat{y}$ as it is during the experiment. An angle ϕ corresponds to the rotation

around $\hat{z}$, and the angle θ corresponds to rotation about $\hat{x}$. The motion of the beam's reflection on the wall was observed as the HV was changed by ± 9 kV. The rotation was calibrated by rotating the cell $\phi = +5^\circ$ and -5°, which moved the reflection on the wall $x' =$283 mm and 334 mm, respectively, and results in a calibration factor of $\frac{\partial \phi}{\partial x'} = \frac{\partial \theta}{\partial x'} \approx 0.28$ mrad/mm. The observed shifts for ΔHV = 18 kV were

$$\begin{aligned} \Delta x &= 0 \pm 0.3 \text{ mm}, & \Delta\phi &= 0 \pm 0.1 \text{ mrad}, \\ \Delta z &= 0 \pm 0.2 \text{ mm}, \quad \text{and} & \Delta\theta &= 0 \pm 0.06 \text{ mrad}. \end{aligned} \tag{6.20}$$

Combining with the calibration factor we find

$$\Delta\phi \approx \Delta\theta \approx 5.5 \ \mu\text{rad/kV}, \tag{6.21}$$

or ≤ 33 μrad for 6 kV.

6.5.1.2 Estimate of cell translation from precession amplitudes

An estimate of cell translation can be derived from observed precession amplitude modulation due to HV polarity switching combined with numerical calculations of the change in flux Φ_B through a SQUID loop 0.034 m from the center of the cell. The dependence is

$$\frac{1}{\Phi_B}\frac{\mathrm{d}\Phi_B}{\mathrm{d}x} = -0.05 \text{ cm}^{-1}, \quad \frac{1}{\Phi_B}\frac{\mathrm{d}\Phi_B}{\mathrm{d}y} = -0.05 \text{ cm}^{-1}, \quad \frac{1}{\Phi_B}\frac{\mathrm{d}\Phi_B}{\mathrm{d}z} = -0.91 \text{ cm}^{-1}. \tag{6.22}$$

The worst-case scenario for motion along x or y is

$$\Delta x = \Delta y = 0.20 \text{ m} \left(\frac{\Delta S}{S}\right), \tag{6.23}$$

where S is the spin precession amplitude for ^{3}He or ^{129}Xe. To estimate $\Delta S/S$ a method similar to the EDM pattern analysis was used on the precession amplitudes for each seg-

ment. An 8-segment pattern analysis on the ^{3}He amplitudes was used to get

$$\frac{\Delta S}{S} = -6.24 \times 10^{-5} \pm 8.53 \times 10^{-5}, \text{or} \quad \left|\frac{\Delta S}{S}\right| \leq 1.6 \times 10^{-4} \text{ (68\% c.l.)} \tag{6.24}$$

which provides a limit of

$$\Delta x \leq 3 \times 10^{-5} \text{ m} \quad \text{or} \quad \Delta y \leq 3 \times 10^{-5} \text{ m}. \tag{6.25}$$

6.5.2 Rotation

To estimate the change in ω' due to cell rotation, during HeXe2018 we measured ω' while changing the angle $\pm 5^\circ$ near the nominal cell orientation along $\hat{y}$ or $\phi = 270^\circ$ in the coordinate system of the room. Fig. 6.8 shows the results, where the segment lengths were chosen to be short enough to ensure linear phase.

Let α be the angle deviation from the nominal B_0 direction. Recall from Eq. 6.4 and Eq. 6.7 that the shift in ω' due to rotation is $\propto \cos(\rho' - \alpha) \approx \cos\rho' \sin\alpha$ where $\rho' = \rho - 90^\circ \text{sgn}[\hat{B}_0]$. Using this and that we expect a term proportional to $\sin^2\alpha$ from species-dependent drifts, we expect comagnetometer drift due to rotation to have the following dependence

$$\omega'_{\text{rotation}} = b_0 + b_1 \sin\alpha + b_3 \sin^2\alpha \tag{6.26}$$

where the coefficients b_n all have units of rad/s. Using the data in Fig. 6.8b,

$$\frac{b_0}{2\pi} = 4.9 \ \mu\text{Hz} \qquad \frac{b_1}{2\pi} = 1.6 \ \mu\text{Hz} \qquad \frac{b_2}{2\pi} = 44.2 \ \mu\text{Hz} \tag{6.27}$$

For small angles α the shift is

$$\delta\omega'_{\text{rot}} \approx \alpha \frac{\partial \omega'}{\partial \alpha} = b_1\alpha + 2b_2\alpha^2. \tag{6.28}$$

Then, using $\alpha_{\mathrm{HV}} \leq 33\ \mu$rad for 6 kV,

$$\begin{aligned} \frac{\omega_{\mathrm{rotation}}^{\mathrm{false}}}{2\pi} &\leq 0.06\ \mathrm{nHz} \\ d_{\mathrm{rotation}}^{\mathrm{false}} &\leq 4.2 \times 10^{-29}\ e\,\mathrm{cm}. \end{aligned} \tag{6.29}$$

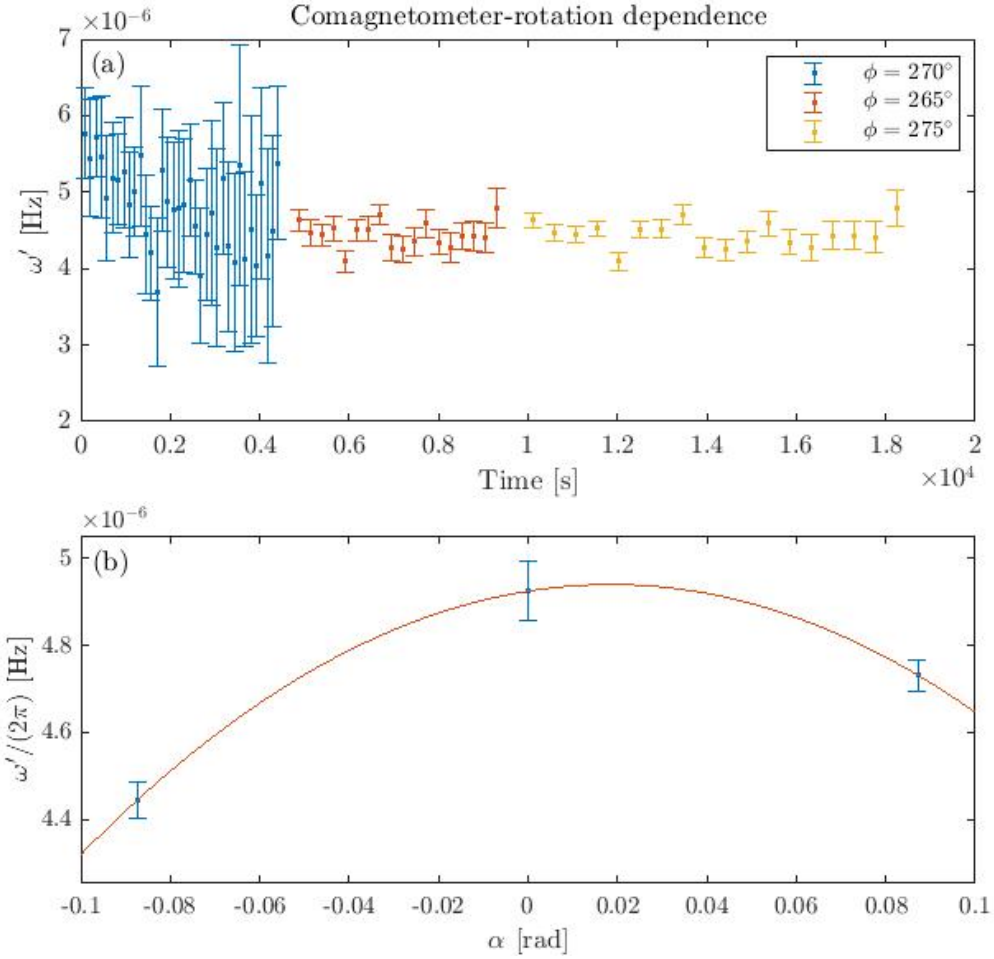

Figure 6.8: ω' vs. time (top) and ω' vs. α (bottom) for angle dependence measurement.

6.5.3 Translation

Cell translation influences ω' through the first, second, and fourth terms of Eq. 6.7 corresponding to a change in the magnitude of B_0 and changes in magnetic gradients. Because we do not have a direct measurement of the comagnetometer response to cell

translation, we address both contributions individually using available data to estimate the false EDM. For future HeXeEDM measurements, the comagnetometer response to cell translation will be directly measured.

6.5.3.1 Effect of translation on B_0 dependence

The change in the comagnetometer frequency due to cell translation is

$$\omega^{\text{false}}_{\text{translation}} = \frac{\partial \omega'}{\partial x}\Delta x, \quad \omega^{\text{false}}_{\text{translation}} = \frac{\partial \omega'}{\partial y}\Delta y, \quad \omega^{\text{false}}_{\text{translation}} = \frac{\partial \omega'}{\partial z}\Delta z. \tag{6.30}$$

Then, using values from Table 6.1 we estimate for a HV-correlated change $\Delta y \leq 3 \times 10^{-5}$

$$\frac{\omega^{\text{false}}_{\text{translation}}}{2\pi} = \frac{1}{2\pi}\frac{\partial \omega'}{\partial B}\frac{\partial B}{\partial y}\Delta y = \left(3\frac{\text{Hz}}{\text{T}}\right)\left(30\frac{\text{nT}}{\text{m}}\right)\Delta y \leq 2.7 \times 10^{-3}\ \text{nHz}, \tag{6.31}$$

which corresponds to a false EDM of

$$d^{\text{false}}_{\text{translation}} \leq 1.9 \times 10^{-30}\ e\,\text{cm}. \tag{6.32}$$

6.5.3.2 Effect of cell motion in the presence of fixed external magnetic gradients

Cell motion within a fixed nonuniform field may produce a false EDM proportional to $(H_{yy})^3$ [107]. Possible sources include a fixed dipole near the cell, or any permanently magnetized component of the SQUID dewar or the MSR. Gradients from a source *on* the cell, like a magnetized o-ring, should not contribute because the source moves with the cell.

6.6 Geometric phase

The geometric phase is the phase accumulation of the spins as they diffuse in a combined magnetic field gradient and motional magnetic field ($\mathbf{E} \times \mathbf{v}/c^2$), and is a false EDM because it reverses with $\mathbf{E}$. It is a small effect with our experimental conditions. At room

temperature, using $\langle v_{\mathrm{He}} \rangle \approx 1575$ m/s and $\langle v_{\mathrm{Xe}} \rangle \approx 241$ m/s, the motional magnetic field $B_{\mathrm{He}}^{\mathrm{mot}} \approx 5$ nT and $B_{\mathrm{Xe}}^{\mathrm{mot}} \approx 0.8$ nT. Since $B_0 = 2.6$ μT, under the adiabatic approximation the spins remain aligned with B_0. The adiabatic condition can also be described as $\omega_0 \tau_{\mathrm{corr}} \gg 1$ where τ_{corr} is the time it takes for the spins to sample the cell and is on the order of seconds because $D_{\mathrm{He}} = 1.3$ cm^2/s and $D_{\mathrm{Xe}} = 0.2$ cm^2/s. Note that the mean free path $\lambda = 3D/v \approx 250$ nm for both ^{3}He and ^{129}Xe which means that the velocity changes directions on a time scale of $\lambda / \langle v \rangle \lesssim 1$ ns, randomizing the geometric phase accumulation between collisions.

Ref. [108] (Eq. 70) provides an estimation of the frequency shift in the diffusion approximation in 2D for cylindrical geometry, where $R \approx 1$ cm is the cell radius

$$\omega_{\mathrm{GP}} = \left(\frac{\gamma^2 R E G_{yy}}{2c^2 \omega_0^2} \right) \frac{4}{x_{1,1}^2 (x_{1,1}^4 - 1)} \frac{\omega_0^2}{1 + (\omega_0 R^2 / D x_{1,1}^2)^2}. \tag{6.33}$$

This is valid for nEDM cells considered in Ref. [108] that have a large radius-to-length ratio. We expect this to be an upper limit for our cylindrical cells where the length is proportional to the diameter and motion along the cell axis reduces radial diffusion. For ^{129}Xe and ^{3}He after scaling the diffusion constants for motion in 2D

$$\omega_{\mathrm{GP}}^{\mathrm{Xe}} = 8.0 \times 10^{-14} \text{ rad/s}, \quad \text{and} \quad \omega_{\mathrm{GP}}^{\mathrm{He}} = 3.4 \times 10^{-12} \text{ rad/s} \tag{6.34}$$

Combining the two to get the comagnetometer shift and false EDM,

$$\begin{aligned} \frac{1}{2\pi} \left| \omega_{\mathrm{GP}}^{\mathrm{false}} \right| &= 1.8 \times 10^{-13} \text{ Hz}, \\ d_{\mathrm{GP}}^{\mathrm{false}} &< 1.3 \times 10^{-31} \, e \, \mathrm{cm}. \end{aligned} \tag{6.35}$$

6.7 E uncertainty

An estimation of the uncertainty in the spatial average $\bar{E}$ in the presence of the safety electrode was performed by collaboration member Tianhao Liu using finite-element-analysis

software (COMSOL) and determined to be within 10%. The deviation δE couples to the EDM

$$d_{\delta E} \leq \frac{\delta E}{E} d_A(^{129}\text{Xe}) \tag{6.36}$$

determined using $d_A(^{129}\text{Xe})$ after unblinding which resulted in

$$d_{\delta E} \leq 2.5 \times 10^{-29}\, e\,\text{cm} \tag{6.37}$$

6.8 E^2 effects

The two cells used in HeXe2017 have different lengths, so different electric field strengths for the same applied HV. Therefore, we have data for $E = 0$, 2.75, and 3.24 kV/cm. The final E^2 false EDM was determined from the unblinded HV segment frequencies. The frequencies shown in Fig. 6.9 are the residuals from a 4$^{\text{th}}$ order polynomial fit of ω_i' of each run, totaling 539 values. The electric field per segment is determined from the average value of the HV recorded by the DAQ for the segment divided by the measurement cell length. The slope of the linear fit is

$$\frac{1}{2\pi}\frac{\partial \omega'}{\partial E^2} = 0.10 \pm 0.87 \frac{\text{nHz}}{(\text{kV/cm})^2} \tag{6.38}$$

The EDM correction is determined from the precision with which we reverse the HV, which was measured to to be ΔHV $\leq$ 10 V; therefore, $|E_+ - E_-| \leq 3.3$ V/cm and $|E_+^2 - E_-^2| \leq 0.02$ kV^2/cm^2. For the false EDM we have

$$\begin{gathered} \frac{1}{2\pi}\omega_{E^2}^{\text{false}} = \frac{1}{2\pi}\frac{\partial \omega'}{\partial E^2}|E_+^2 - E_-^2| \leq 0.017 \text{ nHz (68\% c.l.)}, \\ d_{E^2}^{\text{false}} \leq 1.2 \times 10^{-29}\, e\,\text{cm}. \end{gathered} \tag{6.39}$$

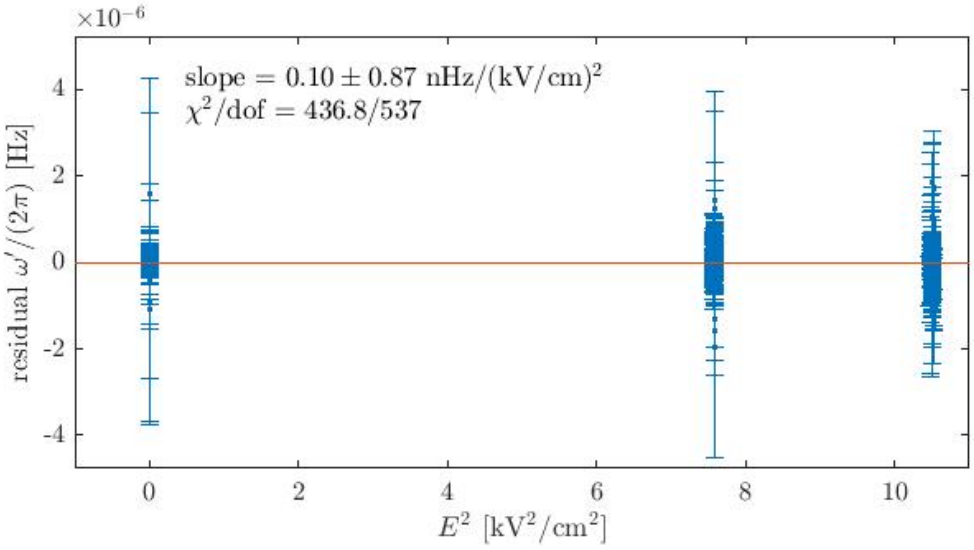

Figure 6.9: Residual frequencies from polynomial fits of ω_i' vs. averaged E^2 per segment.

6.9 Correlations

The consistency of the EDM measurements was checked under different conditions including gas pressure, measurement cell, HV ramp rate, HV segment length, HV polarity and $\hat{\mathbf{V}} \cdot \hat{\mathbf{B}}_\mathbf{0}$ at the start of a sequence of four, and $\hat{\mathbf{B}}_\mathbf{0}$ (See Fig. 6.10). Each of these couples to the systematic effects discussed previously. Varying gas pressure couples to the first and second term of Eq. 6.7 because of differences in the chemical shift and averaging of magnetic gradients within the cell. The two measurement cells used have different dimensions and therefore both the size and time structure (from different T_1) of the comagnetometer drift may change. For different HV ramp rates, the charging current will change. Correlations with HV segment length, HV polarity, and $\hat{\mathbf{V}} \cdot \hat{\mathbf{B}}_\mathbf{0}$ may indicate a systematic error from the comagnetometer drift correction. $\hat{\mathbf{B}}_\mathbf{0}$ couples to the earth's rotation and to the gradients from any nearby stationary dipole. The differences are shown in Table 6.5. No significant correlations were observed. The final systematic error for each of the effects discussed for the HeXe2017 analysis is provided in Table 6.6.

Source	a	b	$\frac{1}{2\pi}(\omega'_a - \omega'_b)$ (nHz)	**Coupling**
$\hat{\mathbf{B}}_\mathbf{0}$	$+$	$-$	-5.25 ± 6.71	Stationary dipole and the earth's rotation.
HV ramp	1 kV/sec	2 kV/sec	2.08 ± 11.41	Charging currents.
$\hat{\mathbf{V}}$	$+$	$-$	4.06 ± 6.80	Comagnetometer drift correction.
$\hat{\mathbf{V}} \cdot \hat{\mathbf{B}}_\mathbf{0}$	$+$	$-$	5.48 ± 6.84	Comagnetometer drift correction.
Segment length	400 sec	800 sec	-6.28 ± 6.76	Comagnetometer drift correction.
Cell	PP1	PP2	-0.81 ± 8.25	Magnetization of cell materials, comagnetometer drift, leakage currents, and cell motion.
Pressure	>0.9 bar	<0.7 bar	1.70 ± 7.86	Comagnetometer B_0 response and gradient sensitivity.

Table 6.5: Dependence of EDM frequencies on various parameters.

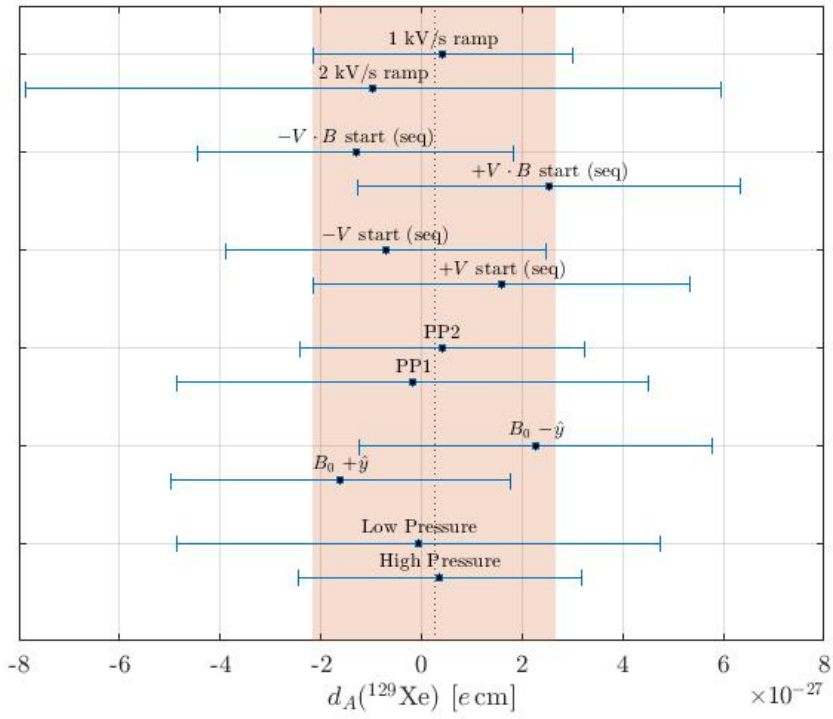

Figure 6.10: Weighted average of EDM measurements by parameter: pressure, cell, HV ramp rate, HV segment length, HV start polarity, $\hat{\mathbf{V}} \cdot \hat{\mathbf{B}}_\mathbf{0}$, and $\hat{\mathbf{B}}_\mathbf{0}$. The dotted line is the weighted average of all EDM measurements, $d_A(^{129}\mathrm{Xe})$, and the shaded region is σ_{d_A}.

Source	**Correction** (e **cm**)	**Sys. Error** (e **cm**)
Leakage current	0	1.2×10^{-28}
Charging currents	0	1.7×10^{-29}
Comagnetometer drift	-7.5×10^{-29}	6.7×10^{-28}
$\vec{E}$-correlated cell motion (rotation)	0	0.4×10^{-28}
$\vec{E}$-correlated cell motion (translation)	0	2.6×10^{-28}
E^2 effects	0	1.2×10^{-29}
E uncertainty	0	2.5×10^{-29}
Geometric phase	0	1.3×10^{-31}
Total	-7.5×10^{-29}	7.3×10^{-28}

Table 6.6: All false EDM sources discussed in the text and their associated systematic error.

CHAPTER VII

Conclusion

7.1 Results

After all systematic corrections and unblinding, for the weighted average of 120 EDM measurements, we find

$$d_A(^{129}\text{Xe}) = [0.25 \pm 2.32\ (\text{stat.}) \pm 0.73\ (\text{sys.})] \times 10^{-27}\ e\,\text{cm}, \tag{7.1}$$

which represents an upper limit of

$$d_A(^{129}\text{Xe}) \leq 4.8 \times 10^{-27}\ e\,\text{cm} \quad (95\%\ \text{c.l.}). \tag{7.2}$$

This result is a 40% improvement over the previous result by Rosenberry with one week of data compared to six months and includes an extensive study of systematic effects.

7.2 Future work

There is another EDM data set available from HeXe2018 with a (very preliminary) sensitivity at the $\sim 5 \times 10^{-28}$ level. In HeXe2018, with better gas purity and adjustments to the gas mixture, ^{3}He polarization was improved by a factor of 10 and ^{129}Xe polarization by a factor of two. A better leakage current measurement was completed, and leakage current

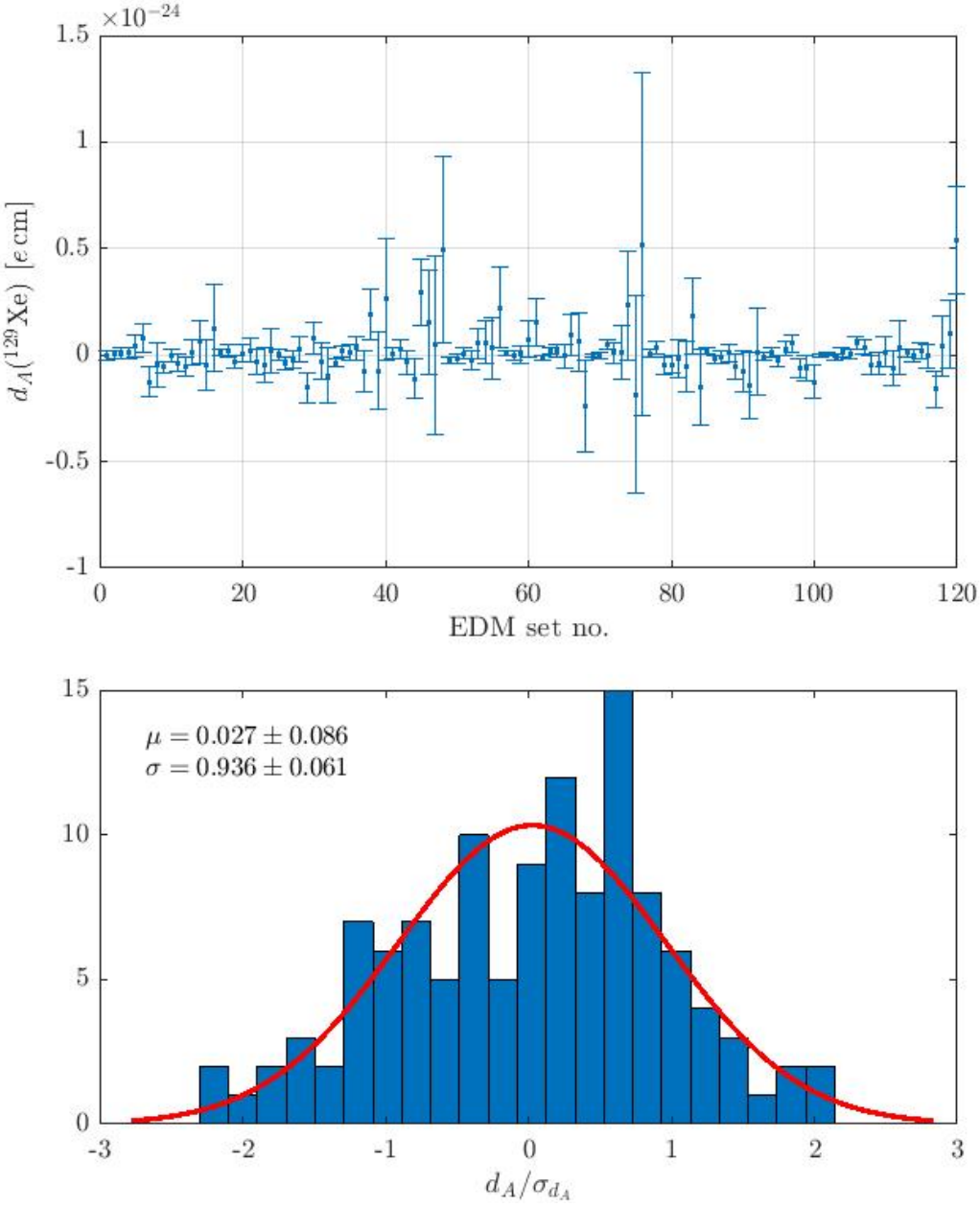

Figure 7.1: The final corrected and unblinded EDM measurements. $d_A(^{129}\mathrm{Xe})$ was determined from the weighted average of the 120 measurements.

to the grounded safety electrode was monitored during the measurements. Combined with the systematic analysis in this work and an additional cell-motion study, a new and more sensitive result is expected in the near future.

Other independent analysis methods are currently being investigated including using an in-phase and quadrature (IQ) method of phase extraction (discussed in Appendix A) and an alternative EDM extraction method using fitting of the phase data for each run.

Longer term HeXeEDM work includes investigation of cell shape to reduce comagnetometer drift following recent studies of ^{129}Xe–^{3}He comagnetometers [109], development of a flow-through gas system for automated cell filling and continuous running, bipolar HV, an upgraded dewar with lower SQUID noise, a larger electric field by increasing cell gas pressure, and higher precision $\pi/2$ pulses using improved external magnetometry. The BMSR-2 was also recently upgraded and now features a higher shielding factor.

With modest improvements in signal-to-noise, longer run-times enabled by an automated flow-through gas system, and reduction of comagnetometer drift, significant improvement in the statistical sensitivity is expected. The estimated statistical sensitivity (see Appendix A for a derivation) is

$$\sigma_d = C(\tau, T_2^*)\frac{h}{2E_0}\frac{\sqrt{24}}{2\pi\tau}\frac{1}{SNR} \tag{7.3}$$

where τ is the integration time which is the HV dwell time, $C(\tau, T_2^*) > 1$ is a coefficient taking into account the signal decay from T_2^*, and SNR is the dimensionless signal-to-noise ratio dependent on bandwidth and integration time. Assuming a 20% improvement in amplitudes over HeXe2018, $\tau = 800$ seconds, $E_0 = 5$ kV/cm, an improved SQUID sensitivity of 2 fT/$\sqrt{\text{Hz}}$, and T_2^* decays of $\sim 10,000$ seconds for each species, the estimated statistical sensitivity for 30 days of run-time with 50% efficiency is $\sigma_d \sim 2.5 \times 10^{-29}\, e\,$cm. However, the biggest limitation to the sensitivity is the comagnetometer drift. As the experiment signal-to-noise increases, the comagnetometer drift is apparent on shorter timescales

and the integration time must be decreased. In order to reach $\sim 10^{-29}\ e\,$cm sensitivity, significant reduction of the drift is necessary through optimization of cell shape and $\pi/2$ pulsing.

APPENDICES

APPENDIX A

Frequency resolution

This appendix provides a derivation of maximum frequency resolution (also referred to as the Cramer-Rao Lower Bound [35]) of two analysis methods: the in-phase and quadrature (IQ) method and the time-series analysis (block-fitting) which was the chosen analysis method for HeXe2017. In the IQ method, the in-phase and quadrature signals are used to obtain the phase as a function of time, and a linear fit of that phase provides the frequency. Below, we will first review the derivations of the maximum frequency resolution (assuming white phase noise) using the IQ method for frequency extraction in the case of a single-frequency signal with no decay and then a decaying single-frequency signal. In the second section we will do the same calculations for the block-fitting technique.

A.1 IQ method

A.1.1 Single frequency with no decay

The voltage signal observed from spin precession, $V(t)$ can be described as the following:

$$V(t) = V_0 \sin(\omega_0 t + \phi_0) + n(t), \tag{A.1}$$

where $n(t)$ is additive white voltage noise with power σ_V^2. The IQ procedure for determining the frequency is detailed below. First, we need to determine σ_ϕ as a function of σ_V. Then, we can determine σ_f from a linear fit of the phases. Starting with two orthogonal reference signals

$$V_{ref1} = \sin(\omega_{ref} t)$$
$$V_{ref2} = \cos(\omega_{ref} t),$$

we multiply the original signal by each reference signal

$$V_1 = V_0 \sin(\omega_0 t + \phi_0) \sin(\omega_{ref} t) + n(t) \cdot \sin(\omega_{ref} t)$$
$$V_2 = V_0 \sin(\omega_0 t + \phi_0) \cos(\omega_{ref} t) + n(t) \cdot \cos(\omega_{ref} t).$$

Here, the noise terms have power $\sigma_V^2/2$ and are uncorrelated. Rewriting the above,

$$V_1 = \frac{V_0}{2} \left[\cos((\omega_0 - \omega_{ref})t + \phi_0) - \cos((\omega_0 + \omega_{ref})t + \phi_0)\right]$$
$$V_2 = \frac{V_0}{2} \left[\sin((\omega_0 - \omega_{ref})t + \phi_0) + \sin((\omega_0 + \omega_{ref})t + \phi_0)\right],$$

we note that there is a low-frequency term and a high-frequency term. The high-frequency term is filtered out with a low-pass filter for the in-phase and quadrature signals. Defining $\omega \equiv \omega_0 - \omega_{ref}$ we have $\phi(t) \equiv \omega t + \phi_0$, which is discretized as shown below with $t^i = \frac{\tau}{N} i$

$$\phi^i = \phi_0 + \omega t^i. \tag{A.2}$$

Finally,

$$V_I^i = \frac{V_0^i}{2} \cos\phi^i \quad V_Q^i = \frac{V_0^i}{2} \sin\phi^i \quad \phi^i = \arctan\frac{V_Q^i}{V_I^i}. \tag{A.3}$$

Now we can determine the errors (dropping the index for the moment):

$$\begin{aligned}
\sigma_\phi^2 &= \left(\frac{V_I}{V_Q^2+V_I^2}\right)^2 \sigma_{V_Q}^2 + \left(\frac{-V_Q}{V_Q^2+V_I^2}\right)^2 \sigma_{V_I}^2 \\
\sigma_\phi^2 &= \left(\frac{V_I}{V_Q^2+V_I^2}\right)^2 \frac{\sigma_V^2}{2} + \left(\frac{-V_Q}{V_Q^2+V_I^2}\right)^2 \frac{\sigma_V^2}{2} \\
&= \frac{\sigma_V^2}{2}\left[\left(\frac{\cos\phi}{V_0/2}\right)^2 + \left(\frac{\sin\phi}{V_0/2}\right)^2\right] \\
&= \frac{\sigma_V^2}{2}\left(\frac{2}{V_0}\right)^2 \\
&= \frac{2\sigma_V^2}{V_0^2}
\end{aligned}$$

We find that the uncertainty per point for phase and voltage are related by

$$\sigma_\phi^i = \frac{\sqrt{2}\sigma_V^i}{V_0^i} \tag{A.4}$$

Aside:

The following is from Bevington [103] Chapter 6. For a linear function

$$y(x) = a + bx,$$

the uncertainty in b after a least-squares fit is

$$\sigma_b^2 = \frac{1}{\Delta}\sum \frac{1}{\sigma_i^2}$$

where

$$\Delta = \begin{vmatrix} \sum \frac{1}{\sigma_i^2} & \sum \frac{x_i}{\sigma_i^2} \\ \sum \frac{x_i}{\sigma_i^2} & \sum \frac{x_i^2}{\sigma_i^2} \end{vmatrix} = \sum \frac{1}{\sigma_i^2} \sum \frac{x_i^2}{\sigma_i^2} - \left(\sum \frac{x_i}{\sigma_i^2}\right)^2.$$

We can obtain ω from a linear fit of the phase

$$\sigma_\omega^2 = \frac{1}{\Delta}\sum_{i=1}^{N}\frac{1}{\sigma_{\phi^i}^2} = \frac{1}{\Delta}\sum_{i=1}^{N}\frac{V_0^2}{2\sigma_V^2} = \frac{1}{\Delta}N\frac{V_0^2}{2\sigma_V^2} \tag{A.5}$$

where

$$\begin{aligned}
\Delta &= \sum\frac{1}{\sigma_i^2}\sum\frac{t_i^2}{\sigma_i^2} - \left(\sum\frac{t_i}{\sigma_i^2}\right)^2 \\
&= \left(\frac{\tau}{N}\right)^2\left(\frac{V_0^2}{2\sigma_V^2}\right)^2\left(N\sum_{i=1}^{N}i^2 - \left(\sum_{i=1}^{N}i\right)^2\right) \\
&= \left(\frac{\tau}{N}\right)^2\left(\frac{V_0^2}{2\sigma_V^2}\right)^2\left(\frac{1}{12}N^2(N^2-1)\right) \\
&= (\tau)^2\left(\frac{V_0^2}{2\sigma_V^2}\right)^2\left(\frac{1}{12}(N^2-1)\right) \\
&\approx \frac{\tau^2}{12}\left(N\frac{V_0^2}{2\sigma_V^2}\right)^2.
\end{aligned} \tag{A.6}$$

Finally,

$$\boxed{\sigma_f = \frac{\sqrt{24}}{2\pi\tau}\,\frac{\sigma_V/\sqrt{N}}{V_0} = \frac{\sqrt{24}}{2\pi\tau}\frac{1}{SNR}}. \tag{A.7}$$

A.1.2 Single frequency with exponential decay

With exponential decay our signal is

$$V(t) = V_0\, e^{-t/T_2}\ \sin(\omega_{\text{ref}}t + \phi(t)). \tag{A.8}$$

The calculation is the same, but now we replace V_0^i with $V_0'^i = V_0\, e^{-t^i/T_2}$.

$$\begin{aligned}
\sigma_\omega^2 &= \frac{1}{\Delta}\sum_{i=1}^{N}\frac{1}{\sigma_{\phi^i}^2} = \frac{1}{\Delta}\sum_{i=1}^{N}\frac{(V_0'^i)^2}{2\sigma_V^2} \\
&= \frac{1}{\Delta}\frac{V_0^2}{2\sigma_V^2}\sum_{i=1}^{N} e^{-\left(\frac{2\tau}{NT_2}\right)i} = \frac{1}{\Delta}\frac{V_0^2}{2\sigma_V^2}\sum_{i=1}^{N}\left(\underbrace{e^{-\frac{2\tau}{NT_2}}}_{\beta}\right)^i \\
&= \frac{1}{\Delta}\frac{V_0^2}{2\sigma_V^2}\sum_{i=1}^{N}\beta^i = \frac{1}{\Delta}\frac{V_0^2}{\sigma_V^2}\left[\frac{\beta}{\beta-1}\left(\beta^N-1\right)\right] \\
&= \frac{1}{\Delta}\frac{V_0^2}{2\sigma_V^2}\left[\frac{1}{1-e^{\frac{2\tau}{NT_2}}}\left(e^{-\frac{2\tau}{T_2}}-1\right)\right]
\end{aligned}$$

Using, for small x, $\frac{1}{1-e^x} \approx -\frac{1}{x}$,

$$\sigma_\omega^2 = \frac{1}{\Delta}N\frac{V_0^2}{2\sigma_V^2}\underbrace{\left(\frac{T_2}{\tau}\frac{1-e^{-\frac{2\tau}{T_2}}}{2}\right)}_{\text{This term}\to 1 \text{ as } T_2\to\infty}$$

Next,

$$\begin{aligned}
\Delta &= \sum\frac{1}{\sigma_i^2}\sum\frac{t_i^2}{\sigma_i^2} - \left(\sum\frac{t_i}{\sigma_i^2}\right)^2 \\
&= \left(\frac{V_0^2}{2\sigma_V^2}\right)^2\left(\frac{\tau}{N}\right)^2\left[\sum\beta^i\sum i^2\beta^i - \left(\sum i\beta^i\right)^2\right]
\end{aligned}$$

The leading term is:

$$\begin{aligned}
\Delta &\approx \left(\frac{V_0^2}{2\sigma_V^2}\right)^2\left(\frac{\tau}{N}\right)^2\frac{N^4T_2^2}{16\tau^4}\left[e^{-\frac{4\tau}{T_2}}\left(-4\tau^2e^{\frac{2\tau}{T_2}} - 2T_2^2e^{\frac{2\tau}{T_2}} + T_2^2e^{\frac{4\tau}{T_2}} + T_2^2\right)\right] \\
&= \left(N\frac{V_0^2}{2\sigma_V^2}\right)^2 \underbrace{\frac{T_2^4}{16\tau^2}\left[1-\left(4\frac{\tau^2}{T_2^2}+2\right)e^{\frac{-2\tau}{T_2}} + e^{\frac{-4\tau}{T_2}}\right]}_{\text{This does, in fact, reduce to } \tau^2/12 \text{ as expected in the limit that } T_2\to\infty}
\end{aligned} \tag{A.9}$$

If $\tau = T_2$ this simplifies to

$$= \left(N\frac{V_0^2}{2\sigma_V^2}\right)^2 \frac{\tau^2}{16}\left[1 - 6e^{-2} + e^{-4}\right]$$

Finally, we have

$$\sigma_\omega^2 = \frac{2\sigma_V^2}{V_0^2 N}\frac{12\tau}{T_2^3}\left(\frac{2}{3}\cdot\frac{1-e^{-\frac{2\tau}{T_2}}}{1-\left(4\frac{\tau^2}{T_2^2}+2\right)e^{\frac{-2\tau}{T_2}}+e^{\frac{-4\tau}{T_2}}}\right)$$

$$\sigma_f = \underbrace{\sqrt{\frac{2}{3}\cdot\frac{1-e^{-\frac{2\tau}{T_2}}}{1-\left(4\frac{\tau^2}{T_2^2}+2\right)e^{\frac{-2\tau}{T_2}}+e^{\frac{-4\tau}{T_2}}}}}_{\text{numerical factor}}\cdot\frac{1}{2\pi}\sqrt{\frac{12\tau}{T_2^3}}\frac{\sqrt{2}\sigma_V/\sqrt{N}}{V_0}. \tag{A.10}$$

For $\tau = T_2$,

$$\sigma_f = \left(\sqrt{\frac{2}{3}\cdot\frac{1-e^{-2}}{1-6e^{-2}+e^{-4}}}\right)\frac{\sqrt{12}}{2\pi\tau}\frac{\sqrt{2}\sigma_V/\sqrt{N}}{V_0}$$

$$\boxed{\sigma_f \approx (1.7)\frac{\sqrt{24}}{2\pi\tau}\frac{\sigma_V/\sqrt{N}}{V_0} = (1.7)\frac{\sqrt{24}}{2\pi\tau}\frac{1}{SNR}}. \tag{A.11}$$

A.2 Block-fitting method

For the block-fitting method, the measurement time τ is split up so that

$$\tau = n\tau_0$$

where n is the number of blocks and τ_0 is the block size. Each block is fitted separately using the separable nonlinear least-squares method detailed below to determine a phase and amplitude for each block.

Separable nonlinear least-squares: The variable projection method

The following is an overview of the method described in Ref. [104], Section 2.[a]

Given a set of observations y_i the residuals for a model that is a linear combination of nonlinear functions can be written as

$$r_i(\mathbf{a}, \boldsymbol{\alpha}) = y_i - \sum_{j=1}^{n} a_j \pi_j(\boldsymbol{\alpha}; t_i).$$

Here, $\mathbf{a}$ and $\boldsymbol{\alpha}$ describe the linear and nonlinear parameters to be determined. The functional to be minimized is

$$\|\mathbf{r}(\mathbf{a}, \boldsymbol{\alpha})\|_2^2 = \|\mathbf{y} - \boldsymbol{\Pi}(\boldsymbol{\alpha})\mathbf{a}\|_2^2$$

where $\boldsymbol{\Pi}(\boldsymbol{\alpha})$ is a matrix composed of the nonlinear functions $\pi_j(\boldsymbol{\alpha}; t_i)$ evaluated at all t_i-values. If the nonlinear parameters α_k are known, the linear parameters can be determined by solving the linear least-squares problem

$$\mathbf{a} = \boldsymbol{\Pi}(\boldsymbol{\alpha})^{+}\mathbf{y}$$

where $\boldsymbol{\Pi}(\boldsymbol{\alpha})^{+}$ is the Moore-Penrose generalized inverse of $\boldsymbol{\Pi}(\boldsymbol{\alpha})$. Replacing $\mathbf{a}$ in this form in the original functional, the minimization problem becomes

$$\min_{\boldsymbol{\alpha}} \frac{1}{2} \left\| \left(\mathbf{I} - \boldsymbol{\Pi}(\boldsymbol{\alpha})\boldsymbol{\Pi}(\boldsymbol{\alpha})^{+} \right) \mathbf{y} \right\|_2^2.$$

In the above form of the functional, the linear parameters have been eliminated so we can define

$$\mathbf{r}_2(\boldsymbol{\alpha}) = \left(\mathbf{I} - \boldsymbol{\Pi}(\boldsymbol{\alpha})\boldsymbol{\Pi}(\boldsymbol{\alpha})^{+} \right) \mathbf{y}$$

which is called the variable projection (VP) of $\mathbf{y}$. The functional $\frac{1}{2}\|\mathbf{r}_2(\boldsymbol{\alpha})\|_2^2$ is the VP functional.

The VP method requires first minimization of the VP functional to obtain the optimal values for the nonlinear parameters α_k which are used to obtain the linear least-squares problem $\mathbf{a} = \boldsymbol{\Pi}(\boldsymbol{\alpha})^+\mathbf{y}$. This is then solved to obtain the linear parameters a_j.

[a] I've slightly changed the notation, using π/Π instead of ϕ/Φ to avoid confusion later in the text since I use ϕ and Φ for phases.

A.2.1 Single frequency with no decay

Suppose we are starting with a voltage signal that can be described as

$$V(t) = V_0 \sin \Phi(t) \tag{A.12}$$

where

$$\Phi(t) = \omega_0 t + \phi(t). \tag{A.13}$$

A.2.1.1 Method description

First, we will divide up the voltage signal into blocks of length τ_0. There are $N = f_s \cdot \tau$ total points in the data set and n blocks of length τ_0. We will use the index m for blocks and i or j for points. Each block has N_b points, where $N_b = f_s \cdot \tau_0$. For simplicity, we'll set $t_0 = t_{i=1} = 0$.

The resulting data to be analyzed can be written in the form

$$V^m(t) = V_0^m \sin \Phi^m(t) \tag{A.14}$$

where $t = [0, \tau_0]$. The same time interval is used for each block of voltage data. This choice will become clear later. The goal is to determine V_0^m and Φ^m for each block. Next,

we do a separable nonlinear least-squares fit, where the fit function is

$$f(t) = A\sin(\omega t) + B\cos(\omega t). \tag{A.15}$$

The fitted parameters are the linear parameters A^m, B^m and the nonlinear parameter ω^m.

As shown in the previous section, this can also be written as

$$f(t) = V_0 \sin(\omega t + \phi) \tag{A.16}$$

defining V as the amplitude and ϕ as the phase at $t = 0$. Therefore, from the fitted parameters we can obtain V_0^m and ϕ^m. Note that, because of the way we have defined the time interval of the fit, the latter is the phase at the beginning of the block. To determine the accumulated phase $\Phi(t)$, where here $t = 0, \tau_0, \ldots, (n-1)\tau_0$, we use the following

$$\Phi^m = \phi^m + \left\{\Phi^{m-1} + \omega^{m-1}\tau_0 - \left(\Phi^{m-1} + \omega^{m-1}\tau_0\right) \bmod (2\pi)\right\} \tag{A.17}$$

where the term in brackets is simply the number of cycles until the current block. Note that this is a slightly different definition for Φ than previously used in Eq. A.14. Previously, $\Phi(t)$ denoted time-evolution of the phase *within* a block, but from now on we will use it only for time-evolution from block-to-block. Any time-evolution within a block will be made explicit (i.e. using ωt).

A.2.1.2 Error determination: Part 1

Now, we will discuss the errors of V_0^m and Φ^m. We will begin by determining the error of the fitted parameters A^m, B^m and ω^m from the separable nonlinear least-squares fit. Recall that the data for each block is

$$V_i^m = V_0^m \sin\left(\Phi^m + \omega_0^m t_i\right) \tag{A.18}$$

with $t_i = \frac{\tau}{N} i = \frac{\tau_0}{N_b} i$. Dropping the block index and using the notation in the above overview of VP method, the linear parameters $\mathbf{a} = (A, B)$ and nonlinear $\boldsymbol{\alpha} = \omega$. We have

$$r_i = V_i - \sum_{k=1}^{2} a_k \pi_k(\omega, t_i)$$

where $\pi_1(t) = \sin(\omega t)$ and $\pi_2(t) = \cos(\omega t)$ evaluated at points t_i for $i = 1, 2, \ldots, N_b$ compose the columns of matrix $\Pi(\omega)$. The VP of $\mathbf{V}$ is

$$\mathbf{r}^{VP}(\omega) = \left(\mathbf{I} - \mathbf{\Pi}(\omega)\mathbf{\Pi}(\omega)^{+}\right)\mathbf{V}$$

or

$$r_i^{VP} = \sum_{j}^{N_b} \left(\delta_{ij} - \sum_{k}^{2} \pi(\omega)_{ik} \pi(\omega)^{+}_{kj} \right) V_j.$$

For the first part of the VP method, the nonlinear minimization problem, the χ^2 to be minimized is

$$\chi^2_{\text{nlin}} = \sum_{i}^{N_b} \left[\frac{1}{\sigma_i} \sum_{j}^{N_b} \left(\delta_{ij} - \sum_{k}^{2} \pi(\omega)_{ik} \pi(\omega)^{+}_{kj} \right) V_j \right]^2 \tag{A.19}$$

where σ_i is the voltage error per point σ_V.

If $\mathbf{\Pi}(\omega) = (\sin \omega t, \cos \omega t)$, then a suitable pseudoinverse is $\mathbf{\Pi}^{+}(\omega) = \frac{1}{2}(\csc \omega t, \sec \omega t)^T$. After the optimum value for ω has been determined, which we'll denote as $\hat{\omega}$, we can then solve the linear problem,

$$\begin{pmatrix} A \\ B \end{pmatrix} = \frac{1}{2} \begin{pmatrix} \csc \hat{\omega} t \\ \sec \hat{\omega} t \end{pmatrix} \mathbf{V}. \tag{A.20}$$

Aside:

The following is from Bevington [103] Chapter 7. For a function that is linear in its parameter a_k:

$$y(x) = \sum_{k=1}^{m} a_k f_k(x)$$

Then, using

$$\Delta = \begin{vmatrix} \sum \frac{f_1(x_i)f_1(x_i)}{\sigma_i^2} & \sum \frac{f_1(x_i)f_2(x_i)}{\sigma_i^2} & \cdots \\ \sum \frac{f_2(x_i)f_1(x_i)}{\sigma_i^2} & \sum \frac{f_2(x_i)f_2(x_i)}{\sigma_i^2} & \cdots \\ \vdots & \vdots & \ddots \end{vmatrix},$$

we can determine the parameters

$$a_1 = \frac{1}{\Delta}\begin{vmatrix} \sum y_i \frac{f_1(x_i)}{\sigma_i^2} & \sum \frac{f_1(x_i)f_2(x_i)}{\sigma_i^2} & \cdots \\ \sum y_i \frac{f_2(x_i)}{\sigma_i^2} & \sum \frac{f_2(x_i)f_2(x_i)}{\sigma_i^2} & \cdots \\ \vdots & \vdots & \ddots \end{vmatrix}, \; a_2 = \frac{1}{\Delta}\begin{vmatrix} \sum \frac{f_1(x_i)f_1(x_i)}{\sigma_i^2} & \sum y_i \frac{f_1(x_i)}{\sigma_i^2} & \cdots \\ \sum \frac{f_2(x_i)f_1(x_i)}{\sigma_i^2} & \sum y_i \frac{f_2(x_i)}{\sigma_i^2} & \cdots \\ \vdots & \vdots & \ddots \end{vmatrix}, \cdots$$

Then, from the symmetric matrix

$$\alpha_{lk} \equiv \sum \left[\frac{1}{\sigma_i^2} f_l(x_i) f_k(x_i) \right]$$

we can determine the covariance matrix $\boldsymbol{\sigma}^2 = \boldsymbol{\alpha}^{-1}$, where the diagonal elements provide the errors $\sigma_{a_k}^2$.

Let's calculate Δ, parameters A and B, and the symmetric matrix $\boldsymbol{\alpha}$. We are assuming

$\omega_0 \approx \hat{\omega} \equiv \omega$. First, with $t_i = \frac{\tau_0}{N_b}\, i$:

$$\begin{aligned}
\Delta &= \sum_{i=1}^{N_b} \frac{1}{\sigma_i^2} \sin^2(\omega t_i) \sum_{i=1}^{N_b} \frac{1}{\sigma_i^2} \cos^2(\omega t_i) - \left(\sum_{i=1}^{N_b} \frac{1}{\sigma_i^2} \sin(\omega t_i) \cos(\omega t_i) \right)^2 \\
&= \left(\frac{1}{\sigma_V^2} \right)^2 \left[\sum_{i=1}^{N_b} \sin^2(\omega t_i) \sum_{i=1}^{N_b} \cos^2(\omega t_i) - \left(\sum_{i=1}^{N_b} \sin(\omega t_i) \cos(\omega t_i) \right)^2 \right] \\
&= \left(\frac{1}{\sigma_V^2} \right)^2 \frac{1}{4} \left(N_b^2 - \csc^2(\frac{\omega \tau_0}{N_b}) \sin^2(\omega \tau_0) \right) \\
&\approx \left(\frac{1}{\sigma_V^2} \right)^2 \frac{N_b^2}{4} \left\{ 1 - \frac{\sin^2 \omega \tau_0}{\omega \tau_0} \right\}
\end{aligned}$$

Since $\sin^2 x / x^2$ is strongly peaked at $x = 0$ and $\omega \tau_0$ is not likely to be small, we can neglect the second term in brackets.

$$\approx \left(\frac{1}{\sigma_V^2} \right)^2 \frac{N_b^2}{4}$$

Next,

$$\begin{aligned}
A &= \frac{1}{\Delta} \left[\sum_{i=1}^{N_b} \frac{V_i}{\sigma_i^2} \sin(\omega t_i) \sum_{i=1}^{N_b} \frac{1}{\sigma_i^2} \cos^2(\omega t_i) - \sum_{i=1}^{N_b} \frac{V_i}{\sigma_i^2} \cos(\omega t_i) \sum_{i=1}^{N_b} \frac{1}{\sigma_i^2} \sin(\omega t_i) \cos(\omega t_i) \right] \\
&= \frac{1}{\Delta} \left(\frac{V_0}{\sigma_V^4} \right) \left[\sum_{i=1}^{N_b} \sin(\omega t_i + \Phi) \sin(\omega t_i) \sum_{i=1}^{N_b} \cos^2(\omega t_i) \quad \ldots \right. \\
&\qquad \left. - \sum_{i=1}^{N_b} \sin(\omega t_i + \Phi) \cos(\omega t_i) \sum_{i=1}^{N_b} \sin(\omega t_i) \cos(\omega t_i) \right] \\
&= \frac{1}{\Delta} \left(\frac{V_0}{\sigma_V^4} \right) \left[-\frac{1}{8} \cos \Phi \left(N_b^2 \cos \left(\frac{2\omega \tau_0}{N_b} \right) - N_b^2 - \cos(2\omega \tau_0) + 1 \right) \csc^2 \left(\frac{\tau_0 \omega}{N_b} \right) \right] \\
&\approx \frac{1}{\Delta} \left(\frac{V_0}{\sigma_V^4} \right) N_b^2 \cos \Phi \left(\frac{2\omega^2 \tau_0^2 + \cos(2\omega \tau_0) - 1}{8\omega^2 \tau_0^2} \right) \approx \frac{1}{\Delta} \left(\frac{V_0}{\sigma_V^2} \right) N_b^2 \cos \Phi \left(\frac{1}{4} \right) \\
&= \left(\sigma_V^2 \right)^2 \frac{4}{N_b^2} \left(\frac{V_0}{\sigma_V^4} \right) \frac{N_b^2}{4} \cos \Phi \\
&= V_0 \cos \Phi
\end{aligned}$$

Similarly, we find $B = V_0 \sin\Phi$. We can now determine $\boldsymbol{\alpha}$

$$\alpha_{jk} = \sum_i \frac{1}{\sigma_i^2} \hat{\pi}_j(t_i)\hat{\pi}_k(t_i)$$

Using $\hat{\omega}t_i = \hat{\omega}\frac{\tau_0}{N_b}i \equiv \xi i$

$$\begin{aligned}\boldsymbol{\alpha} &= \frac{1}{\sigma_V^2}\begin{bmatrix} \sum \sin^2 \xi i & \sum \sin \xi i \cos \xi i \\ \sum \sin \xi i \cos \xi i & \sum \cos^2 \xi i \end{bmatrix} \\ &\approx \frac{1}{2}\frac{N_b}{\sigma_V^2}\begin{bmatrix} 1 & 0 \\ 0 & 1 \end{bmatrix}\end{aligned}$$

which gives us

$$\sigma_A^2 = \sigma_B^2 = \frac{2\sigma_V^2}{N_b} \tag{A.21}$$

Noting that $\sigma_\phi = \sigma_\Phi$ we can obtain an expression for the phase error

$$\begin{aligned}\sigma_\Phi^2 &= \left(\frac{B}{A^2+B^2}\right)^2 \sigma_A^2 + \left(\frac{A}{A^2+B^2}\right)^2 \sigma_B^2 \\ &= \frac{2\sigma_V^2}{N_b}\left(\frac{1}{A^2+B^2}\right) \\ &= \frac{2\sigma_V^2}{N_b}\left(\frac{1}{V_0^2}\right)\end{aligned}$$

Finally we have

$$\boxed{\sigma_\Phi = \sqrt{2}\left(\frac{\sigma_V/\sqrt{N_b}}{V_0}\right)} = \sqrt{2n}\left(\frac{\sigma_V/\sqrt{N}}{V_0}\right) \tag{A.22}$$

To get the frequency from the previously determined $\Phi(t)$, where $t = 0, \tau_0, 2\tau_0, \ldots (n-1)\tau_0$, we again use a linear fit to obtain the same result as the IQ method,

$$\sigma_\omega^2 = \frac{1}{\Delta}\sum_{i=0}^{n-1}\frac{1}{\sigma_{\Phi^i}^2} = \frac{1}{\Delta}\sum_{i=0}^{n-1}\frac{V_0^2 N_b}{2\sigma_V^2} = \frac{1}{\Delta}nN_b\frac{V_0^2}{2\sigma_V^2} = \frac{1}{\Delta}N\frac{V_0^2}{2\sigma_V^2} \tag{A.23}$$

where we used $N = nN_b$.

$$\begin{aligned}
\Delta &= \sum \frac{1}{\sigma_i^2} \sum \frac{t_i^2}{\sigma_i^2} - \left(\sum \frac{t_i}{\sigma_i^2} \right)^2 \\
&= \left(\frac{V_0^2}{\sigma_V^2} \frac{N_b}{2} \right)^2 \frac{\tau^2}{n^2} \left(n \sum_{i=0}^{n-1} i^2 - \left(\sum_{i=0}^{n-1} i \right)^2 \right) \\
&= \left(\frac{V_0^2}{\sigma_V^2} \frac{N_b}{2} \right)^2 \tau^2 \left(\frac{1}{12}(n^2 - 1) \right) \\
&\approx \frac{\tau^2}{12} \left(\frac{V_0^2}{\sigma_V^2} \frac{N}{2} \right)^2 .
\end{aligned}$$

Finally,

$$\boxed{\sigma_f = \frac{\sqrt{24}}{2\pi\tau} \frac{\sigma_V/\sqrt{N}}{V_0}.} \tag{A.24}$$

A.3 Comparison with simulated data

To confirm the estimations of the Cramer-Rao Lower Bound (CRLB) from Eqs. A.7,A.10, and A.24, we compared the results of frequency extraction using both the block-fitting method and the IQ method using simulated data. The datasets were generated as sinusoidal signals with additive white gaussian noise. We compare the results of simulated data with and without decay for one and two frequency signals. Then, for two frequency signals we added common-mode frequency drift, similar to a B_0 drift. Each dataset of a given type (e.g. single frequency with decay) has the same signal with different white noise. Note that the IQ method errors are underestimated because the signals are filtered and the autocorrelation was not accounted for when determining error bars from the linear phase fits.

We find that the calculated frequency resolution using Eq. A.10 and the frequency errors using the block-fitting method are in good agreement.

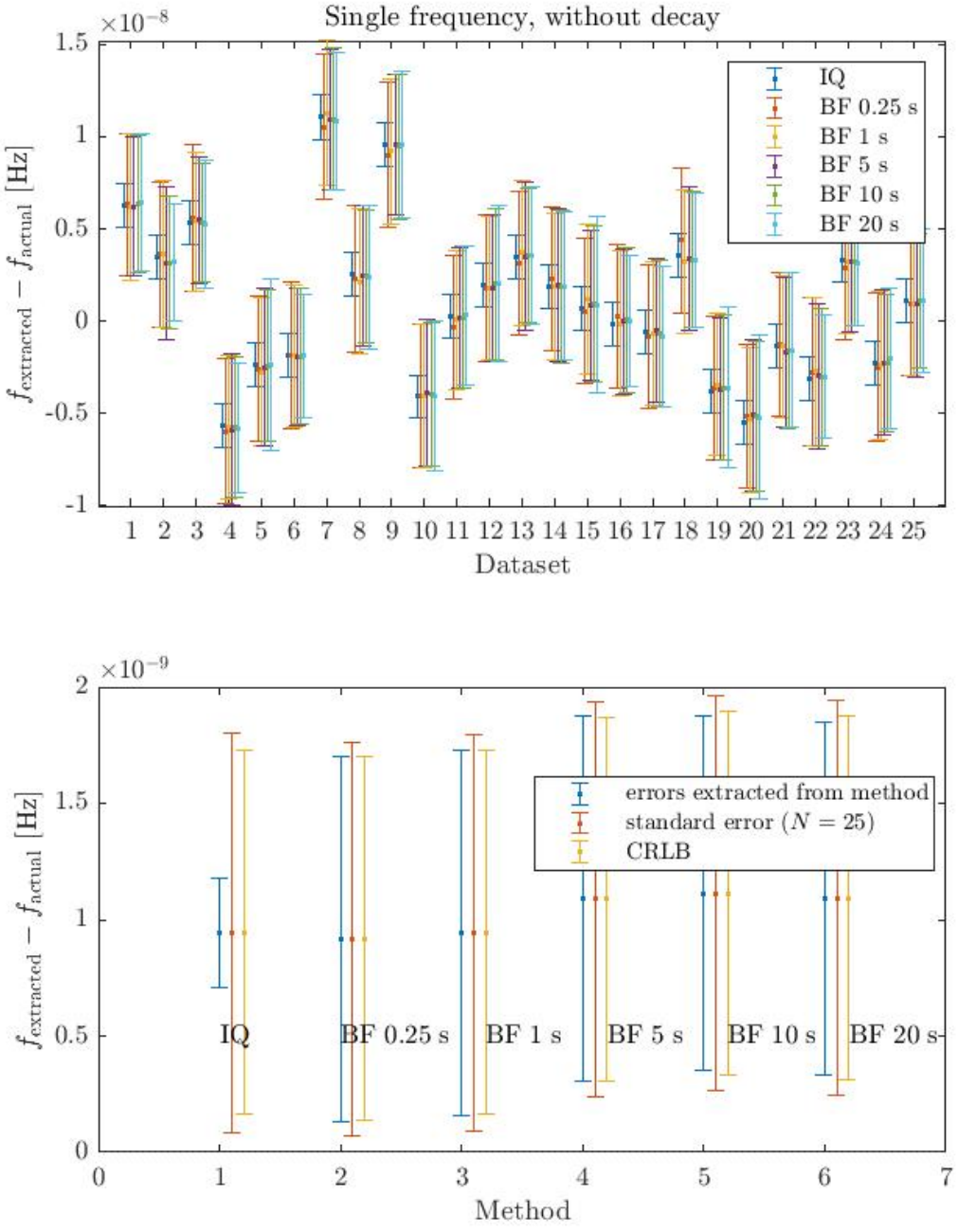

Figure A.1: The extracted frequencies from the IQ method and for varying block-lengths using the block-fitting method for single-frequency data without signal decay.

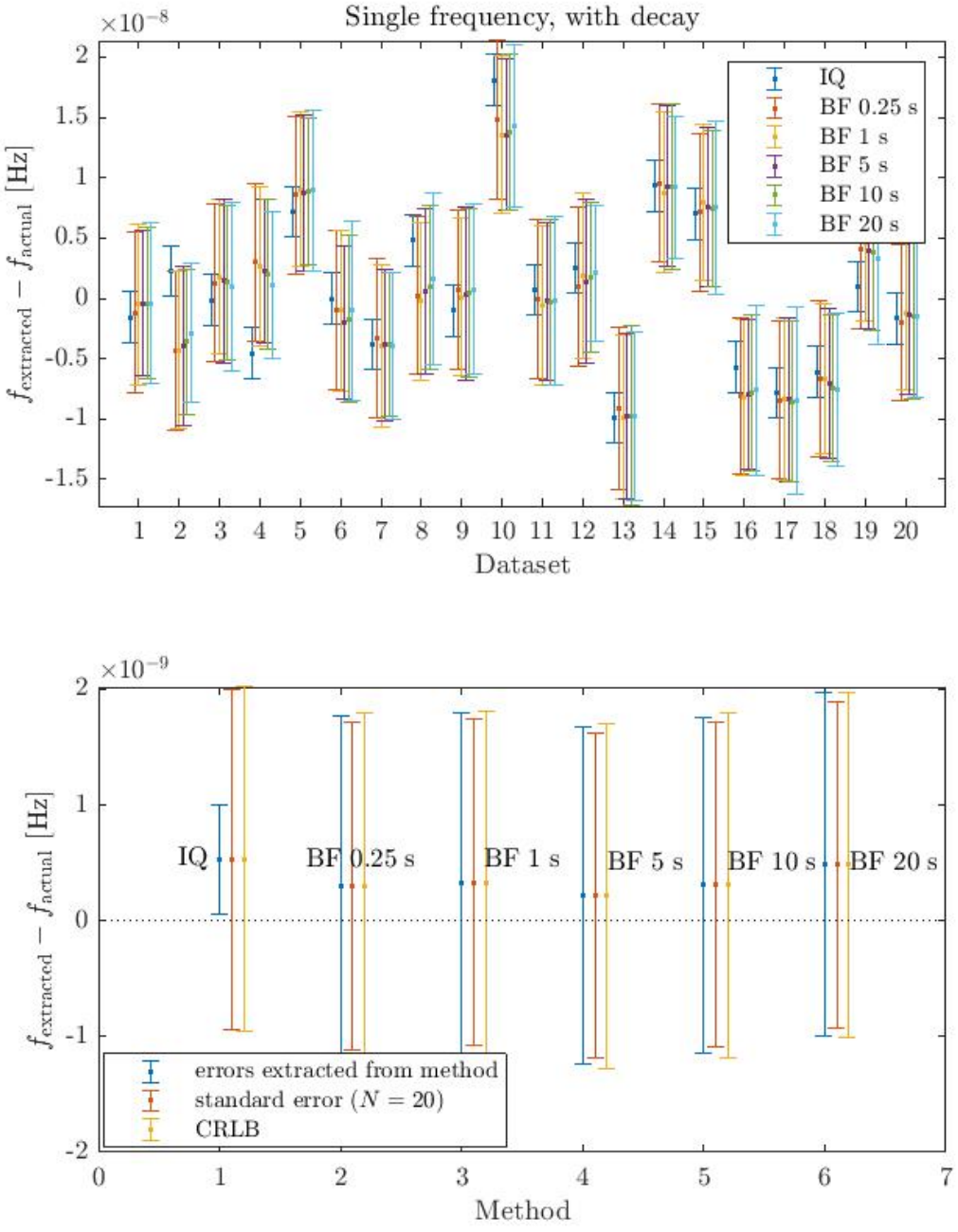

Figure A.2: The extracted frequencies from the IQ method and for varying block-lengths using the block-fitting method for single-frequency data with signal decay.

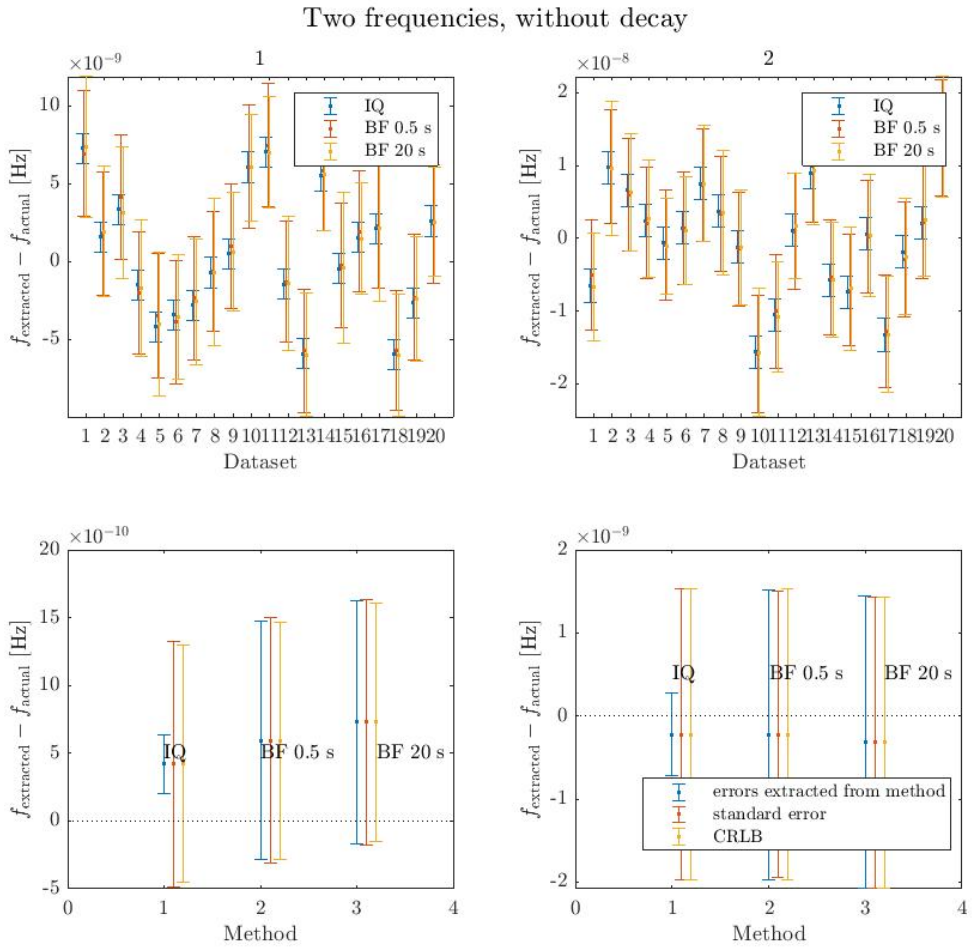

Figure A.3: The extracted frequencies from the IQ method and for varying block-lengths using the block-fitting method for two-frequency data without signal decay.

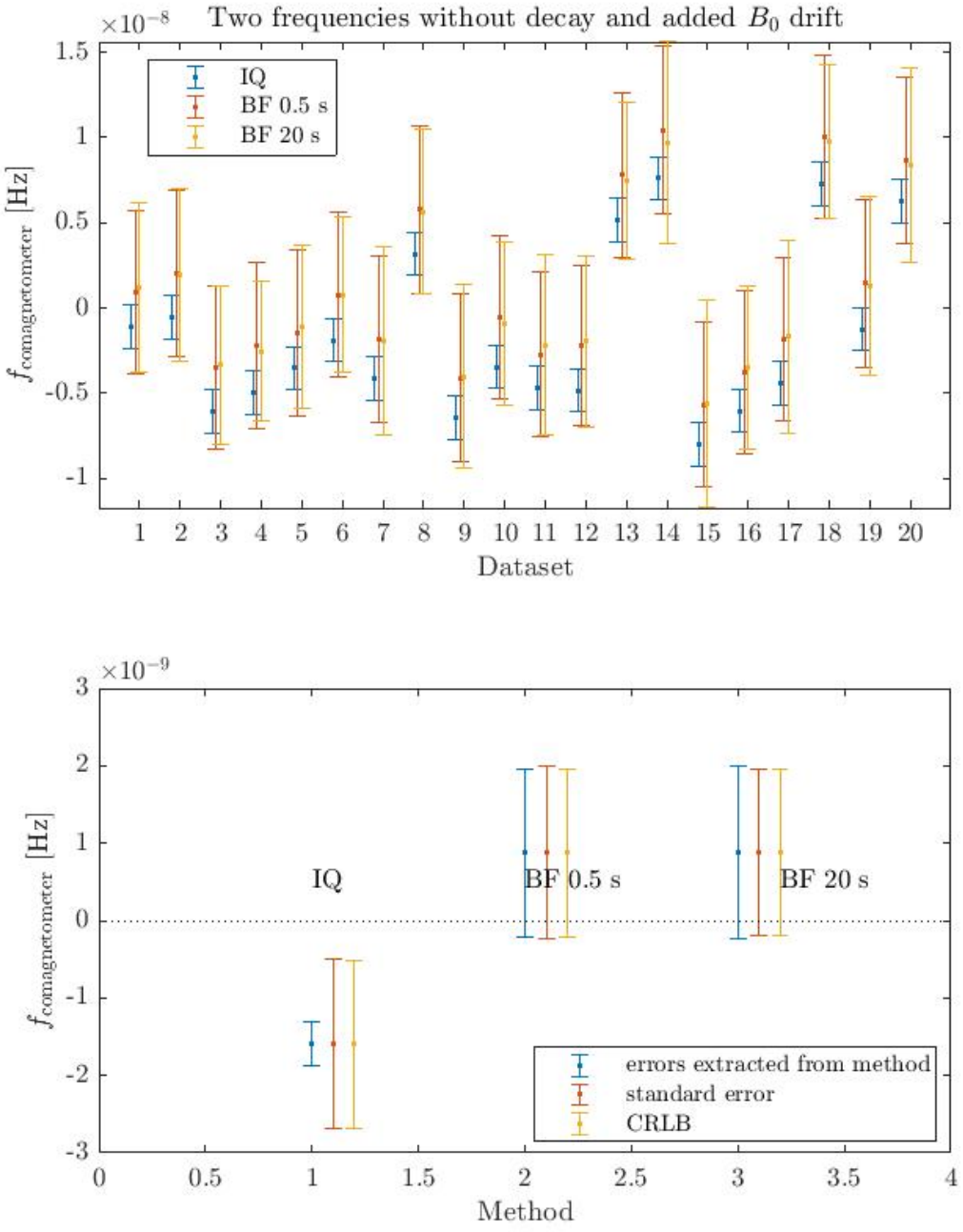

Figure A.4: The extracted frequencies from the IQ method and for varying block-lengths using the block-fitting method for two-frequency data without signal decay but with an added "B_0" drift. The second added frequency was $f_2 = rf_1$. After extracting individual frequencies they were "comagnetometer-corrected" $f_{\text{comagnetometer}} = f_1 - rf_2$.

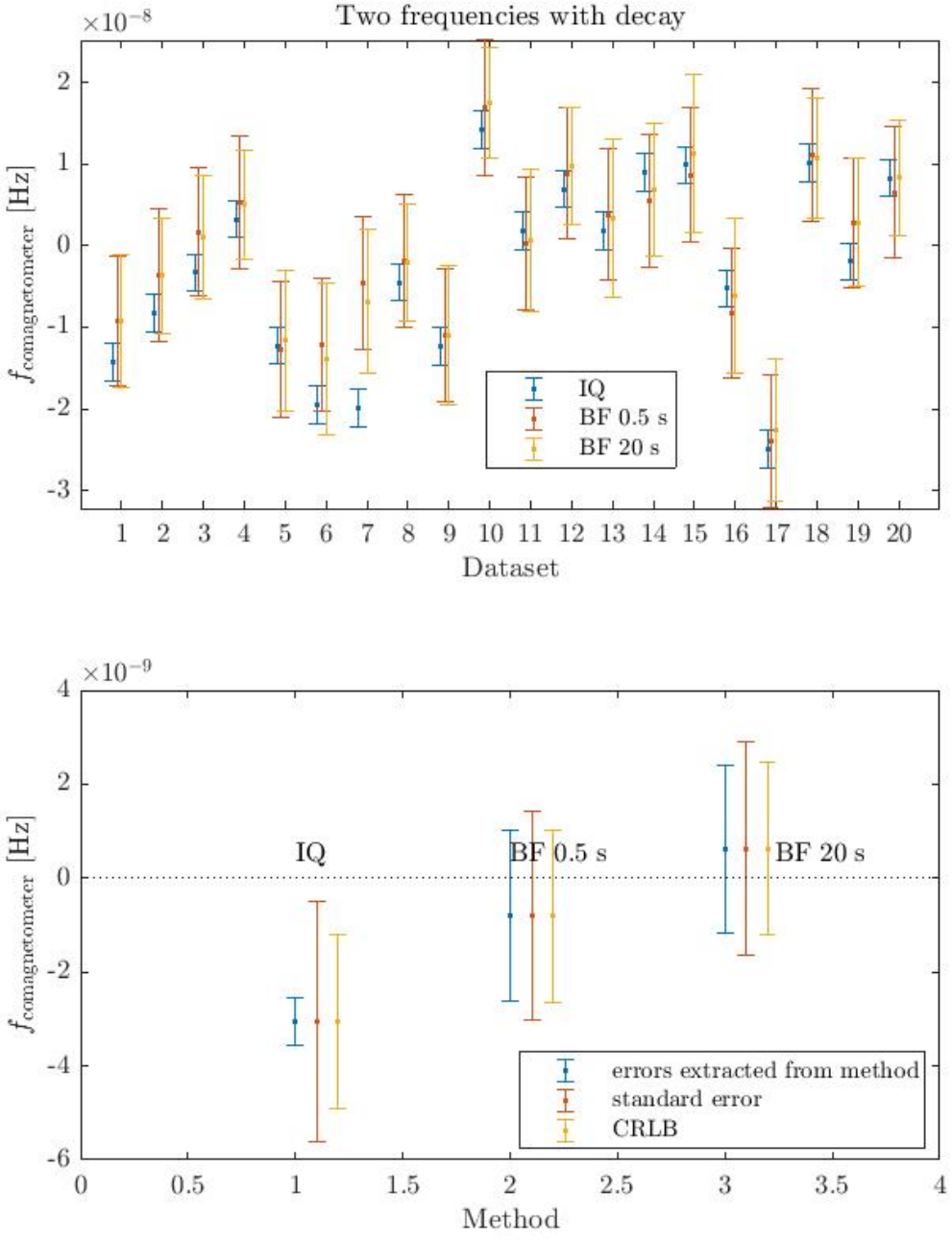

Figure A.5: The extracted frequencies from the IQ method and for varying block-lengths using the block-fitting method for two-frequency data with signal decay and added B_0 drift. The second added frequency was $f_2 = rf_1$. After extracting individual frequencies they were "comagnetometer-corrected" $f_{\text{comagnetometer}} = f_1 - rf_2$.

APPENDIX B

Monte Carlo study

We used simulated data to confirm the estimated frequency resolution for our analysis method and to perform a Monte Carlo experiment as a test of the accuracy of the analysis method used for HeXe2017.

To investigate the validity of the CRLB formula in the case of noise that is only locally white as is the case for SQUID data, this study was done using simulated data with real noise instead of additive white gaussian noise.

B.1 Simulated data generation

A set of simulated data was generated using the parameters in Table B.1. For each run, a spin precession signal was generated with the same amplitude and T_2^* decay time for each species as in the actual run. The B_0 drift was generated as a random walk process and the species-dependent drifts $\omega^{sd}_{\text{Xe/He}}(t)$ as a decaying exponential with randomized T_1 between 5000–15000 seconds.

The frequencies were generated using

$$\omega^0_{\text{He}}(t) = \gamma_{\text{He}} B_0(t) + \omega^{sd}_{\text{He}}(t) \tag{B.1}$$

and similarly for $\omega^0_{Xe}(t)$. Both frequencies were integrated to generate $\Phi^0_{\mathrm{He}}(t)$ and $\Phi^0_{\mathrm{Xe}}(t)$. The Advanpix Multiprecision Computing Toolbox for MATLAB [110] was used for greater precision for the phases. To $\Phi^0_{\mathrm{Xe}}(t)$, a false EDM phase shift corresponding to $3 \times 10^{-27}\ e\,\mathrm{cm}$ was added, using the high-voltage monitor signal from the run and the length of each cell.

Next, the spin precession signal was generated using the phases and the real run amplitudes and T_2^* times from Table B.1. The signals had the form

$$Z(t) = A^0_{\mathrm{Xe}} \cos \Phi^0_{\mathrm{Xe}}(t) e^{-t/T^*_{2,\mathrm{Xe}}} + A^0_{\mathrm{He}} \cos \Phi^0_{\mathrm{He}}(t) e^{-t/T^*_{2,\mathrm{He}}}. \tag{B.2}$$

These 16 generated signals were added to the real noise spectra of the 16 runs for each of the MC cases. Each of the MC cases used the same 16 noise spectra but a different frequency. The real noise spectra were obtained by applying a sharp band-stop filter to the ^{129}Xe and ^{3}He frequencies in the data. The MC frequencies were added sufficiently far away to avoid the filtered portion of the frequency spectrum. The MC frequencies were chosen to be in a portion of the frequency spectrum that was also flat and at least 10 mHz away from any other previously chosen MC frequency [35].

B.2 Results

The data were divided into blocks and HV segments and analyzed using the method described in Chapter V. The comagnetometer drift was corrected for using the method outlined in Chapter VI Section 6.4. The results are shown for $N = 15$ cases in Fig. B.1. The extracted EDM is consistent with the added EDM and the error bar is consistent with the standard error of the 15 cases.

Run	^{129}Xe ampl. and T_2^*	^{3}He ampl. and T_2^*	Cell	HV dwell/sep.	No. HV seg.
aC82	37.3 pT, 6926 s	5.9 pT, 6406 s	PP2	380/413 s	34
aC83	20.8 pT, 7586 s	3.2 pT, 7137 s	PP2	380/413 s	34
aC84	33.1 pT, 6931 s	4.9 pT, 6425 s	PP2	380/413 s	34
aC85	20.0 pT, 7923 s	3.2 pT, 7463 s	PP2	380/413 s	34
aC86	21.8 pT, 3725 s	4.5 pT, 5874 s	PP1	380/413 s	34
aC89	15.4 pT, 3797 s	2.8 pT, 6485 s	PP1	360/414 s	34
aC91	28.8 pT, 3998 s	5.4 pT, 6557 s	PP1	380/413 s	34
aC92	17.3 pT, 4035 s	3.8 pT, 7047 s	PP1	380/413 s	16
aC93	27.6 pT, 7210 s	4.1 pT, 6779 s	PP2	780/807 s	34
dC02	32.0 pT, 5359 s	4.4 pT, 4893 s	PP2	780/813 s	34
dC08	30.5 pT, 5362 s	4.7 pT, 4985 s	PP2	380/413 s	34
dC10	26.9 pT, 3703 s	5.3 pT, 5783 s	PP1	380/413 s	34
dC12	21.9 pT, 8577 s	4.3 pT, 8082 s	PP2	380/413 s	34
dC13	34.4 pT, 7834 s	5.1 pT, 7306 s	PP2	780/813 s	16
dC14	21.7 pT, 7689 s	3.5 pT, 7282 s	PP2	380/413 s	34
dC15	18.1 pT, 3854 s	3.8 pT, 6641 s	PP1	380/413 s	34

Table B.1: Summary of the HeXe2017 parameters used for generating simulated data. HV dwell and separation times are used in the analysis and are based on the HV monitor from the runs.

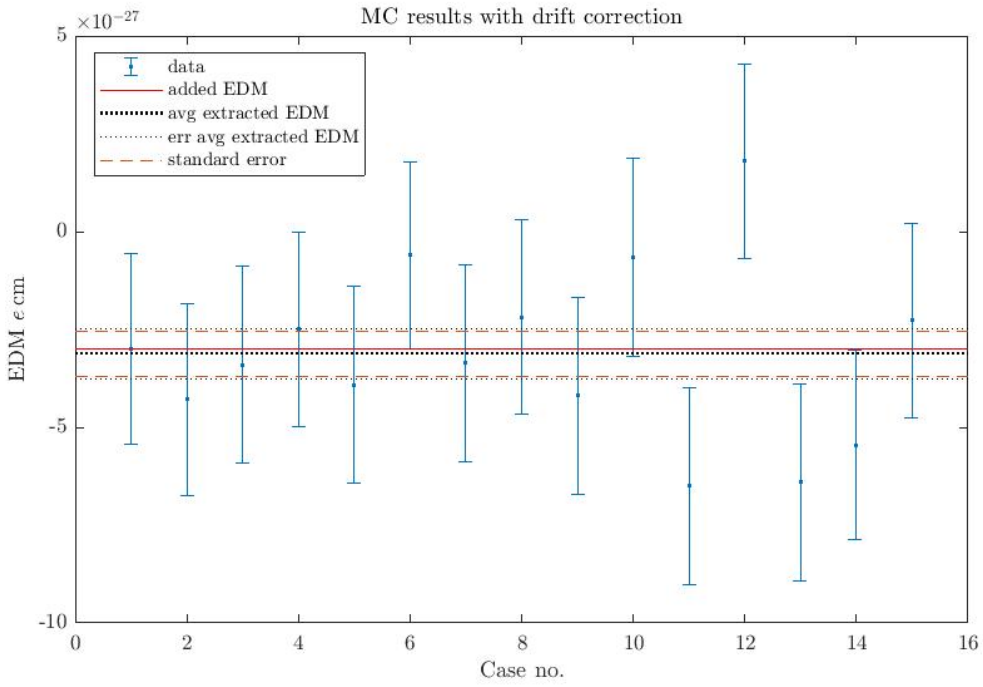

Figure B.1: Results of a Monte Carlo study of the HeXe2017 analysis method including comagnetometer drift-correction.

APPENDIX C

Choice of analysis parameters

For the HeXe2017 analysis, the analysis parameters chosen were: use of Z_1 over the gradiometer Z_{grad}, FIR high-pass filtering < 5 Hz, 6-parameter fit, 20 second block size, $[-\tau/2, \tau/2]$ block interval, 4 HV segments for each EDM sequence, and linear fit of phases to determine frequency. The following is a discussion about the use of the high-pass filter to remove baseline drift in order to use a 6-parameter fit.

The filtered data are shifted by time delay that is the same for all frequencies that needs to be corrected so that the HV timing is unaffected. The filter used and the correction are

Listing C.1: Matlab code for creating FIR filter (requires Signal Processing Toolbox)

```
1 hpFilt = designfilt('highpassfir','StopbandFrequency',0.5,'
    PassbandFrequency',5,'StopbandAttenuation',100,'
    PassbandRipple',.001,'SampleRate',f_sample);
2 D = mean(grpdelay(hpFilt));
3 zdata = filter(hpFilt,[zdata;zeros(D,1)]);
4 zdata = zdata(D+1:end)
```

where `f_sample` is the sampling frequency 915.5245 Hz.

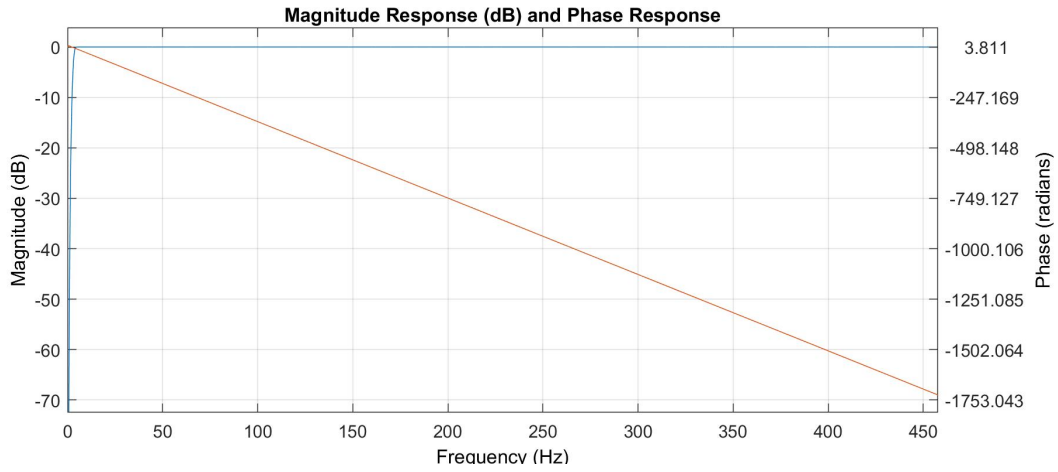

Figure C.1: Magnitude and phase response for the applied filter.

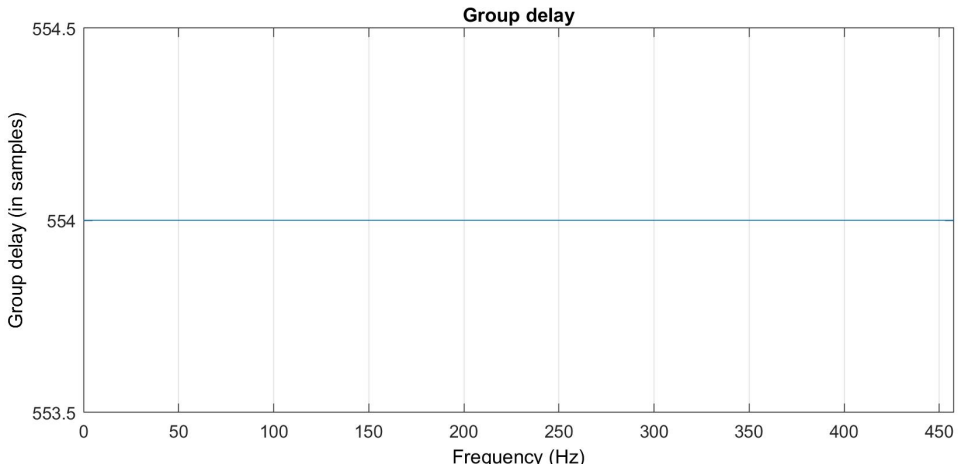

Figure C.2: $d\phi/d\omega$ for the FIR high-pass filter used for the HeXe2017 analysis.

A delay would cause the following:

$$\begin{aligned}\omega_{\mathrm{Xe}}^{\mathrm{filt}} &= \omega_{\mathrm{Xe}}^{\mathrm{unfilt}} + \frac{d}{dt}\left(\frac{d\phi_{\mathrm{Xe}}}{d\omega}\cdot\delta\omega\right) \\ &= \omega_{\mathrm{Xe}}^{\mathrm{unfilt}} + \frac{d\phi_{\mathrm{Xe}}}{d\omega}\cdot\left(\gamma_{\mathrm{Xe}}\frac{dB}{dt} + \frac{d\omega'_{\mathrm{Xe}}}{dt}\right)\end{aligned} \tag{C.1}$$

where the last term is a species-dependent frequency shift. Then the comagnetometer frequency is

$$
\begin{aligned}
\omega_{\mathrm{Xe,co}}^{\mathrm{filt}} &= \omega_{\mathrm{Xe}}^{\mathrm{filt}} - \frac{\gamma_{\mathrm{Xe}}}{\gamma_{\mathrm{He}}}\omega_{\mathrm{He}}^{\mathrm{filt}} \\
&= \omega_{\mathrm{Xe}}^{\mathrm{unfilt}} + \frac{d\phi_{\mathrm{Xe}}}{d\omega}\cdot\left(\gamma_{\mathrm{Xe}}\frac{dB}{dt} + \frac{d\omega'_{\mathrm{Xe}}}{dt}\right) - \frac{\gamma_{\mathrm{Xe}}}{\gamma_{\mathrm{He}}}\left[\omega_{\mathrm{He}}^{\mathrm{unfilt}} + \frac{d\phi_{\mathrm{He}}}{d\omega}\cdot\left(\gamma_{\mathrm{He}}\frac{dB}{dt} + \frac{d\omega'_{\mathrm{He}}}{dt}\right)\right] \\
&= \omega_{\mathrm{Xe,co}}^{\mathrm{unfilt}} + \frac{d\phi_{\mathrm{Xe}}}{d\omega}\cdot\left(\gamma_{\mathrm{Xe}}\frac{dB}{dt} + \frac{d\omega'_{\mathrm{Xe}}}{dt}\right) - \left[\frac{d\phi_{\mathrm{He}}}{d\omega}\cdot\left(\gamma_{\mathrm{Xe}}\frac{dB}{dt} + \frac{\gamma_{\mathrm{Xe}}}{\gamma_{\mathrm{He}}}\frac{d\omega'_{\mathrm{He}}}{dt}\right)\right]
\end{aligned}
$$

If $\frac{d\phi_{\mathrm{Xe}}}{d\omega} = \frac{d\phi_{\mathrm{He}}}{d\omega} = \frac{d\phi}{d\omega}$ as seen above, then

$$
\omega_{\mathrm{Xe,co}}^{\mathrm{filt}} = \omega_{\mathrm{Xe,co}}^{\mathrm{unfilt}} + \frac{d\phi}{d\omega}\cdot\left(\frac{d\omega'_{\mathrm{Xe}}}{dt} - \frac{\gamma_{\mathrm{Xe}}}{\gamma_{\mathrm{He}}}\frac{d\omega'_{\mathrm{He}}}{dt}\right)
$$

This is a correction on the order of the comagnetometer drift. If the comagnetometer drift is $\sim 1\ \mathrm{nHz/s}$ then this causes a correction of $< 0.6\ \mathrm{nHz}$ in the extracted xenon comagnetometer-corrected frequency. The error bar for each HV segment is typically 50–100 nHz. Also note that the segment lengths have been chosen such that comagnetometer drift within a HV segment is below the phase noise, so this term does not affect our extracted frequencies and errors.

Next, we compare use of a Z-gradiometer vs $Z1$ magnetometer for analysis and compare $m = 6, 7, 8$ parameter fits. The 6 parameter fit contains no SQUID offset or baseline drift terms, the 7-parameter adds the offset, and the 8-parameter fit contains both. C84 Z-gradiometer and Z_1, both filtered and unfiltered, were analyzed with a 6, 7, and 8 parameter fit. For each block fit we determined the statistic F_χ comparing the 6 and 7 or the 7 and 8-parameter fit. For the full run there were 36 segments each with 19 blocks.

We find no difference in the results using the 8-parameter fit with unfiltered data and a 6-parameter fit with filtered data.

Signal	m	filtered?	F_χ^{avg}	P^{avg}
Z_{grad}	$6 \to 7$	no	2.4×10^{6}	1
Z_{grad}	$7 \to 8$	no	1.3×10^{-2}	0.0733
Z_{grad}	$6 \to 7$	yes	2.4×10^{-5}	0.0039
Z_{grad}	$7 \to 8$	yes	1.9×10^{-5}	0.0009
Z_1	$6 \to 7$	no	1.5×10^{4}	1
Z_1	$7 \to 8$	no	2.2×10^{-3}	0.0330
Z_1	$6 \to 7$	yes	1.8×10^{-6}	0.0009
Z_1	$7 \to 8$	yes	5.6×10^{-6}	0.0015

Table C.1: F_χ averaged for all blocks and segments and corresponding probabilities.

Signal	m	filtered?	f_{EDM} (nHz)
Z_{grad}	6	no	93.92 ± 866.6
Z_{grad}	7	no	42.30 ± 16.8
Z_{grad}	8	no	42.10 ± 16.8
Z_{grad}	6	yes	42.17 ± 16.8
Z_{grad}	7	yes	42.18 ± 16.8
Z_{grad}	8	yes	42.18 ± 16.8
Z_1	6	no	72.77 ± 543.21
Z_1	7	no	28.73 ± 15.28
Z_1	8	no	28.73 ± 15.28
Z_1	6	yes	28.70 ± 15.28
Z_1	7	yes	28.69 ± 15.28
Z_1	8	yes	28.69 ± 15.28

Table C.2: Frequencies extracted from each method using a weighted average of sequences of 4. These frequencies have an additional blind to the HeXe2017 blind and should only be compared with each other.

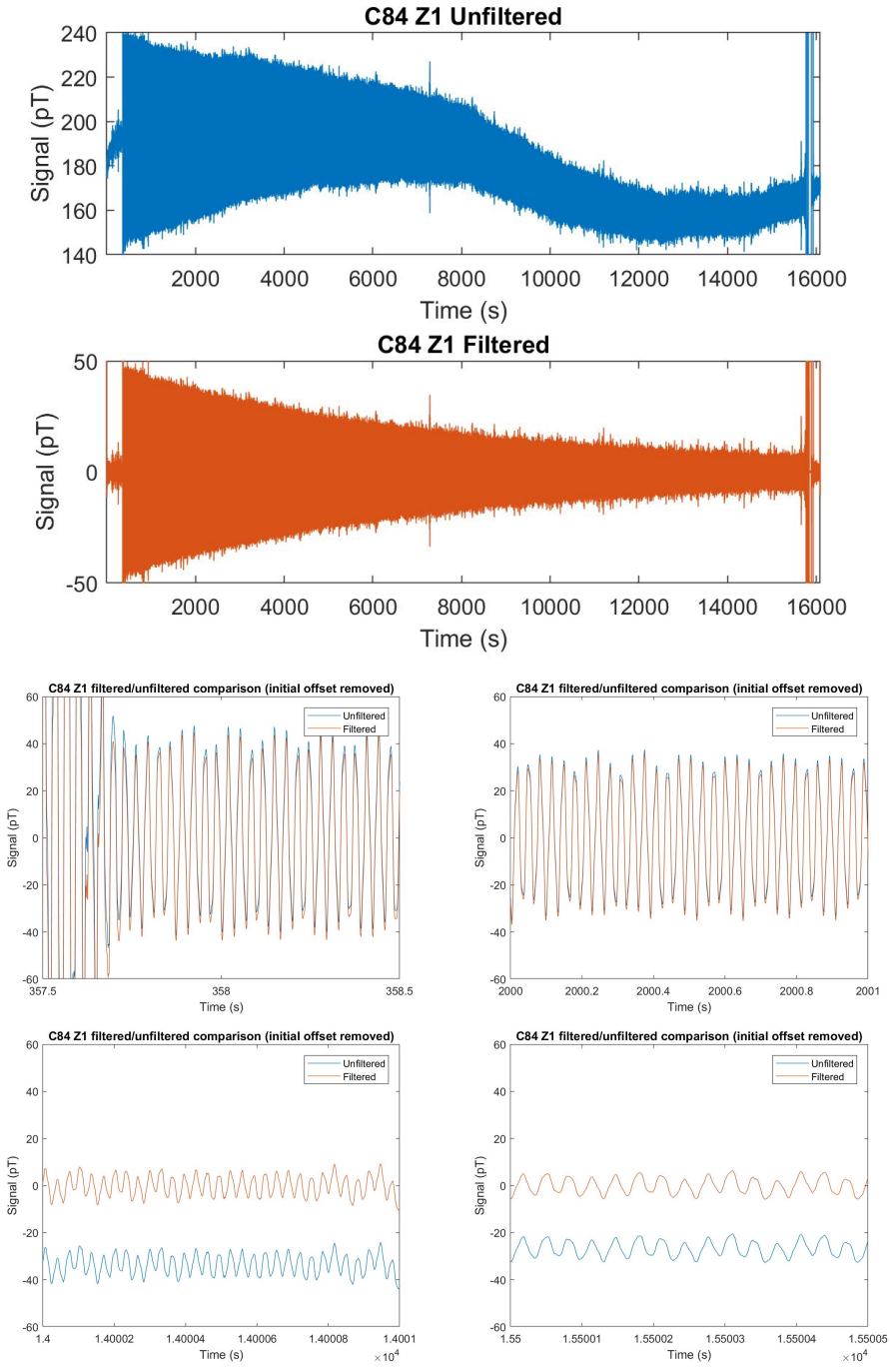

Figure C.3: Some comparisons of the filtered (delay corrected) and unfiltered signals. Top plot is the full unfiltered and filtered signal plotted separately. Bottom the two plotted on the same graph (with initial offset removed), zoomed in at various intervals.

BIBLIOGRAPHY

BIBLIOGRAPHY

[1] C. L. Bennett, M. Halpern, G. Hinshaw, N. Jarosik, A. Kogut, M. Limon, S. S. Meyer, L. Page, D. N. Spergel, G. S. Tucker, E. Wollack, E. L. Wright, C. Barnes, M. R. Greason, R. S. Hill, E. Komatsu, M. R. Nolta, N. Odegard, H. V. Peiris, L. Verde, and J. L. Weiland, "First-Year Wilkinson Microwave Anisotropy Probe (WMAP) Observations: Preliminary Maps and Basic Results," *The Astrophysical Journal Supplement Series*, vol. 148, pp. 1–27, Sept. 2003.

[2] E. W. Kolb and M. S. Turner, *The early universe.* Addison-Wesley Publishing Company, 1990.

[3] J. M. Cline, "Baryogenesis," *arXiv e-prints*, pp. hep–ph/0609145, Sept. 2006.

[4] A. Sakharov, "Violation of CP invariance, C asymmetry, and Baryon Asymmetry of the Universe," *JETP Lett.*, vol. 5, p. 24, 1967.

[5] T. E. Chupp, P. Fierlinger, M. Ramsey-Musolf, and J. Singh, "Electric dipole moments of the atoms, molecules, nuclei and particles," *ArXiv e-prints*, Oct 2017.

[6] I. B. Khriplovich and S. K. Lamoreaux, *CP Violation Without Strangeness*. Springer Berlin Heidelberg, 1997.

[7] E. M. Purcell and N. F. Ramsey, "On the possibility of electric dipole moments for elementary particles and nuclei," *Phys. Rev.*, vol. 78, pp. 807–807, Jun 1950.

[8] J. Smith, *A Search for a Permanent Electric Dipole Moment of the Neutron*. PhD thesis, Harvard University, 1951.

[9] J. H. Smith, E. M. Purcell, and N. F. Ramsey, "Experimental limit to the electric dipole moment of the neutron," *Phys. Rev.*, vol. 108, pp. 120–122, Oct 1957.

[10] T. D. Lee and C. N. Yang, "Question of parity conservation in weak interactions," *Phys. Rev.*, vol. 104, pp. 254–258, Oct 1956.

[11] C. S. Wu, E. Ambler, R. W. Hayward, D. D. Hoppes, and R. P. Hudson, "Experimental test of parity conservation in beta decay," *Phys. Rev.*, vol. 105, pp. 1413–1415, Feb 1957.

[12] R. L. Garwin, L. M. Lederman, and M. Weinrich, "Observations of the failure of conservation of parity and charge conjugation in meson decays: the magnetic moment of the free muon," *Phys. Rev.*, vol. 105, pp. 1415–1417, Feb 1957.

[13] J. I. Friedman and V. L. Telegdi, "Nuclear emulsion evidence for parity nonconservation in the decay chain $\pi^+ - \mu^+ - e^+$," *Phys. Rev.*, vol. 105, pp. 1681–1682, Mar 1957.

[14] J. H. Christenson, J. W. Cronin, V. L. Fitch, and R. Turlay, "Evidence for the 2π decay of the k_2^0 meson," *Phys. Rev. Lett.*, vol. 13, pp. 138–140, Jul 1964.

[15] L. I. Schiff, "Measurability of nuclear electric dipole moments," *Phys. Rev.*, vol. 132, pp. 2194–2200, Dec 1963.

[16] P. Sandars, "The electric dipole moment of an atom," *Physics Letters*, vol. 14, no. 3, pp. 194 – 196, 1965.

[17] P. Sandars, "Enhancement factor for the electric dipole moment of the valence electron in an alkali atom," *Physics Letters*, vol. 22, no. 3, pp. 290 – 291, 1966.

[18] J. Engel, M. J. Ramsey-Musolf, and U. van Kolck, "Electric dipole moments of nucleons, nuclei, and atoms: The standard model and beyond," *Progress in Particle and Nuclear Physics*, vol. 71, pp. 21 – 74, 2013. Fundamental Symmetries in the Era of the LHC.

[19] T. E. Chupp and M. Ramsey-Musolf, "Electric dipole moments: A global analysis," *Phys. Rev. C*, vol. 91, p. 035502, Mar 2015.

[20] N. Yamanaka, B. K. Sahoo, N. Yoshinaga, T. Sato, K. Asahi, and B. P. Das, "Probing exotic phenomena at the interface of nuclear and particle physics with the electric dipole moments of diamagnetic atoms: A unique window to hadronic and semileptonic CP violation," *The European Physical Journal A*, vol. 53, p. 54, Mar 2017.

[21] J. M. Pendlebury, S. Afach, N. J. Ayres, C. A. Baker, G. Ban, G. Bison, K. Bodek, M. Burghoff, P. Geltenbort, K. Green, W. C. Griffith, M. van der Grinten, Z. D. Grujić, P. G. Harris, V. Hélaine, P. Iaydjiev, S. N. Ivanov, M. Kasprzak, Y. Kermaidic, K. Kirch, H.-C. Koch, S. Komposch, A. Kozela, J. Krempel, B. Lauss, T. Lefort, Y. Lemière, D. J. R. May, M. Musgrave, O. Naviliat-Cuncic, F. M. Piegsa, G. Pignol, P. N. Prashanth, G. Quéméner, M. Rawlik, D. Rebreyend, J. D. Richardson, D. Ries, S. Roccia, D. Rozpedzik, A. Schnabel, P. Schmidt-Wellenburg, N. Severijns, D. Shiers, J. A. Thorne, A. Weis, O. J. Winston, E. Wursten, J. Zejma, and G. Zsigmond, "Revised experimental upper limit on the electric dipole moment of the neutron," *Phys. Rev. D*, vol. 92, p. 092003, Nov 2015.

[22] M. A. Rosenberry and T. E. Chupp, "Atomic electric dipole moment measurement using spin exchange pumped masers of $^{129}\mathrm{Xe}$ and $^{3}\mathrm{He}$," *Phys. Rev. Lett.*, vol. 86, pp. 22–25, Jan 2001.

[23] B. Graner, Y. Chen, E. G. Lindahl, and B. R. Heckel, "Reduced limit on the permanent electric dipole moment of $^{199}\mathrm{Hg}$," *Phys. Rev. Lett.*, vol. 116, p. 161601, Apr 2016.

[24] M. Bishof, R. H. Parker, K. G. Bailey, J. P. Greene, R. J. Holt, M. R. Kalita, W. Korsch, N. D. Lemke, Z.-T. Lu, P. Mueller, T. P. O'Connor, J. T. Singh, and M. R. Dietrich, "Improved limit on the $^{225}\mathrm{Ra}$ electric dipole moment," *Phys. Rev. C*, vol. 94, p. 025501, Aug 2016.

[25] T. G. Vold, F. J. Raab, B. Heckel, and E. N. Fortson, "Search for a permanent electric dipole moment on the $^{129}\mathrm{Xe}$ atom," *Phys. Rev. Lett.*, vol. 52, pp. 2229–2232, Jun 1984.

[26] E. R. Oteiza, *Search for a Permanent Electric Dipole Moment in XENON-129 Using Simultaneous HELIUM-3 Magnetometry*. PhD thesis, HARVARD UNIVERSITY., 1992.

[27] T. E. Chupp, E. R. Oteiza, and R. J. Hoare, "The search for a permanent electric dipole moment using 129xe and 3he," *AIP Conference Proceedings*, vol. 270, no. 1, pp. 84–95, 1991.

[28] T. Inoue, T. Furukawa, A. Yoshimi, T. Nanao, M. Chikamori, K. Suzuki, H. Hayashi, H. Miyatake, Y. Ichikawa, M. Tsuchiya, N. Hatakeyama, S. Kagami, M. Uchida, H. Ueno, Y. Matsuo, T. Fukuyama, and K. Asahi, "Frequency characteristics of nuclear spin oscillator with an artificial feedback toward search for^{129}Xe atomic electric dipole moment," *Eur. Phys. J.*, vol. D70, no. 6, p. 129, 2016.

[29] M. P. Ledbetter, S. Pustelny, D. Budker, M. V. Romalis, J. W. Blanchard, and A. Pines, "Liquid-state nuclear spin comagnetometers," *Phys. Rev. Lett.*, vol. 108, p. 243001, Jun 2012.

[30] F. Allmendinger, U. Schmidt, W. Heil, S. Karpuk, A. Scharth, Y. Sobolev, K. Tullney, and S. Zimmer, "Probing Physics beyond the Standard Model with He/Xe clock comparison experiments," in *Proceedings, 6th Meeting on CPT and Lorentz Symmetry (CPT 13): Bloomington, Indiana, USA, June 17-21, 2013*, pp. 17–20, 2014.

[31] Y. Masuda, K. Asahi, K. Hatanaka, S.-C. Jeong, S. Kawasaki, R. Matsumiya, K. Matsuta, M. Mihara, and Y. Watanabe, "Neutron electric dipole moment measurement with a buffer gas comagnetometer," *Physics Letters A*, vol. 376, no. 16, pp. 1347 – 1351, 2012.

[32] T. E. Chupp, E. R. Oteiza, J. M. Richardson, and T. R. White, "Precision frequency measurements with polarized $^{3}\mathrm{He}$, $^{21}\mathrm{Ne}$, and $^{129}\mathrm{Xe}$ atoms," *Phys. Rev. A*, vol. 38, pp. 3998–4003, Oct 1988.

[33] C. Gemmel, W. Heil, S. Karpuk, K. Lenz, Y. Sobolev, K. Tullney, M. Burghoff, W. Kilian, S. Knappe-Grüneberg, W. Müller, A. Schnabel, F. Seifert, L. Trahms, and U. Schmidt, "Limit on lorentz and CPT violation of the bound neutron using a free precession $^{3}\mathrm{He}/^{129}\mathrm{Xe}$ comagnetometer," *Phys. Rev. D*, vol. 82, p. 111901, Dec 2010.

[34] F. Allmendinger, W. Heil, S. Karpuk, W. Kilian, A. Scharth, U. Schmidt, A. Schnabel, Y. Sobolev, and K. Tullney, "New limit on Lorentz invariance and CPT-violating neutron spin interactions using a free-spin-precession ^{3}He-^{129}Xe comagnetometer," *Phys. Rev. Lett.*, vol. 112, p. 110801, Mar 2014.

[35] Y. Chibane, S. K. Lamoreaux, J. M. Pendlebury, and K. F. Smith, "Minimum variance of frequency estimations for a sinusoidal signal with low noise," *Measurement Science and Technology*, vol. 6, pp. 1671–1678, dec 1995.

[36] T. E. Chupp, R. J. Hoare, R. L. Walsworth, and B. Wu, "Spin-exchange-pumped ^{3}He and ^{129}Xe Zeeman masers," *Phys. Rev. Lett.*, vol. 72, pp. 2363–2366, Apr 1994.

[37] E. Krägeloh, "Spin clock measurements using hyper-polarized helium and xenon," Master's thesis, Technische Universität München, 2016.

[38] A. Abragam, *Principles of Nuclear Magnetism (International Series of Monographs on Physics)*. Clarendon Press, 1983.

[39] C. P. Slichter, *Principles of Magnetic Resonance (Springer Series in Solid-State Sciences) (v. 1)*. Springer, 1996.

[40] R. L. Gamblin and T. R. Carver, "Polarization and relaxation processes in He^3 gas," *Phys. Rev.*, vol. 138, pp. A946–A960, May 1965.

[41] L. D. Schearer and G. K. Walters, "Nuclear spin-lattice relaxation in the presence of magnetic-field gradients," *Phys. Rev.*, vol. 139, pp. A1398–A1402, Aug 1965.

[42] G. D. Cates, S. R. Schaefer, and W. Happer, "Relaxation of spins due to field inhomogeneities in gaseous samples at low magnetic fields and low pressures," *Phys. Rev. A*, vol. 37, pp. 2877–2885, Apr 1988.

[43] Barbé, R., Leduc, M., and Laloë, F., "Résonance magnétique en champ de radiofréquence inhomogène - 2 e partie: Vérifications expérimentales; mesure du coefficient de self-diffusion de 3He," *J. Phys. France*, vol. 35, no. 12, pp. 935–951, 1974.

[44] R. H. Acosta, L. Agulles-Pedrós, S. Komin, D. Sebastiani, H. W. Spiess, and P. Blümler, "Diffusion in binary gas mixtures studied by NMR of hyperpolarized gases and molecular dynamics simulations," *Phys. Chem. Chem. Phys.*, vol. 8, pp. 4182–4188, 2006.

[45] W. Hogervorst, "Diffusion coefficients of noble-gas mixtures between 300 K and 1400 K," *Physica*, vol. 51, pp. 59–76, Jan. 1971.

[46] T. R. Marrero and E. A. Mason, "Gaseous diffusion coefficients," *Journal of Physical and Chemical Reference Data*, vol. 1, no. 1, pp. 3–118, 1972.

[47] A. P. Malinauskas, "Gaseous diffusion. the systems He–Ar, Ar–Xe, and He–Xe," *The Journal of Chemical Physics*, vol. 42, no. 1, pp. 156–159, 1965.

[48] K. P. Srivastava, "Mutual diffusion of binary mixtures of helium, argon and xenon at different temperatures," *Physica*, vol. 25, pp. 571–578, 1959.

[49] R. Trengove and P. J. Dunlop, "Diffusion coefficients and thermal diffusion factors for five binary systems of nitrogen and a noble gas," *Physica A: Statistical Mechanics and its Applications*, vol. 115, no. 3, pp. 339 – 352, 1982.

[50] K. C. Hasson, G. D. Cates, K. Lerman, P. Bogorad, and W. Happer, "Spin relaxation due to magnetic-field inhomogeneities: Quartic dependence and diffusion-constant measurements," *Phys. Rev. A*, vol. 41, pp. 3672–3688, Apr 1990.

[51] N. Bloembergen, E. M. Purcell, and R. V. Pound, "Nuclear magnetic relaxation," *Nature*, vol. 160, pp. 475–476, Oct 1947.

[52] H. C. Torrey, "Bloch equations with diffusion terms," *Phys. Rev.*, vol. 104, pp. 563–565, Nov 1956.

[53] M. G. Richards, B. P. Cowan, M. F. Secca, and K. Machin, "The 3 He nuclear Zeeman maser," *Journal of Physics B: Atomic, Molecular and Optical Physics*, vol. 21, no. 4, p. 665, 1988.

[54] D. D. McGregor, "Transverse relaxation of spin-polarized $^3\mathrm{He}$ gas due to a magnetic field gradient," *Phys. Rev. A*, vol. 41, pp. 2631–2635, Mar 1990.

[55] W. Happer, "Optical pumping," *Rev. Mod. Phys.*, vol. 44, pp. 169–249, Apr 1972.

[56] S. Appelt, A. B.-A. Baranga, C. J. Erickson, M. V. Romalis, A. R. Young, and W. Happer, "Theory of spin-exchange optical pumping of $^3\mathrm{He}$ and $^{129}\mathrm{Xe}$," *Phys. Rev. A*, vol. 58, pp. 1412–1439, Aug 1998.

[57] V. Lefevre-Seguin and M. Leduc, "Metastability-exchange and depolarising collisions in xenon and krypton," *Journal of Physics B: Atomic and Molecular Physics*, vol. 10, no. 11, p. 2157, 1977.

[58] T. G. Walker and W. Happer, "Spin-exchange optical pumping of noble-gas nuclei," *Rev. Mod. Phys.*, vol. 69, pp. 629–642, Apr 1997.

[59] N. D. Bhaskar, J. Camparo, W. Happer, and A. Sharma, "Light narrowing of magnetic resonance lines in dense, optically pumped alkali-metal vapor," *Phys. Rev. A*, vol. 23, pp. 3048–3064, Jun 1981.

[60] T. E. Chupp and K. P. Coulter, "Polarization of $^{21}\mathrm{Ne}$ by spin exchange with optically pumped Rb vapor," *Phys. Rev. Lett.*, vol. 55, pp. 1074–1077, Sep 1985.

[61] T. E. Chupp, M. E. Wagshul, K. P. Coulter, A. B. McDonald, and W. Happer, "Polarized, high-density, gaseous $^3\mathrm{He}$ targets," *Phys. Rev. C*, vol. 36, pp. 2244–2251, Dec 1987.

[62] M. E. Wagshul and T. E. Chupp, "Optical pumping of high-density Rb with a broadband dye laser and GaAlAs diode laser arrays: Application to $^3\mathrm{He}$ polarization," *Phys. Rev. A*, vol. 40, pp. 4447–4454, Oct 1989.

[63] E. S. Hrycyshyn and L. Krause, "Inelastic collisions between excited alkali atoms and molecules. VII. Sensitized fluorescence and quenching in mixtures of rubidium with H2, HD, D2, N2, CH4, CD4, C2H4, and C2.H6," *Canadian Journal of Physics*, vol. 48, no. 22, pp. 2761–2768, 1970.

[64] C. B. Alcock, V. P. Itkin, and M. K. Horrigan, "Vapour pressure equations for the metallic elements: 298–2500K," *Canadian Metallurgical Quarterly*, vol. 23, no. 3, pp. 309–313, 1984.

[65] R. J. Knize, "Spin destruction in rubidium-rubidium and potassium-potassium collisions," *Phys. Rev. A*, vol. 40, pp. 6219–6222, Dec 1989.

[66] M. E. Wagshul and T. E. Chupp, "Laser optical pumping of high-density Rb in polarized $^3\mathrm{He}$ targets," *Phys. Rev. A*, vol. 49, pp. 3854–3869, May 1994.

[67] J. Singh, *Alkali-Hybrid Spin-Exchange Optically-Pumped Polarized ^{3}He Targets Used for Studying Neutron Structure*. PhD thesis, University of Virginia, 2010.

[68] I. A. Nelson, *Physics of practical spin-exchange optical pumping*. PhD thesis, University of Wisconsin–Madison, 2001.

[69] Y.-Y. Jau, N. N. Kuzma, and W. Happer, "High-field measurement of the $^{129}\mathrm{Xe}-\mathrm{Rb}$ spin-exchange rate due to binary collisions," *Phys. Rev. A*, vol. 66, p. 052710, Nov 2002.

[70] I. C. Ruset, *Hyperpolarized ^{129}Xe Production and Applications*. PhD thesis, University of New Hampshire, 2005.

[71] T. G. Walker, "Fundamentals of spin-exchange optical pumping," *Journal of Physics: Conference Series*, vol. 294, no. 1, p. 012001, 2011.

[72] E. Babcock, *Spin-exchange optical pumping with alkali-metal vapors*. PhD thesis, University of Wisconsin-Madison, 2005.

[73] E. Babcock, B. Chann, T. G. Walker, W. C. Chen, and T. R. Gentile, "Limits to the polarization for spin-exchange optical pumping of $^3\mathrm{He}$," *Phys. Rev. Lett.*, vol. 96, p. 083003, Mar 2006.

[74] B. Chann, E. Babcock, L. W. Anderson, and T. G. Walker, "Skew light propagation in optically thick optical pumping cells," *Phys. Rev. A*, vol. 66, p. 033406, Sep 2002.

[75] B. Lancor, E. Babcock, R. Wyllie, and T. G. Walker, "Circular dichroism of RbHe and RbN_2 molecules," *Phys. Rev. A*, vol. 82, p. 043435, Oct 2010.

[76] I. Altarev, E. Babcock, D. Beck, M. Burghoff, S. Chesnevskaya, T. Chupp, S. Degenkolb, I. Fan, P. Fierlinger, A. Frei, E. Gutsmiedl, S. Knappe-Grüneberg, F. Kuchler, T. Lauer, P. Link, T. Lins, M. Marino, J. McAndrew, B. Niessen, S. Paul, G. Petzoldt, U. Schläpfer, A. Schnabel, S. Sharma, J. Singh, R. Stoepler, S. Stuiber, M. Sturm, B. Taubenheim, L. Trahms, J. Voigt, and T. Zechlau, "A magnetically shielded room with ultra low residual field and gradient," *Review of Scientific Instruments*, vol. 85, no. 7, p. 075106, 2014.

[77] I. Altarev, M. Bales, D. H. Beck, T. Chupp, K. Fierlinger, P. Fierlinger, F. Kuchler, T. Lins, M. G. Marino, B. Niessen, G. Petzoldt, U. Schläpfer, A. Schnabel, J. T. Singh, R. Stoepler, S. Stuiber, M. Sturm, B. Taubenheim, and J. Voigt, "A large-scale magnetic shield with 106 damping at millihertz frequencies," *Journal of Applied Physics*, vol. 117, no. 18, p. 183903, 2015.

[78] J. Bork, H.-D. Hahlbohm, R. Klein, and A. Schnabel, "The 8-layered magnetically shielded room of the PTB: design and construction," *Proceedings 13th International Conference on Biomagnetism (Biomag2002)*, p. 970, 2002.

[79] F. Thiel, A. Schnabel, S. Knappe-Grüneberg, D. Stollfuß, and M. Burghoff, "Demagnetization of magnetically shielded rooms," *Review of Scientific Instruments*, vol. 78, no. 3, p. 035106, 2007.

[80] D. Budker and D. F. J. Kimball, eds., *Optical Magnetometry*. Cambridge University Press, 2009.

[81] D. Drung, "High-T_c and low-T_c dc SQUID electronics," *Superconductor Science Technology*, vol. 16, pp. 1320–1336, Dec 2003.

[82] J. Clarke and A. I. Braginski, eds., *The SQUID Handbook*. Wiley-VCH Verlag GmbH & Co. KGaA, May 2004.

[83] D. Drung and H. Koch, "An integrated dc squid magnetometer with variable additional positive feedback," *Superconductor Science and Technology*, vol. 7, no. 5, p. 242, 1994.

[84] J.-H. Storm, P. Hömmen, D. Drung, and R. Körber, "An ultra-sensitive and wideband magnetometer based on a superconducting quantum interference device," *Applied Physics Letters*, vol. 110, no. 7, p. 072603, 2017.

[85] M. Burghoff, H. Schleyerbach, D. Drung, L. Trahms, and H. Koch, "A vector magnetometer module for biomagnetic application," *IEEE Transactions on Appiled Superconductivity*, vol. 9, pp. 4069–4072, Jun 1999.

[86] J. Voigt, *Entwicklung eines Messsystems zur Charakterisierung magnetisch geschirmter Umgebungen*. PhD thesis, Technischen Universit"at Ilmenau,, 2015.

[87] S. Degenkolb, *Optical Magnetometry Using Multiphoton Transitions*. PhD thesis, University of Michigan, 2016.

[88] N. Kazakov, ed., *Diffusion Bonding of Materials*. Elsevier, 1985.

[89] F. Kuchler, *Electric dipole moment searches using the isotope 129-xenon*. PhD thesis, Technische Universität München, 2014.

[90] J. N. Zerger, M. J. Lim, K. P. Coulter, and T. E. Chupp, "Polarization of 129xe with high power external-cavity laser diode arrays," *Applied Physics Letters*, vol. 76, no. 14, pp. 1798–1800, 2000.

[91] E. Babcock, B. Chann, I. A. Nelson, and T. G. Walker, "Frequency-narrowed diode array bar," *Appl. Opt.*, vol. 44, pp. 3098–3104, May 2005.

[92] E. S. Korchak, W. Kilian, and L. Mitschang, "Configuration and performance of a mobile ^{129}Xe polarizer," *Appl. Magn. Reson.*, vol. 44, pp. 65–80, 2013.

[93] J. Meinel, "Investigations of the simultaneous spin precession of He-3 and Xe-129 at microtesla magnetic fields," bachelor's thesis, Technische Universität München, 2014.

[94] "Multi-channel analog data acquisition system." Available at `https://www.ptb.de/cms/fileadmin/internet/fachabteilungen/abteilung_8/8.2_biosignale/8.21/laye.pdf`.

[95] W. A. Terrano, J. Meinel, N. Sachdeva, T. Chupp, S. Degenkolb, P. Fierlinger, F. Kuchler, and J. T. Singh, "Frequency shifts in noble-gas magnetometers," *arXiv e-prints*, p. arXiv:1807.11119, July 2018.

[96] J. Meinel, "Investigations of systematic frequency shifts in ^{3}He/^{129}Xe comagnetometers for ^{129}Xe electric dipole measurement," Master's thesis, Technische Universität München, 2017.

[97] M. V. Romalis, D. Sheng, B. Saam, and T. G. Walker, "Comment on "new limit on lorentz-invariance- and cpt-violating neutron spin interactions using a free-spin-precession $^3\mathrm{He}-^{129}\mathrm{Xe}$ comagnetometer"," *Phys. Rev. Lett.*, vol. 113, p. 188901, Oct 2014.

[98] F. Allmendinger, U. Schmidt, W. Heil, S. Karpuk, A. Scharth, Y. Sobolev, and K. Tullney, "Allmendinger et al. reply:," *Phys. Rev. Lett.*, vol. 113, p. 188902, Oct 2014.

[99] F. Bloch and A. Siegert, "Magnetic resonance for nonrotating fields," *Phys. Rev.*, vol. 57, pp. 522–527, Mar 1940.

[100] N. F. Ramsey, "Resonance transitions induced by perturbations at two or more different frequencies," *Phys. Rev.*, vol. 100, pp. 1191–1194, Nov 1955.

[101] J. H. Wesenberg and K. Mølmer, "Field inside a random distribution of parallel dipoles," *Phys. Rev. Lett.*, vol. 93, p. 143903, Sep 2004.

[102] S. G. Rautian, "On the strength distribution of a field created by randomly distributed dipoles," *Optics and Spectroscopy*, vol. 100, pp. 739–747, May 2006.

[103] P. Bevington and D. Robinson, *Data Reduction and Error Analysis for the Physical Sciences*. McGraw-Hill, 1992.

[104] G. Golub and V. Pereyra, "Separable nonlinear least squares: the variable projection method and its applications," *Inverse Problems*, vol. 19, no. 2, p. R1, 2003.

[105] I. Fan, S. Knappe-Grüneberg, J. Voigt, W. Kilian, M. Burghoff, D. Stollfuss, A. Schnabel, G. Wübbeler, O. Bodner, C. Elster, F. Seifert, and L. Trahms, "Direct measurement of the γ_{he} / γ_{xe} ratio at ultralow magnetic field," *Journal of Physics: Conference Series*, vol. 723, no. 1, p. 012045, 2016.

[106] W. J. Riley, "Handbook of frequency stability analysis," *NIST Special Publication 1065*, 2008.

[107] D. Sheng, A. Kabcenell, and M. V. Romalis, "New classes of systematic effects in gas spin comagnetometers," *Phys. Rev. Lett.*, vol. 113, p. 163002, Oct 2014.

[108] S. K. Lamoreaux and R. Golub, "Detailed discussion of a linear electric field frequency shift induced in confined gases by a magnetic field gradient: Implications for neutron electric-dipole-moment experiments," *Phys. Rev. A*, vol. 71, p. 032104, Mar 2005.

[109] M. E. Limes, N. Dural, M. V. Romalis, E. L. Foley, T. W. Kornack, A. Nelson, and L. R. Grisham, "Dipolar and scalar ^{3}He and ^{129}Xe frequency shifts in mm-sized cells," *arXiv e-prints*, p. arXiv:1805.11578, May 2018.

[110] "Advanpix Multiprecision Computing Toolbox." `https://www.advanpix.com`.